

Naval Research Laboratory

Washington, DC 20375-5320



AD-A267 075



NRL/MR/6721--93-7312

X-Ray Laser Program Final Report for FY92

Complied by

JOHN P. APRUZESE

*Radiation Hydrodynamics Branch
Plasma Physics Division*

July 1, 1993

DTIC
ELECTE
JUL 22 1993
S E D

This work was supported by the Strategic Defense Initiative Organization under
Job Title, Ultra Short Wavelength Laser Research

03 7

Approved for public release; distribution unlimited.

93-16397



REPORT DOCUMENTATION PAGE			Form Approved OMB No. 0704-0188	
Public reporting burden for this collection of information is estimated to average 1 hour per response, including the time for reviewing instructions, searching existing data sources, gathering and maintaining the data needed, and completing and reviewing the collection of information. Send comments regarding this burden estimate or any other aspect of this collection of information, including suggestions for reducing this burden, to Washington Headquarters Services, Directorate for Information Operations and Reports, 1215 Jefferson Davis Highway, Suite 1204, Arlington, VA 22202-4302, and to the Office of Management and Budget, Paperwork Reduction Project (0704-0188), Washington, DC 20503.				
1. AGENCY USE ONLY (Leave Blank)	2. REPORT DATE July 1, 1993	3. REPORT TYPE AND DATES COVERED Final 10/1/91 - 09/30/92		
4. TITLE AND SUBTITLE X-Ray Laser Program Final Report for FY92			5. FUNDING NUMBERS PE - 63220C	
6. AUTHOR(S) Compiled by John P. Apruzese: authors identified in subsections				
7. PERFORMING ORGANIZATION NAME(S) AND ADDRESS(ES) Naval Research Laboratory Washington, DC 20375-5320			8. PERFORMING ORGANIZATION REPORT NUMBER NRL/MR/6721-93-7312	
9. SPONSORING/MONITORING AGENCY NAME(S) AND ADDRESS(ES) Strategic Defense Initiative Organization T/IS Pentagon Washington, DC 20301-7100			10. SPONSORING/MONITORING AGENCY REPORT NUMBER	
11. SUPPLEMENTARY NOTES This work was supported by the Strategic Defense Initiative Organization under Job Title, Ultra Short Wavelength Laser Research.				
12a. DISTRIBUTION/AVAILABILITY STATEMENT Approved for public release; distribution unlimited.			12b. DISTRIBUTION CODE	
13. ABSTRACT (Maximum 200 words) This report details the progress achieved by the Radiation Hydrodynamics Branch in X-Ray Laser experiments and modeling during FY92. Some of the experimental work discussed was carried out at Sandia National Laboratories in collaboration with NRL. It is divided into an executive summary and sections whose authors are separately identified. The individual sections describe progress in photopumped x-ray laser research, calculations of x-ray inversions, intensities, and pulsewidths in plasmas created by ultraintense subpicosecond lasers, and effects of non-Maxwellian electron distributions on x-ray gain.				
14. SUBJECT TERMS X-ray laser Neonlike lasers X-ray pulsewidth Resonant photoexcitation Population inversion Ultra short pulse lasers Spectroscopy Pulsed power Transient transport phenomena			15. NUMBER OF PAGES 87	
			16. PRICE CODE	
17. SECURITY CLASSIFICATION OF REPORT UNCLASSIFIED	18. SECURITY CLASSIFICATION OF THIS PAGE UNCLASSIFIED	19. SECURITY CLASSIFICATION OF ABSTRACT UNCLASSIFIED	20. LIMITATION OF ABSTRACT SAR	

CONTENTS

EXECUTIVE PROGRAM SUMMARY	iv
I. Enhancement of Ionization in Neon X-ray Laser Targets Radiatively Driven by a Sodium Potassium Z Pinch	1
II. Ultra Short Pulse Laser Produced Aluminum Plasma	21
III. Escape Time of Heliumlike Alpha Resonance Line Photons Emitted from Optically Thick Plasmas	29
IV. The Influence of Non-Maxellian Distributions on the Gain of 3s-3p Transitions in Neonlike Selenium	54

Accession For	
NTIS CRA&I	<input checked="checked" type="checkbox"/>
DTIC TAB	<input type="checkbox"/>
Unannounced	<input type="checkbox"/>
Justification	
By	
Distribution /	
Availability Codes	
Dist	Avail and / or Special
A-1	

U.S. GOVERNMENT PRINTING OFFICE: 1970 O 340-000

EXECUTIVE PROGRAM SUMMARY

This report describes the x-ray laser research conducted by the Radiation Hydrodynamics Branch under SDIO sponsorship during FY 1992. Some of the experimental work was performed at Sandia National Laboratories as part of a collaboration with NRL. This document consists of four sections whose authors are separately identified, each detailing progress in a different aspect of the overall effort.

Last year's report described the first, and still the only, achievement of a population inversion in the x-ray region of the spectrum by resonant photopumping. The experiment consisted of two basic components: an intensely radiating pure sodium Z pinch whose He α transition is resonant at 11 \AA with the 1-4 He γ line of neon, and a neon gas cell which is photoionized by the approximately 10 TW of total x-rays coming from the pinch. Since that noteworthy accomplishment, further work has concentrated on enhancing the photoionization of the neon and detecting and measuring the possible laser lines.

To photoionize neon to the He-like stage, it is critical that the pumping pinch produce sufficient photons in the energy regions near the photoionization edges of the Li, Be, and B-like stages (about 250 - 450 eV for Ne). The first section describes work in which the soft power output spectrum of the pure sodium pinch was measured as a function of energy. These initial measurements showed that the photon flux in the critical 250 - 450 eV region was considerably less than that which would obtain if the pinch radiated a Planckian spectrum with a temperature appropriate to the total measured power output. As a means of increasing this critical photon power, potassium was introduced into the (previously) pure sodium pinch, since it is a more efficient soft x-ray radiator. The results are easily summarized: it works. Replacing 25% of the sodium with potassium has no appreciable effect on the power of the optically thick pump line, but raises the subkilovolt power of the pinch a remarkable factor of 3. Furthermore, the comparative spectra of neon clearly demonstrate enhanced ionization when the sodium-potassium load is employed.

The figure at the end of this summary shows three of the spectra in the region of the possible neon laser lines which were obtained at Sandia with the new sodium-potassium load. The two lines near 217 \AA may represent the first detection of a He-like 4-3 line but

this identification is still uncertain at this time. Note also the unexplained increase of a factor of 5 of the 5f-3d Li-like line when the fill pressure is increased by only 50%. The 5f-3d line in Li-like Al has been observed to lase in recombination by no less than 8 groups worldwide. This very interesting observation in our photopumped system is now under further experimental and theoretical investigation for the potential of a recombination laser.

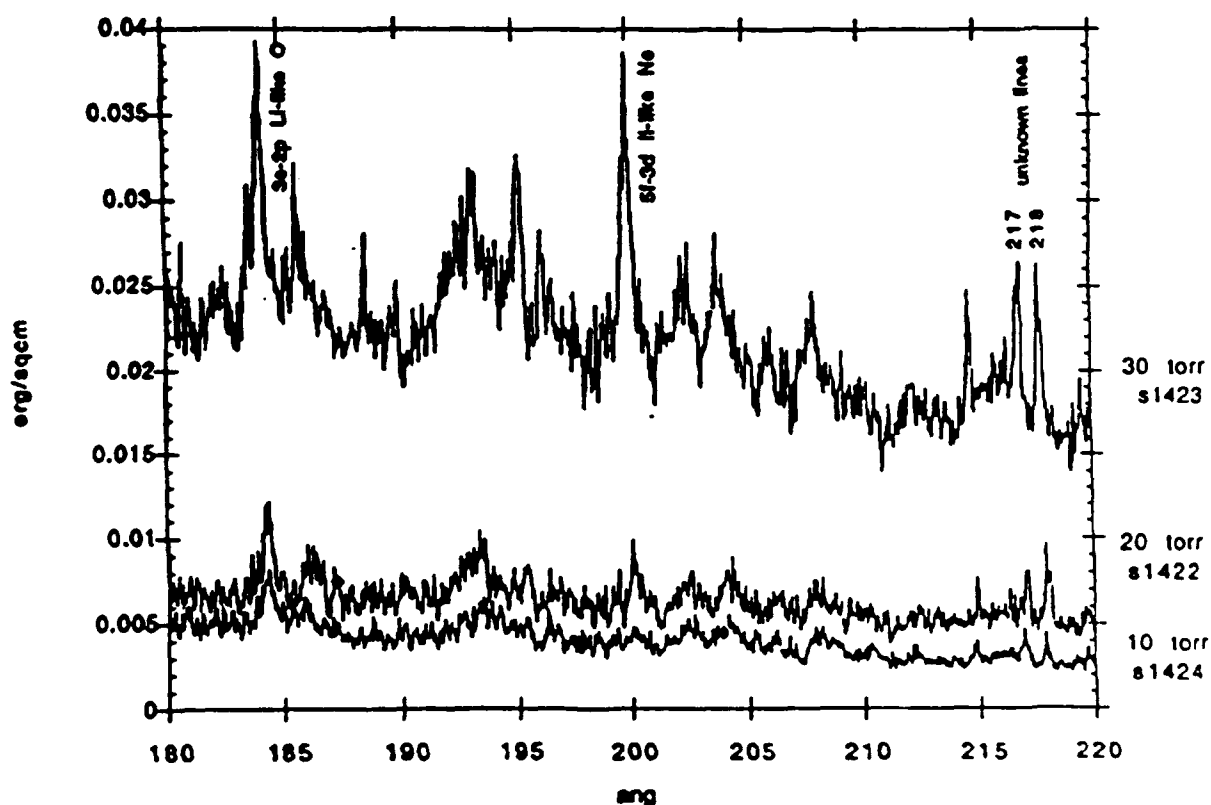
Another important advance in photopumped x-ray laser research was accomplished at the Laboratory of Plasma Studies, Cornell University, in work which had been supported in part on a previous SDIO contract and had involved some collaboration with NRL. At Cornell, resonant photopumping has been demonstrated via fluorescence observations in the Al - Mg system, on a pulsed-power device producing only 400 kiloamperes peak current. This work has been accepted for publication by Physical Review A and is scheduled for the March, 1993 issue. The authors are Qi, Hammer, Kalantar, and Mittal.

Resonant photopumping has now been demonstrated on 3 different pulsed-power machines, ranging in peak current from 0.4 MA (LION, Cornell), to 1 MA (Gamble II, NRL), to 10 MA (Saturn, Sandia National Laboratories). The Sandia experiment also produced population inversion.

Ultra-intense, femtosecond-pulsed laboratory lasers ranging from the ultraviolet to the infrared represent an exciting new tool for investigations varying from basic atomic and plasma physics to specific mission-oriented goals. We have continued our assessment of the potentialities of these devices with respect to their production of gain at ultrashort wavelengths and also for excitation of superintense incoherent x-ray sources. Section 2 considers the interaction of a subpicosecond laser pulse with a planar aluminum target, using a model which includes solution of the Helmholtz wave equation as well as self-consistent detailed configuration atomic physics coupled to radiation hydrodynamics. Among other results, the temperature and density profiles midway from the leading edge of the blowoff plasma are found to support population inversions for a number of upper states. A remaining question is whether these inversions persist for timescales of interest for extracting gain. In many laser-produced plasmas, the most intense radiation emanates

from the strongest resonance lines which by nature of their large oscillator strengths are most likely to be optically thick. Escape of this radiation is a diffusion-like process which can affect the x-ray pulsewidth and thus the intensity. In section 3, the basic time-dependent transfer model which was described in last year's report is applied to the He-like α line which is often the most intense K shell radiator. Wide-ranging results for the pulsewidth as well as analytic models including atomic number scaling enable accurate assessments to be made of this effect in virtually any accessible laboratory experiment.

Various laser absorption mechanisms can result in the production of non-Maxwellian electron distributions which in turn affect the atomic state populations by altering the relevant rates. This problem is considered in detail in Section 4 for neonlike lasers (the most robust of the short wavelength systems). It is found that generation of ion-acoustic turbulence at high laser intensities can in principle increase the gain of 3s-3p transitions and improve the performance of these lasers.



The Li-like neon 5f-3d potential laser line at 200 Å increases dramatically with fill pressure of the neon gas cell.

Enhancement of Ionization in Neon X-ray Laser Targets Radiatively Driven by a Sodium-Potassium Z Pinch

T. Nash, R. Spielman, and T. Tanaka
Sandia National Laboratories

J. Apruzese and R. W. Clark
Naval Research Laboratory

Abstract

We present spatially and temporally resolved XUV spectra from a neon gas cell laser target that is photopumped by a high power sodium z pinch 2 cm away radiating 10 TW. In this sodium/neon photoresonant laser scheme the 2 to 1 transition of He-like Na in the pinch nominally radiates 200 GW and is resonant with the 4 to 1 transition in He-like neon. We have measured the ionization balance of the neon gas cell as a function of both space and time and found that with a pure sodium pinch the neon L shell is not completely ionized. By introducing 25% potassium into the z pinch load we have increased the amount of He-like neon in the target without appreciably affecting the sodium pump power. The spatial profile of neon ionization states is consistent with a radiatively driven shock propagating through and heating the neon gas cell target.

Manuscript approved March 12, 1993.

I. Introduction

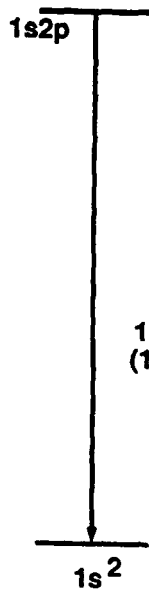
X-ray lasers demonstrated to date have been pumped by collisional excitation and recombination. 1-10 Although resonant photopumping could potentially produce an efficient x-ray laser 11-20, the shortest wavelength at which photopumped gain has been measured is 2163 Å in Be-like C. 21

Using elliptical crystal spectroscopy, resonant photopumping of the $n=4$ level of He-like neon by a sodium z pinch on the pulsed power driver Saturn has been demonstrated. 22 The 200 GW pump is sufficient to produce a measureable 4 to 3 inversion in He-like neon. Details are presented in Reference 22. The next logical step in this x-ray laser research is to measure the strongest predicted laser transition, the 4f-3d singlet line at 231 Å.

The atomic energy level diagram including the coincident lines for the sodium/neon x-ray laser scheme is shown in figure 1. The resonant photopump of typically 200 GW in the He-like sodium 2 to 1 transition is provided by the z pinch load of the Saturn accelerator. Saturn also emits up to 10 TW total radiation which photoionizes the neon L shell in the neon laser target, and is predicted to drive a shock wave from the side window of the gas cell into the neon. 23 The 4p singlet level of He-like neon is resonantly photopumped. Electron and ion collisions distribute the population and hence the 4 to 3 inversion over the $n=4$ sublevels and the largest gain is predicted for the 4f to 3d singlet transition at 231 Å. 13,19

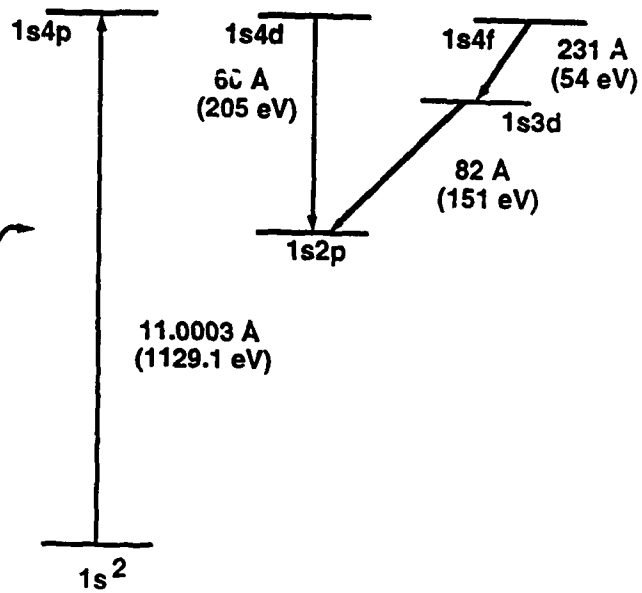
The experimental arrangement is shown in figure 2. Saturn delivers approximately 10 MA with a 60 nsec rise time to a sodium z pinch load. The pinch radiates up to 10 TW with 200 GW in the resonant photopump. The pulsewidth of the resonant photopump is 20 to 30 nsec. A neon gas cell is placed with its side window 18 mm from the pinch axis, just outside of the pinch current return posts. This

He-like Na (pump)

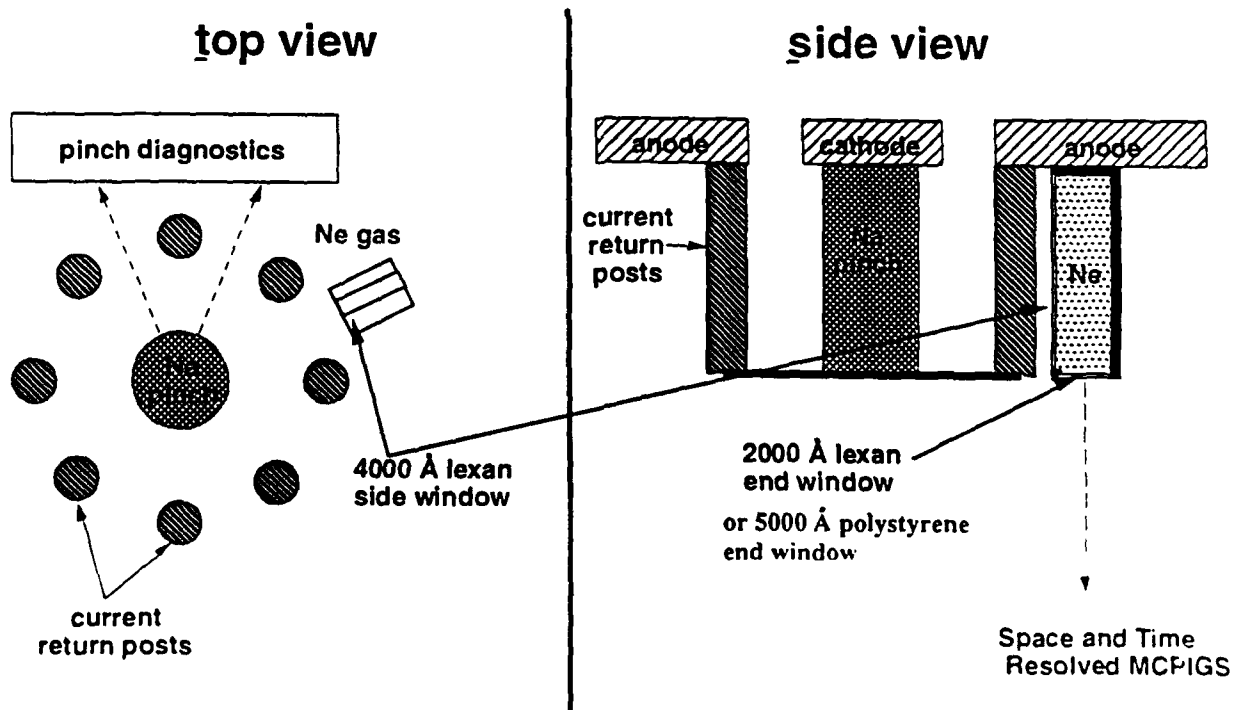


11.0027 Å
(1129.2 eV)

He-like Ne (lasing)



1. Atomic energy level diagram for Sodium/Neon photoresonant x-ray laser scheme.



2. Experimental Layout of Z-pinch, target, and diagnostic.

assures that the neon is heated by radiation rather than current. A neon fill pressure of 10 torr is confined by a 4000 Å Lexan side window and an end window that is either 2000 Å Lexan or 5000 Å polystyrene. The pumping radiation is incident on and ionizes the side window, and also heats the neon gas target. XUV radiation is measured along an axial line of sight passing through the end window with a spatially resolved 10 nsec gated MCPIGS (microchannel plate (MCP) intensified one meter grazing incidence spectrometer).²⁴

II. Instrumentation

We measure the XUV spectra from the neon gas cell with a spatially resolved single time gated MCPIGS. The MCP is curved to the one meter diameter of the Rowland circle. The instrumental acceptance is f/40 up to a 3 meter radius 2 degree grazing incidence spherical gathering mirror.

A 6 mm wide by 150 mm long stripline on the MCP is gated by a 10 nsec 900 volt pulse to provide a single 10 nsec resolved time frame. Typically the gate is centered on the peak of the z pinch x-ray emission. On the short 6 mm width of the strip we spatially resolve with an imaging cylindrical mirror at 5 degrees grazing incidence. With spatial magnification of 1/2.7 the spatial resolution at the target is better than 1 mm. However due to the large 150 mm length of the spectral focus, the spatial focus degrades rapidly away from the spatial focus wavelength. At spectral locations 15 Å from the spatial focus, the spatial resolution degrades to worse than 1 mm. This limitation in the spatial imaging of the MCPIGS will be addressed in the future by using a flat field variable line spaced grating spectrometer that maintains spatial focus along the entire spectral range. On the MCPIGS instrument we use two vacuum spacers, one for spatial focus at 230 Å and one for spatial focus at 80 Å, assuming the use of a typical 1200 l/mm grating.

For the spatial focus at 230 Å we use a 1200 l/mm grating blazed at 5 degrees, and a 1000 Å Al filter to remove higher orders. For spatial focus at 80 Å we use no filter and a 1200 l/mm grating blazed at 2 degrees. The entrance slit width is typically 20 microns and the grating is half masked.

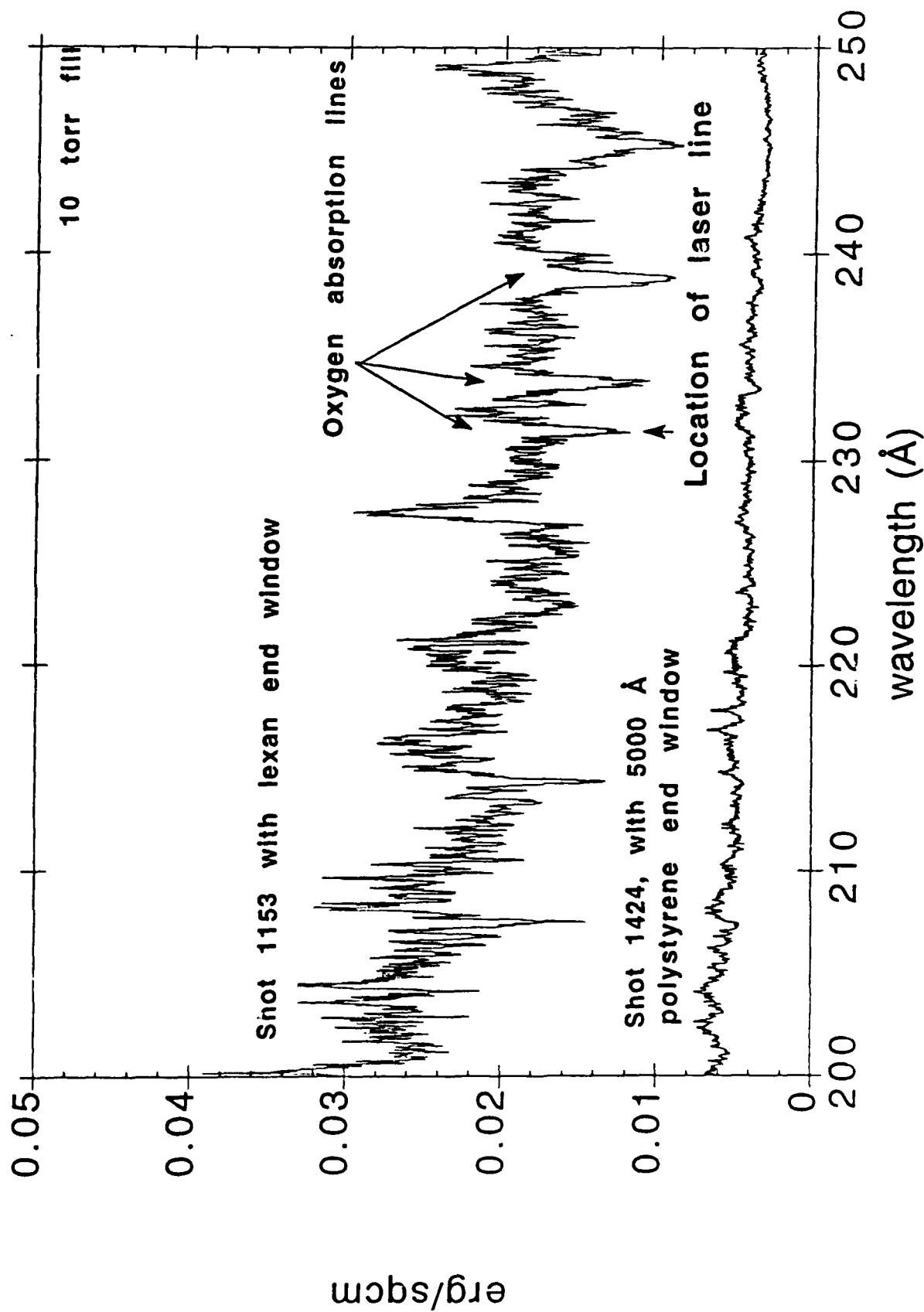
A spherical spectral gathering mirror sets the field of view as 1 mm wide at the gas cell, the other dimension of the gas cell being imaged by the cylindrical mirror. A close to close fast valve with 3 mm by 3 cm aperture open for 500 microseconds protects the mirrors from shot debris.

The microchannel plate is backed by a fiber optic faceplate coated with P11 phosphor. The spectral data is recorded on Kodak type 2484 film, then digitized and computer processed.

III. Results

Our initial and unsuccessful attempt at measuring the 231 Å line is depicted in figure 3. When viewed through a 2000 Å thick lexan end window the spectrum is plagued with oxygen absorption lines, one of which falls precisely on the location of the laser line. We then eliminated these oxygen lines by using a 5000 Å oxygen-free polystyrene end window. With this end window the oxygen absorption lines disappear and the background level, likely due to oxygen lines as well as continuum emission, is reduced. Estimates of instrumental sensitivity and fluorescent yield in the laser line indicate that we are unlikely to detect the 231 Å transition unless it is lasing with a gain greater than 1 cm^{-1} .

Measurements of ionization balance are made by recording spectra in the 70 to 120 Å window. This region includes bright 3 to 2 transitions in Be-like, Li-like, and He-like neon. With a pure sodium

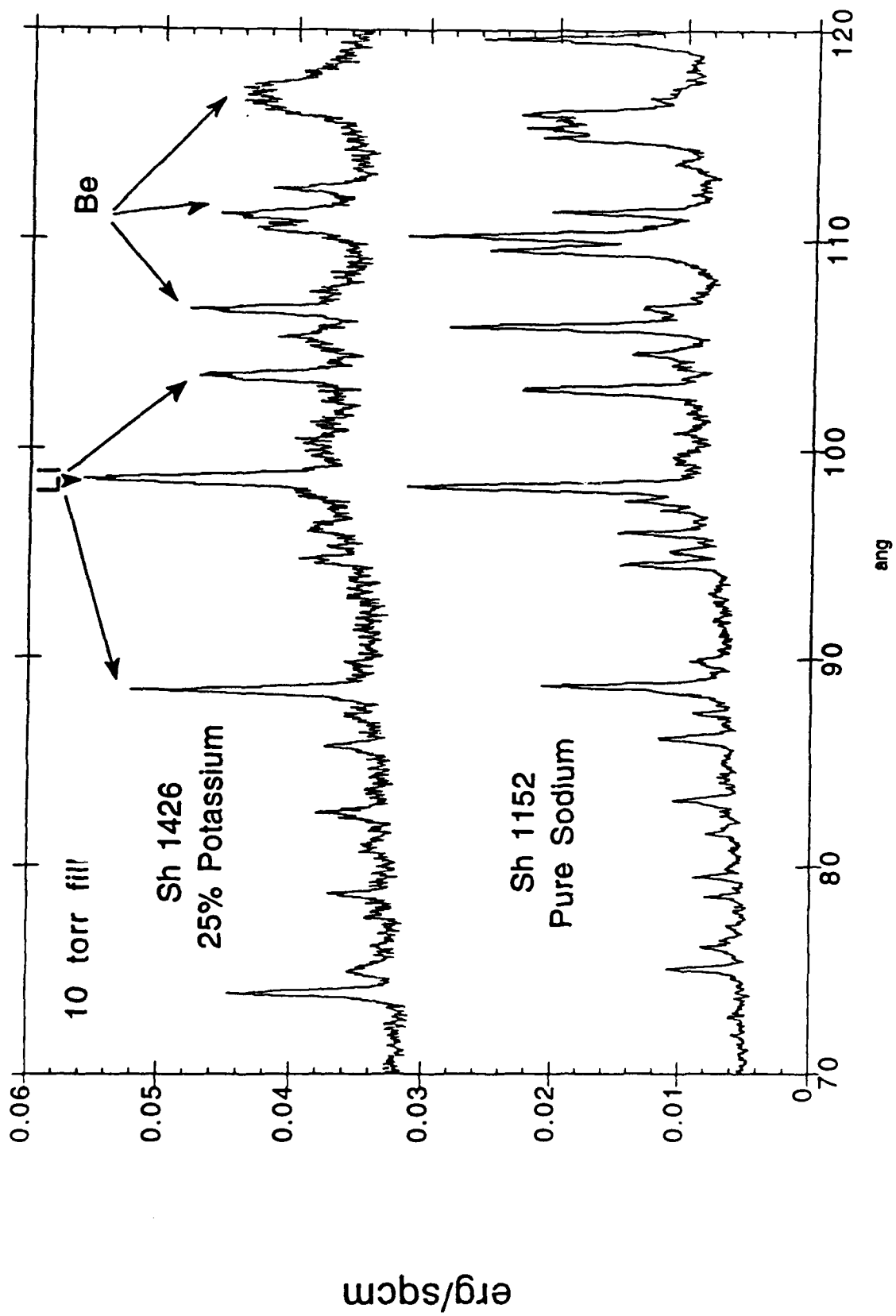


3. A polystyrene end window eliminates oxygen absorption.

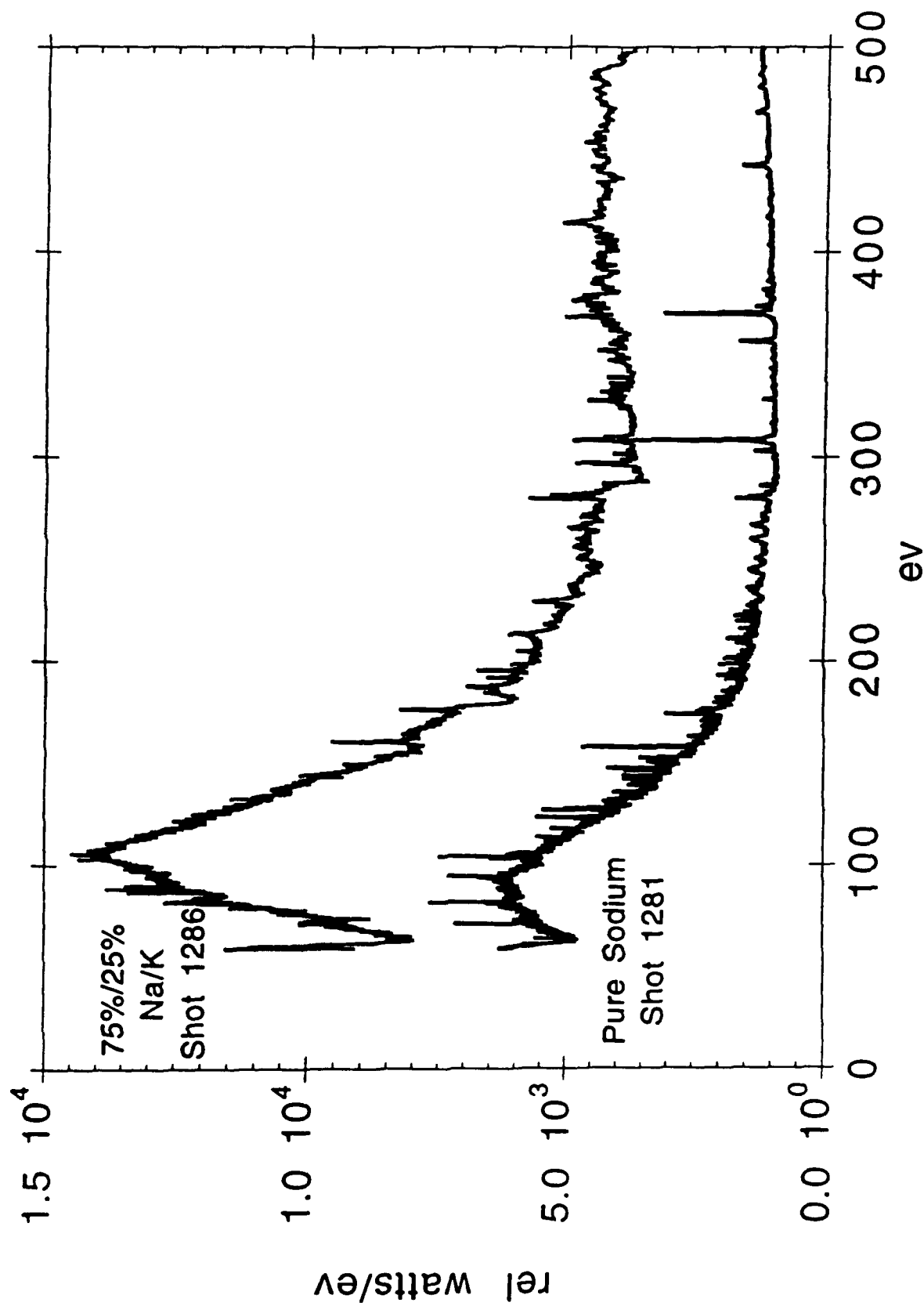
z pinch pump the lines of Be-like and Li-like neon are about equal as depicted in the bottom trace of figure 4. One reason we are not detecting the L_α line could be a paucity of He-like neon. Complete photoionization of the neon L shell requires copious radiation at 240 to 450 eV energies, and a sodium plasma is lacking in transitions near these energies. In order to increase the photoionization pump we introduce potassium into the z pinch with the idea that potassium L radiation could help photoionize the neon L shell and produce more He-like neon. With 25% potassium in the driving pinch the ratio of Li-like to Be-like neon line intensities increases a factor of 2 indicating a higher ionization level and thus more He-like neon is present when potassium is used in the pinch.

The spectra of both pure sodium and sodium-potassium pinches were measured with a grazing incidence spectrometer. This data is shown in figure 5. The spectral distributions are based on an estimate of instrumental response. The signal at all subkilovolt energies increases a factor of 3 when 25% of the pinch mass is potassium. This increases the ability of the pumping z pinch to photoionize the neon L shell, as corroborated by the data of figure 4.

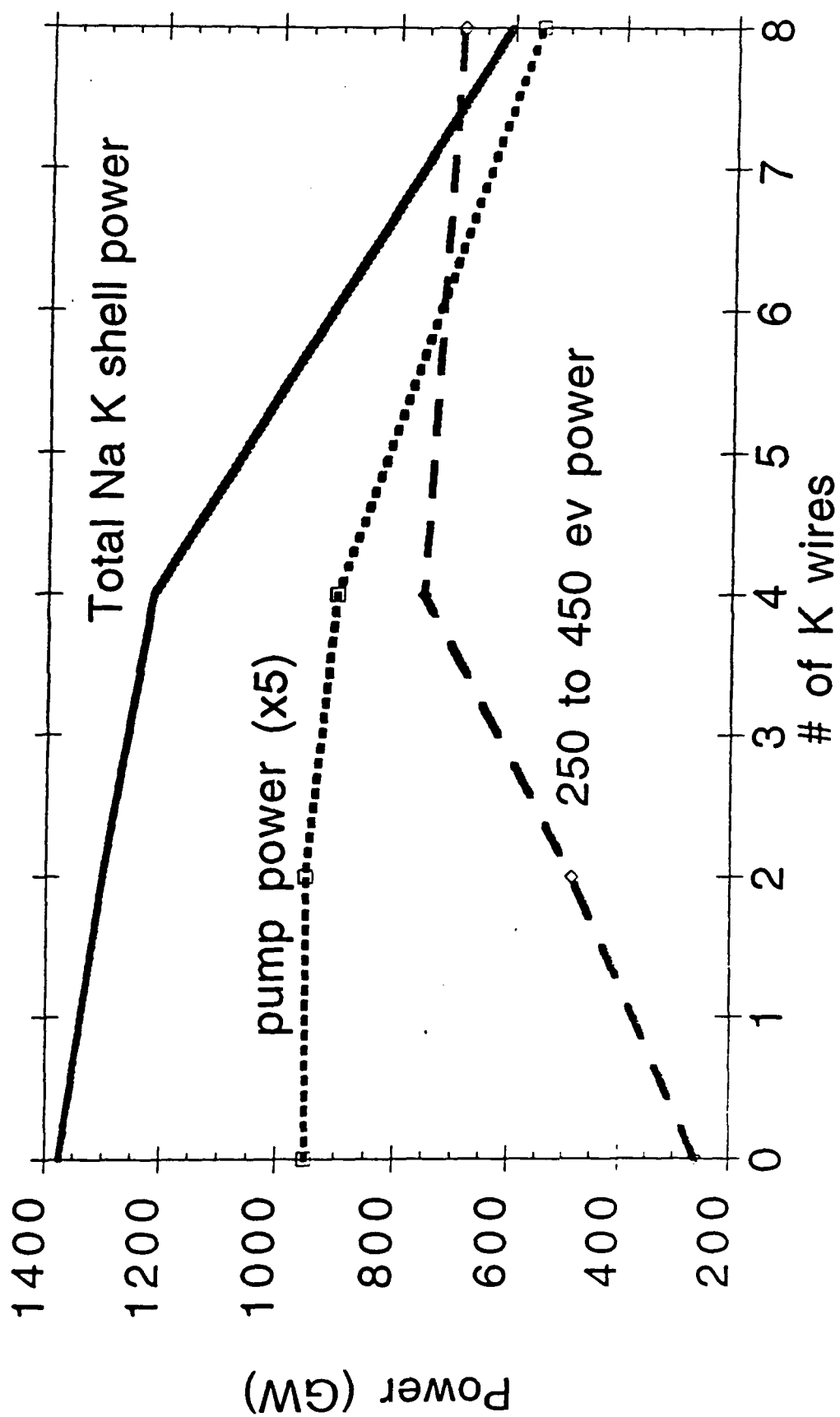
The effect of different amounts of potassium introduced into the sodium pinch was scanned on a shot to shot basis. The results are shown in figure 6. The total number of wires in the z pinch load array is 16. The power in the 250 to 450 eV window is measured by a titanium-filtered carbon x-ray diode. This diode shows the power in this window increasing a factor of 3 in going from 0 to 25% potassium in the load, and is in agreement with the spectroscopic data of figure 5. The 11 Å resonant photopump line power and total sodium K shell power, measured by x-ray diodes, bolometers, and photoconductive detectors, do not significantly decrease up to a 25% fraction (4 wires) of potassium. However at 50% potassium (8 wires) the sodium K shell and resonant photopump power fall off dramatically. The data of figure 6 shows that 25% potassium in the sodium load optimizes the ability of the z pinch to both photoionize the neon L shell and resonantly photopump the He-like neon.



4. Potassium increases the ionization state of the neon target.



5. A small amount of potassium impurity greatly increases the soft x-ray yield.



6. Four potassium wires maximizes the 250-450 eV power without appreciably affecting the pump power.

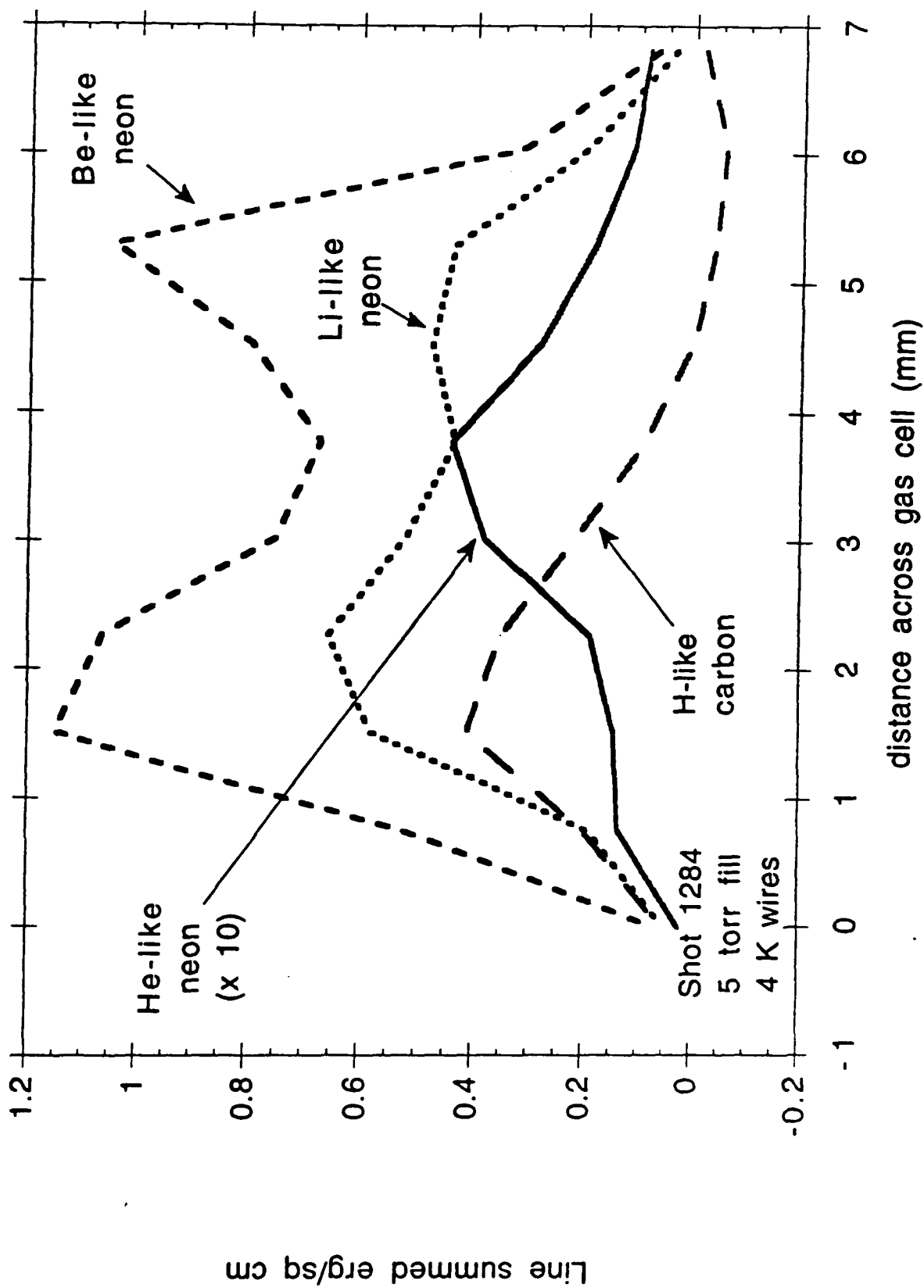
IV. Spatial Ionization Profiles and Interpretation

The spatial distributions of lines of He-like, Li-like, and Be-like neon, and H-like carbon, recorded with a 10 nsec gate centered on the radiation power pulse are shown in figure 7. The lines are the 78.3 Å 3d-2p triplet transition for He-like neon, the 98.2 Å 3d-2p transition for Li-like neon, the cluster of 3d-2p triplet transitions around 110 Å for Be-like neon, and Balmer alpha at 182 Å for H-like carbon. Be-like and Li-like neon are seen to burn out at the center of the gas cell where He-like emissions peak. The neon is likely heated by a radiatively driven shock wave that moves from the side window across the gas cell. The H-like carbon in figure 7 comes from the side window and its location of intensity fall-off indicates the position of the shock. The shock is estimated to travel 1 mm during the 10 nsec data acquisition gate. The shock evidently heats a localized region of the neon, burning through the L shell and enhancing He-like neon in concert with direct photoionization.

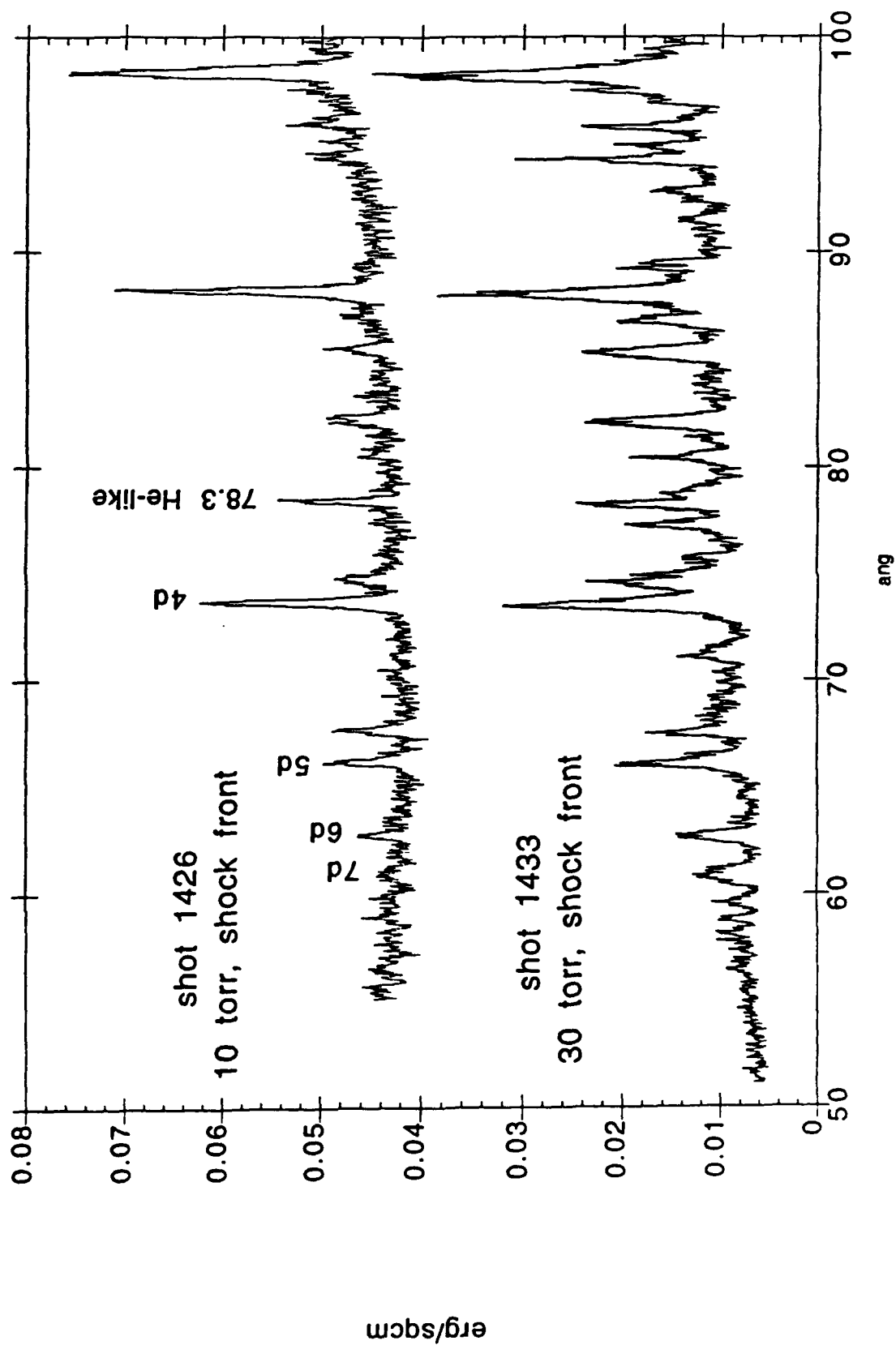
As mentioned above, the He-like neon line measured is the 78.3 Å 3d to 2p triplet transition array. This is the only strong XUV line from He-like neon we have detected. Modelling indicates that this line should be stronger than other He-like neon XUV lines because the lower 2p triplet level of this transition has a slow decay time and a large population. We have also detected the 3p-2s triplet transition at 74.4 Å in He-like neon at a level barely above background noise.

The small measured intensity of the 3d-2p He-like line points out the difficulty of measuring the candidate laser transition which is predicted to be about 10 times weaker in fluorescence.

The optimum fill pressure for detecting He-like neon lines in the XUV has been found to be 10 torr. In figure 8 the upper trace shows the 78.3 Å He-like neon line at almost 1/2 the intensity of the Li-like 4d



7. At the shock front the He-like line peaks where the Li-like and Be-like lines burn out.



8. The He-like line is strong at the shock front, but increasing pressure causes recombination.

to 2p line, measured at the shock front with a 10 torr fill pressure. At 30 torr fill pressure the 78.3 Å line intensity increases only slightly and is overwhelmed by surrounding lines from Li-like and Be-like neon. Modeling indicates that the higher fill pressure causes recombinations back into lower ionization states, whereas the ionization continues to be dominated by the fixed photon source.

The evolution of the neon gas cell target has been calculated for a variety of assumed pump pinch spectra using the one-dimensional planar radiation-hydrodynamics model described in Reference 25. In these calculations, the assumed initial neon fill pressure has also been varied. The neon atomic model includes 52 spectral lines in Ne VIII through X and 29 continuum bound-free edges, all self-consistently coupled to the energy equation via multifrequency radiation transport. Some of the initial results of these calculations have been described in Reference 23.

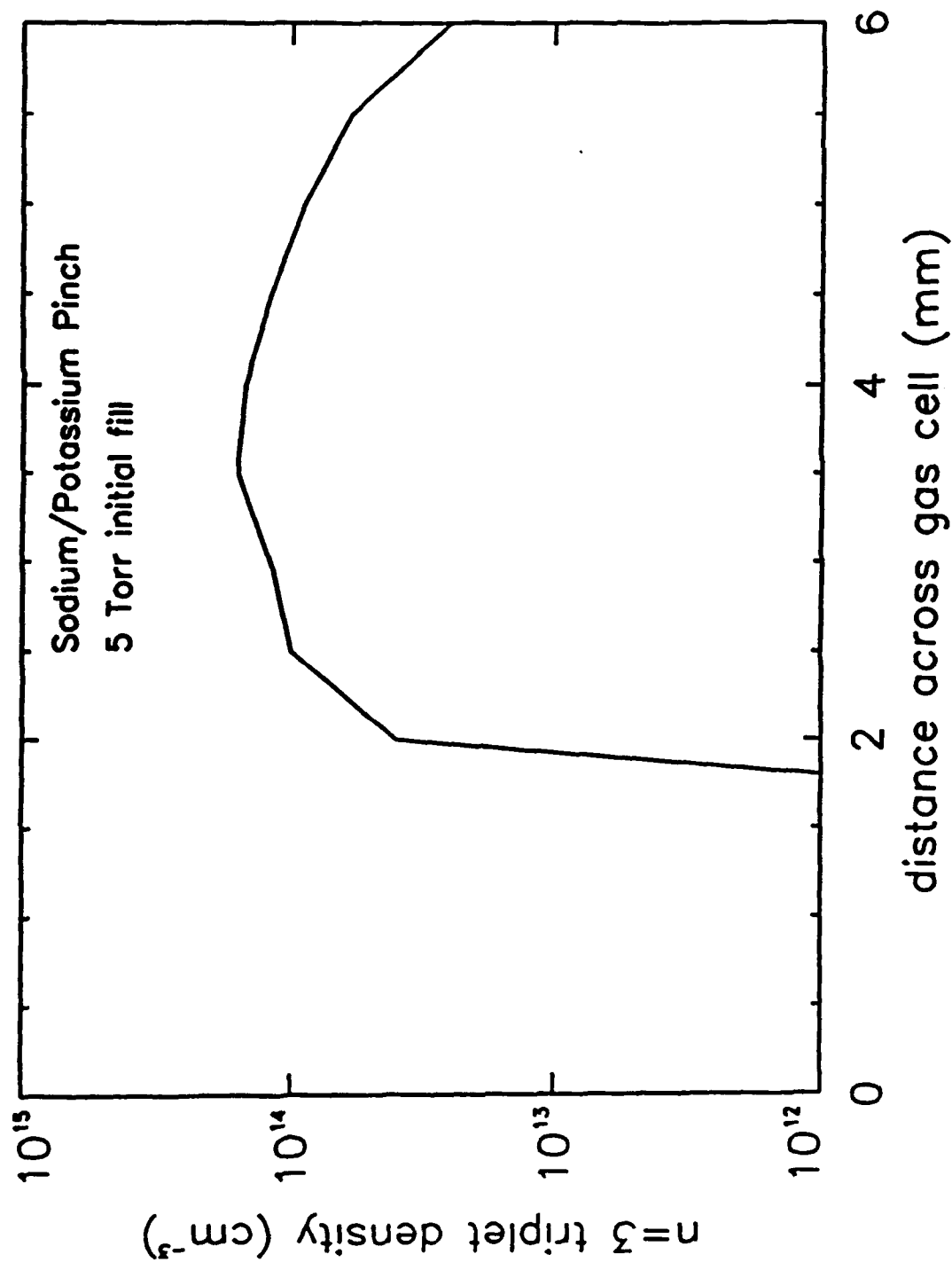
Varying both the assumed pump radiation and neon fill pressure obviously leads to differences in the calculated evolution of the target which aid in interpreting the experimental results. However, the basic hydrodynamic behavior of the target is a common thread which runs through all of the numerical solutions. The optical depth of the cold window is of order unity to the soft pinch x-rays in the 100 to 300 eV spectral region. As ionization proceeds, the window plasma becomes increasingly transparent to the pinch radiation, nonetheless absorbing enough energy to strip the carbon to the K shell, and behaving like a laser-driven exploding foil.²⁶ In accord with the similarity solutions of Reference 26, the present numerical results indicate window expansion velocities about 50% greater than the local isothermal sound speed (3×10^6 cm sec⁻¹ at 15 eV to which the window is heated). The window plasma pushes the much lower density neon 1.5 to 2.0 mm back from its original position during the approximate 30 nsec x-ray heating to the peak of the pump pulse. This creates a compressed, heated neon region about 1 mm thick of 35 eV temperature contiguous to the exploded side window plasma. The remainder of the 6 mm neon column remains

quiescent, heated purely by x-rays to temperatures of 10-15 eV. The existence of a 30 eV region has already been suggested by experimental measurements of the slope of the neon recombination continuum.²² Besides demonstrating the enhancement of ionization due to the potassium radiation, the present experimental data also verify the existence of the predicted shock-heated neon and window explosion, as now discussed.

One of the most revealing and critical areas for comparison of theory and experiment is the predicted versus measured spatial profile of the 78.3 Å triplet array in He-like neon. The intensity of this transition is proportional to the local He-like ground state density as well as the resonant photopumping rate to $n=4$. No collisional excitation from the He-like ground state occurs at the relatively low temperatures (<35 eV) of the target, whose high ionization state is principally produced by photons from the Z pinch.

In Figure 9 the calculated $n=3$ triplet population density at the peak of the x-ray pulse of a Na/K pinch is plotted versus position in the gas cell. In this calculation the measured spectral shape of the Na/K soft x-ray spectrum was used to drive the gas cell target. The temporal dependence of the pulse was assumed to be Gaussian with a FWHM of 35 nsec. Note the excellent qualitative correspondence between Figure 9 and the He-like trace in Figure 7. Both the measured and calculated peaks occur 3.5-4.0 mm to the rear of the original side retaining window. The calculation indicates that explosion of the window has pushed the carbon-neon interface back 1.8 mm from its original position. The spatially resolved experimental data of Figure 7 also indicates shock positions of 1-2 mm (some blurring occurs from integrating over the 10 nsec gate). The basic hydrodynamic processes occurring in these x-ray driven gas cell targets therefore appear to be well understood and characterized.

Since the ground state ionization thresholds of B-like, Be-like, and Li-like neon lie at 158, 207, and 239 eV, respectively, it is clear that the



9. The calculated He-like $n=3$ triplet population is plotted versus position in the gas cell at the peak of the x-ray pulse from the driving sodium/potassium pinch. The initial fill pressure is 5 torr. The original position of the gas cell side window is at 0.

large increase in spectral output in this region due to the introduction of potassium will enhance the ionization of the neon. The He-like neon fraction is calculated to vary from 55% for a pure Na pump with 10 torr fill pressure to 80% for a Na/K pump at 5 torr fill.

V. Conclusions

We have measured the ionization balance across a neon gas cell irradiated by a 10 TW z pinch. The measurements are consistent with a radiatively driven shock wave propagating through the neon. We have increased the overall level of ionization and the amount of He-like neon in the gas cell by introducing 25% potassium into the z pinch load. This increases the ionizing soft x-ray radiation a factor of 3. Oxygen absorption lines have also been eliminated from the spectrum by using an oxygen-free 5000 Å polystyrene end window.

VI. Acknowledgements

We would like to thank Larry Ruggles for his work in preparing and operating the MCPiGS instrument, Mark Vargas for preparing the sodium/potassium loads, John McGurn for operating XRDS and PCDS, Bob Ripple for operating the grazing incidence spectrometer that produced figure 5, and the Saturn crew for all the operational aspects of the x-ray laser runs.

VII. References

1. D.L. Matthews, et al., Phys. Rev. Lett 54, 110 (1985)
2. M.D. Rosen, et al., Phys. Rev. Lett. 54, 106 (1985)
3. B.J. MacGowan, et al., Phys. Rev. Lett. 59, 2157 (1987)
4. T.N. Lee, E.A. McLean, and R.C. Elton, Phys. Rev. Lett. 59, 1185 (1987)
5. S. Suckewer, et al., Phys. Rev. Lett. 55, 1753 (1985)
6. C. Chenaïs-Popovics, et al., Phys. Rev. Lett. 59, 2161 (1987)
7. P. Jaegle, et al., J. Opt. Soc. Am. B 4, 503 (1987)
8. D. Kim, et al., J. Opt. Soc. Am. B 6, 115 (1989)
9. J.C. Moreno, et al., Phys. Rev. A 39, 6033 (1989)
10. G. Jamelot, et al., Appl. Phys. B 50, 239 (1990)
11. V.A. Bhagavatula, J. Appl. Phys. 47, 4535 (1976)
12. J.P. Apruzese, et al., J. Appl. Phys. 53, 4020 (1982)
13. J.P. Apruzese and J. Davis, Phys. Rev. A 31, 2976 (1985)
14. J.P. Apruzese, et al., Phys. Rev. A 35, 4896 (1987)
15. F.C. Young, et al., Appl. Phys. Lett. 50, 1053 (1987)
16. J. Nilsen, Phys. Rev. 40, 5440 (1989)
17. B.N. Chichkov and E.E. Fill, Phys. Rev. A 42, 599 (1990)
18. Y.T. Lee, et al., J. Quant. Spectros. Rad. Transfer 43, 335 (1990)
19. J. Nilsen and E.A. Chandler, Phys. Rev. A 44, 4591 (1991)

20. J. Nilsen, J. Quant. Spectrosc. Radiat. Transfer 46, 547 (1991)
21. N. Qi and M. Krishnan, Phys. Rev. Lett. 59, 2051 (1987)
22. J.L. Porter, et al., Phys Rev. Lett. 68, 796 (1992)
23. J.P. Apruzese, et al., in Proceedings of the Second International Colloquium on X-ray Lasers, York, England, edited by G.J. Tallents (Institute of Physics, Bristol, 1991), p. 39
24. T.J. Nash, et al., Rev. Sci. Instrum. 61 2810 (1990)
25. D. Duston, R.W. Clark, J. Davis, and J.P. Apruzese, Phys Rev. A 27, 1441 (1983)
26. R.A. London and M.D. Rosen, Phys. Fluids 29, 3813 (1986)

Ultra Short Pulse Laser Produced Aluminum Plasma

J. Davis, R.W. Clark, and J. Giuliani, Jr.
Radiation Hydrodynamics Branch
Plasma Physics Division

ABSTRACT

The interaction of a subpicosecond laser pulse with a planar aluminum target is investigated. The interaction is described using a 1-D time-dependent non-LTE radiation hydrodynamics model in conjunction with a Helmholtz wave equation characterizing the laser-target coupling. In addition, a fraction of the absorbed laser energy is partitioned into energetic electrons that are transported and deposited into the cold un-ionized portion of the target. The radiative characteristics of the K_{α} and the K-shell line spectra are presented and discussed. The feasibility of creating conditions conducive to population inversion in selected transitions in lithiumlike aluminum is investigated.

INTRODUCTION

The interaction of a subpicosecond pulsed laser with a solid target produces a hot solid density plasma with a radiation signature that is characterized by an ultra short burst of energetic x-rays. The duration of the emitted radiation pulse is on the order of picoseconds and represents a potentially useful source of x-rays of interest for a variety of applications involving: ultra fast optics, picosecond spectroscopy, inner shell photo-pumping and recombination x-ray lasers, and chirped pulsed x-rays. However, before this new tool can be utilized we must first understand and characterize the properties and behavior of the plasma that generates the x-rays. This raises a number of issues, the first and most important involves describing how the laser energy couples to the cold solid target. Conventional wisdom suggests that for laser intensities less than about 10^{18} watts/cm² the dominant absorption mechanisms are thought to be multiphoton ionization initially followed and dominated by a combination of inverse bremsstrahlung and resonance absorption. Above 10^{18} watts/cm² absorption is more likely dominated by a variety of parametric plasma processes. Unfortunately, in general, there is no unanimity on what is the dominant absorption process and so it remains an open issue. A series of well thought out and well diagnosed experiments would provide a useful data base and starting point for addressing the absorption issue.

In this paper we treat the laser plasma coupling for intensities less than 10^{18} watts/cm² and for S polarization by means of a Helmholtz wave equation with an enhanced collision frequency. An enhanced collision frequency is employed in order to guarantee sufficient absorption and subsequent plasma heating to reproduce the observed spectra. In addition, in order to explain some of the observed features associated with the inner shell x-ray spectra, we have tacitly assumed that a fraction of the absorbed energy is partitioned into energetic electrons. These are transported and deposited in the un-ionized cold aluminum, producing local shock heating and inner shell vacancies. The K-shell vacancies are filled rapidly by either Auger decay or resonance fluorescence.

Numerical simulations are carried out for several KrF laser intensities ranging from 10^{16} to 3×10^{17} watts/cm² with pulse lengths of 650 femtoseconds normally incident on a 2μ thick planar aluminum slab. Comparisons are made for two laser intensities, two collision frequencies, and two beam energies.

MODEL

The calculations are based on a time-dependent 1-D collisional radiative radiation hydrodynamics model self-consistently coupled to a Helmholtz wave equation, describing the absorption of the laser pulse which is assumed normally incident on the target. The collisional radiative model contains all the ground states and selected excited levels distributed throughout the manifold of ionization stages. In particular, the K-shell manifold contains excited states up to and including the $n=10$ level and contains both singlet and triplet states in the heliumlike stage. The lithiumlike ionization stage also includes all levels up to $n=10$. The remaining ionization stages contain ground states and a variety of excited states important to the radiative energetics and diagnostics of the plasma. The ionization dynamics model is self-consistently coupled to a multi-cell probability of escape radiation transport scheme. The spectral line profile functions are represented by Voigt functions. A detailed discussion of the ionization dynamics and atomic processes, including the inner shell processes, are given in references 1 -3. The absorption of the normally incident laser pulse on the target is calculated by solving the Helmholtz wave equation for a multi-layered medium. In this way we self-consistently allow for the interaction of the incident, reflected and transmitted waves in each numerical zone in the medium. The resistivity was calculated using the collision frequency model of Cauble and Rozmus⁴, which is represented by ν_0 . A fraction of the absorbed energy, in our case 30%, was partitioned into energetic electrons. These electrons were slowed down and deposited their energy according to the Bethe-Bloch approximation. The simulations were performed for

energetic electrons consisting of either a 10 KeV or 4 KeV beam energy and for collision frequencies 10X and 100X ν_0 respectively.

RESULTS

The rate at which a Gaussian profile laser pulse of FWHM 650 fsec 248 nm KrF laser pulse of 10^{16} watts/cm² is deposited into a 2 μ thick aluminum target is shown in Fig. 1 as a function of position at 0.4 psec. The laser pulse is assumed incident on the target from right to left. At this time about 14% of the laser power is deposited in the target. Also shown in Fig. 1 are the mass density and the ratio of the local electric field, averaged over an optical cycle, $\langle E \rangle$, to the amplitude of the incident electric field, E_0 , as functions of position. The location of the critical surface, i.e. where $\omega = \omega_p$ is represented as R_{critical} . There is an enhancement of $\langle E \rangle / E_0$ at about 2.08 μ that represents the constructive interference between the incident and

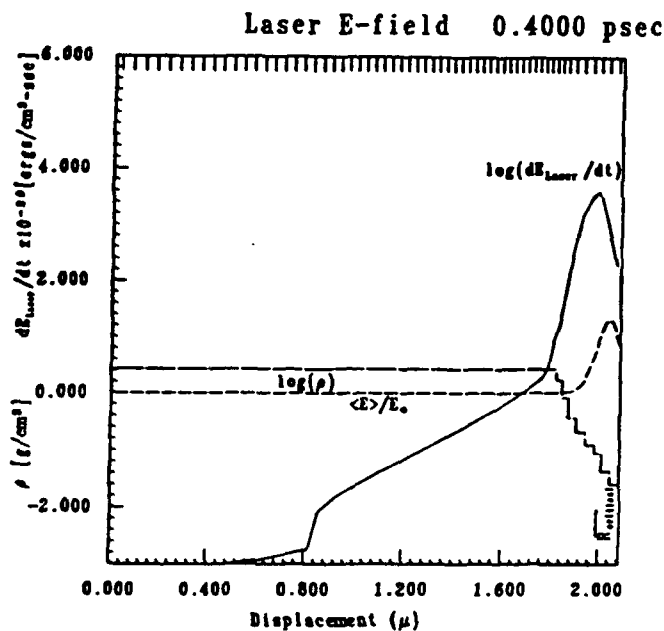


Fig. 1. Laser energy deposition at 0.40 picoseconds.

The logarithm of the rate of energy deposition into the target $\delta E_{\text{Laser}}/\delta t$ is plotted, and the location of the critical surface R_{critical} is shown. The local electric field, averaged over an optical cycle, $\langle E \rangle$ is shown normalized to the amplitude of the incident field E_0 . The mass density ρ is shown in a stepwise manner to indicate the spatial resolution of the simulation in the deposition region.

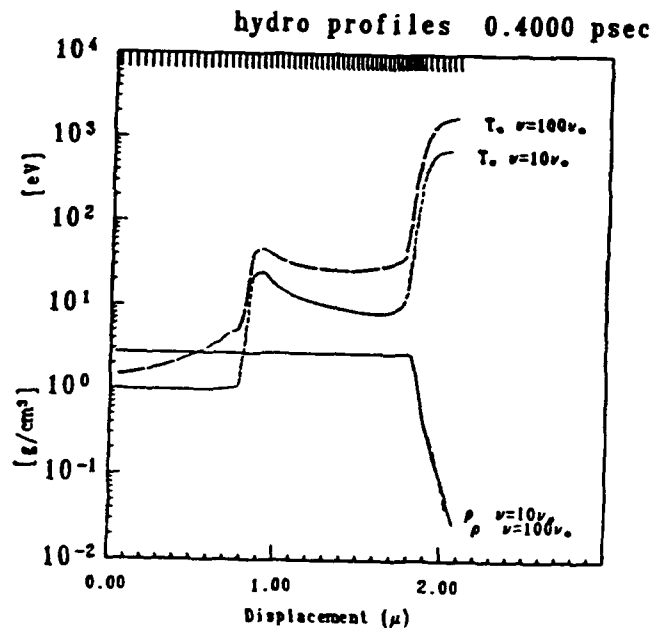


Fig. 2. Hydrodynamic profiles at 0.40 picoseconds.

Spatial profiles of mass density and temperature are plotted near the peak of the laser pulse. Two effective collision frequencies are compared for a laser intensity of 10^{16} W/cm²: $10\nu_0$ and $100\nu_0$.

reflected waves. The mass density, $\log(\rho)$, is plotted in "staircase" mode to emphasize the spatial resolution of the numerical grid. At this time only a very weak shock wave due to the deposition appears at about 1.86μ . Figure 2 shows the hydrodynamic profiles at 0.4 psec for $10v_0$ and $100v_0$ as a function of distance. These profiles include the effects of the deposition due to an energetic beam of 10 KeV electrons containing 30% of the absorbed energy. Since there is little expansion of the leading edge of the blowoff plasma at this early time the density profiles remain essentially the same. On the other hand, the temperature profiles are significantly different. As a result of the enhanced $100v_0$ collisional and beam heating a higher temperature profile is produced both in the laser deposition region and deeper into the target than in the $10v_0$ case. Also, as a consequence of the beam deposition there is an additional local heating causing a second weak shock wave deep in the cold aluminum. The temperature differential between these two collisional cases is simply the result of distributing more of the absorbed energy into thermal energy in the $100v_0$ case than the $10v_0$ case. In the absence of an energetic electron beam, the temperature profile initially would be dominated mostly by thermal conduction from the laser deposition region and exhibit a rapid decay into the cold aluminum. These differences are easily observed and identified in the x-ray spectra.

In Figures 3 and 4 are shown the spatially integrated and time resolved intensity of the x-ray emission spectra for the K_α lines and K-shell lines as a function of photon energy at 0.4 psec for an incident laser intensity of 10^{16} watts/cm² with a 10 KeV beam for 10 and $100v_0$, respectively. The lines are identified and labeled on the Figures. The most notable and distinguishing feature on these Figures is the series of K_α lines generated by the energetic electrons. Another obvious feature on Fig. 4 is the enhancement (by almost an order of magnitude) of the free-bound continuum which is observable over the entire photon range shown. Only a brief glimpse of the free-bound continuum is visible around 1.4 KeV on Fig. 3. The differences in the intensity of the K_α lines are due to the enhanced collisionality. The primary reason for this is the change in the plasmas' reflectivity. Although the beam energy is the same in both cases the collisionality differs by a factor of ten between the two cases leading to a factor of 3 increase in the absorption properties of the plasma. Spectroscopically, the K_α signatures and their intensity distribution represent a useful diagnostic for determining the effects of the energetic electrons. They also represent a substantial fraction of the radiated x-ray line energy. The other interesting feature appearing on these Figures is the presence of some of the K-shell lines, in particular the hydrogen-like lines. For the $100v_0$ case the spectra contains lines from both the helium- and hydrogen-like ionization stages with the heliumlike resonance line dominating the K-shell spectra. The hydrogenlike resonance line is about equal

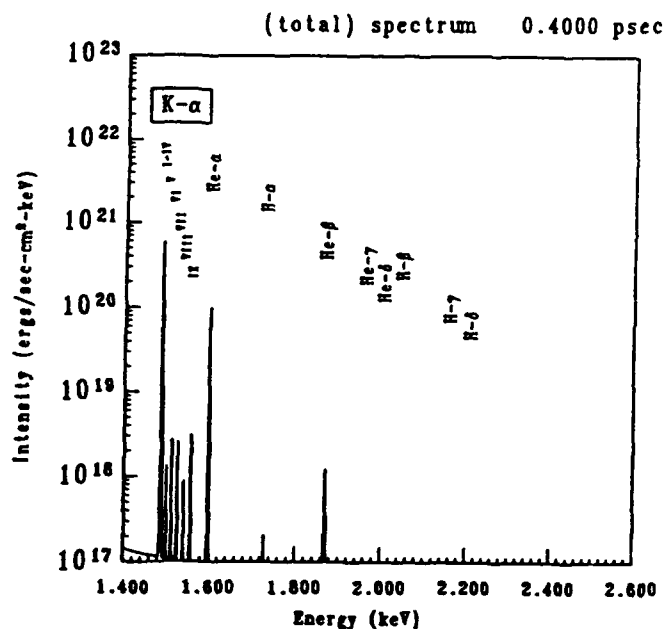


Fig. 3. Emission spectrum at 0.40 psec for $\nu = 10\nu_0$.

Instantaneous emission spectrum near the peak of the laser pulse showing magnitudes of the K_α and K-shell lines. The collision frequency has been enhanced by a factor of 10. Helium- α emission and K_α radiation from the lower ionized states of aluminum dominate the spectrum.

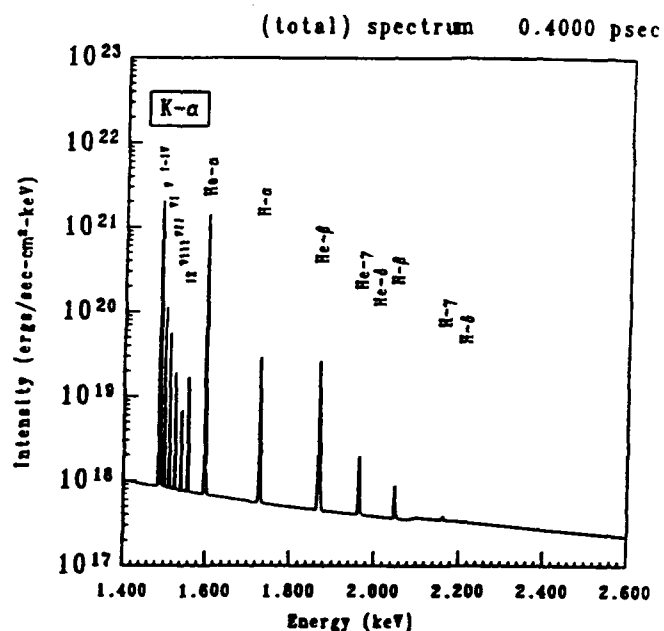


Fig. 4. Emission spectrum at 0.40 psec for $\nu = 100\nu_0$.

Instantaneous emission spectrum near the peak of the laser pulse with the collision frequency enhanced by a factor of 100. The reduction in the reflectivity produces a hotter plasma, evidenced by the presence of H-like emission and enhanced K_α radiation from aluminum V-IX.

in magnitude to the Heliumlike β line indicating that the temperature of the emitting region is insufficient to populate the hydrogenlike levels and is more readily conducive to populating the upper levels of the heliumlike states. Both are significantly less than the heliumlike resonance line by about a factor of 50. For the $10\nu_0$ case the plasma is radiating predominantly from the heliumlike resonance line. Ultra short pulse laser aluminum target experiments performed at 10^{16} watts/cm² produce an emission spectra much like the $10\nu_0$ case where hydrogenlike spectra are absent and only the heliumlike and K_α lines appear. ⁵

Figures 5 and 6 represent the total integrated spatial and spectral intensity up to 620 femtoseconds for an incident laser intensity of 10^{17} watts/cm² and an enhanced collisionality of $100\nu_0$ for electron beam energies of 4 and 10 KeV, respectively. The significant spectral differences between these two cases is the intensity and distribution of the K_α lines and the magnitude of the underlying continuum. These observations could be used as a diagnostic to infer plasma conditions. The heliumlike resonance line radiates like a beacon and dominates the K-shell spectrum in both cases. However, at a laser intensity of 10^{17} watts/cm² and a 100 fold increase in the collision frequency the plasma is hot enough to sustain and radiate significant amounts of both helium- and hydrogen-like lines. The slight difference in the

magnitude of the underlying continuum between the two cases is due to the increased free-bound recombination radiation in the 4 KeV beam case due to the cooler temperature in the target as a result of the lower beam energy. This behavior is also reflected in the distribution and intensity of the K_{α} lines.

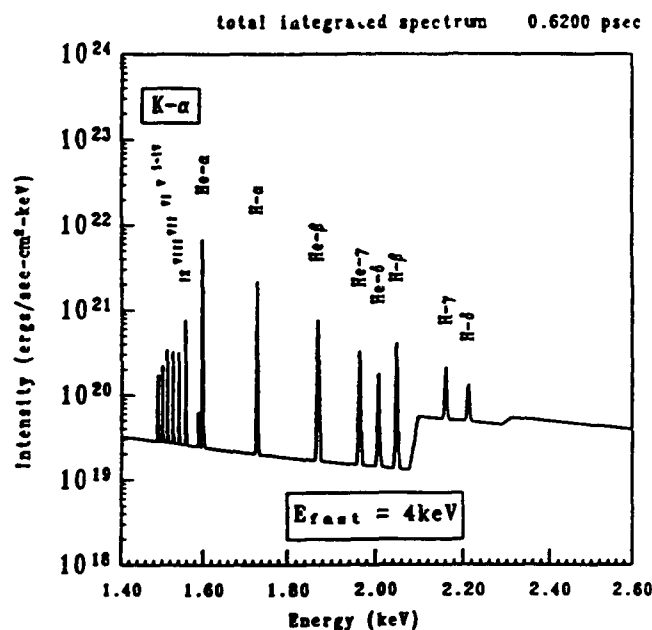


Fig. 5. Integrated Emission spectrum for $E_{beam} = 4keV$.

Emission spectrum time-integrated over the laser pulse for 4 keV fast electrons. K_{α} radiation from the lower ionized states of aluminum is relatively weak, since fast electrons are being deposited in hot plasma near the critical surface.

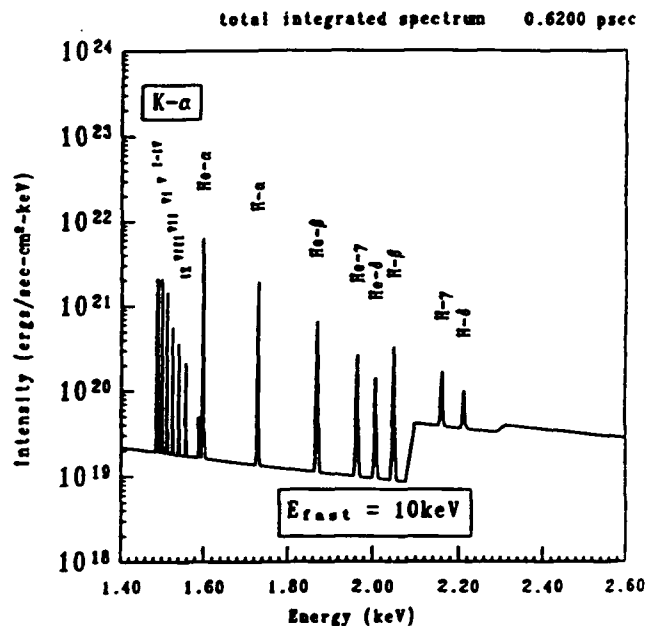


Fig. 6. Integrated Emission spectrum for $E_{beam} = 10\text{keV}$.

Emission spectrum time-integrated over the laser pulse for 10 keV fast electrons. K_{α} radiation from the lower ionised states of aluminum is now dominant, since many energetic electrons are being deposited in the cool interior of the target.

Finally, we have investigated the possibility of plasma conditions being generated that are conducive to creating population inversions in selected levels in lithiumlike aluminum. For the case of a laser intensity of 3×10^{17} watts/cm² with a 100 fold increase in collisionality and a beam energy of 10 KeV, preliminary results indicate that the temperature and density profiles midway from the leading edge of the blowoff plasma do support population inversions in a number of upper states. As an example, we present results for the $n=8$ principal quantum number of lithiumlike aluminum in Fig. 7. The energy levels and their energies relative to the

ground state are shown along with the ratio of fractional population of the upper to lower level, i.e., $(f_u/g_u)/f_l/g_l$ where $f_{u,l}$ and $g_{u,l}$ represents the fractional population and statistical weight of the upper and lower level, respectively. The results of these simulations provide encouraging data supporting the idea that it is possible to create inversions over timescales of interest. Whether the existence of population inversions can successfully lead to lasing with a gain length is still under active investigation.

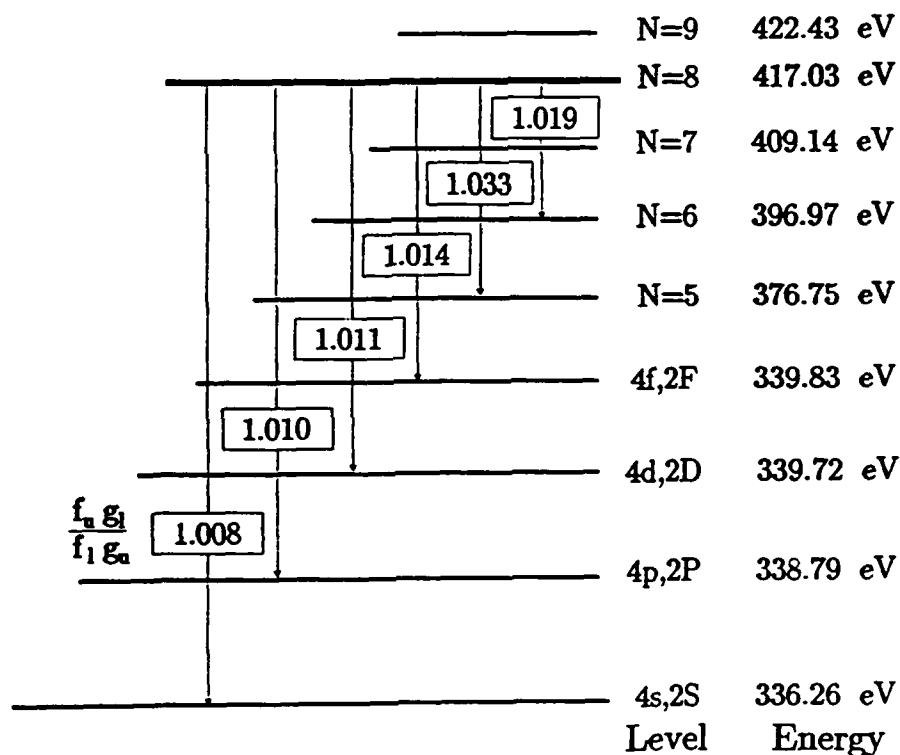


Fig. 7. Population Inversions in Li-like Aluminum.

Ratio of Lithium-like fractional populations $f_u g_l / f_l g_u$ at 0.48 picoseconds for $x=1.82\mu$ (0.05μ behind the critical surface). Population inversions among the atomic levels (mainly $N > 3$) are produced at this time. Those relative to the $N = 8$ level are shown above.

Acknowledgment

We would like to thank Dr. P. Kepple for making the atomic data base available.

References

- 1. D. Duston, R. Clark, J. Davis and J. Apruzese, Phys. Rev. 27, 1441, 1983.**
- 2. D. Duston, R. Clark and J. Davis, Phys. Rev. 31A, 3220, 1985**
- 3. V. L. Jacobs, J. Davis, B.F. Rozsnyai, and J. Cooper, Phys. Rev. A 21, 1917, 1980.**
- 4. R. Cauble and W. Rozmus, J. Plasma. Phys. 37, 405, 1987.**
- 5. D. Meyerhofer, " Progress Towards a Picosecond X-ray Tube", Preprint June 26, 1992.**

**Escape time of heliumlike alpha resonance line photons
emitted from optically thick plasmas**

J. P. Apruzese

**Radiation Hydrodynamics Branch
Plasma Physics Division**

ABSTRACT

The heliumlike alpha resonance line is one of the strongest and most frequently observed transitions in plasma spectroscopy. In optically thick plasmas of moderate density, photons emitted in this line typically undergo many absorptions and re-emissions before escaping. In the present investigation the time required for this process to occur in aluminum plasma is calculated by numerical solution of the time-dependent equation of radiative transfer, in which the photon transit time between interactions is taken into account. An analytic model is also developed in which the collisional quenching probability is parameterized in terms of an equivalent two-level atom. This model facilitates interpretation of the numerical results, and permits economical estimates of the escape time for different plasma elements and conditions. One practical implication of these results is that a subpicosecond x-ray pulse from a femtosecond laser-produced high density plasma can be broadened by multiple scattering if it propagates into a moderate-density preformed plasma.

I. INTRODUCTION

The $1s^2-1s2p^1P_1$ principal resonance line of the heliumlike ion (designated He- α) is one of the most frequently observed lines in plasma spectroscopy. It has been detected in devices ranging from tokamaks to inertial confinement fusion capsules to Z pinches. Most recently, this line has appeared prominently in the spectra of targets irradiated by high power sub-picosecond lasers.

For elements with atomic number Z between 4 and 50, the oscillator strength of this transition [1] exceeds 0.5, hence it is usually optically thick for moderate to high density plasmas. The associated rapid spontaneous decay rate means that absorption of a line photon is often followed by re-emission within the line profile (referred to as scattering). Thus, much of the line energy that escapes the plasma does so after diffusion in both position and frequency, which can affect the intensity and width of the x-ray pulse. For multnanosecond sources such as the dense Z pinch, this effect is expected to be small compared to the inherent lifetime of the plasma. However, this may not be the case for the very short lived plasmas produced by the current generation of powerful subpicosecond lasers [2-12]. Numerous uses of such plasmas are envisioned, prominently among them the production of ultrashort x-ray pulses [2,4,5,12-16].

One interesting phenomenon which has been identified and quantified to some degree is the effect of a laser prepulse on the characteristics of the x-rays emitted from such short-lived plasmas. The Los Alamos group [7, 17] and others [10] report that the presence of a prepulse has a strongly positive effect on the plasma x-ray yield. This occurs whether the prepulse is of nsec [7,17] or sub-psec [10] duration. With a prepulse present, the preformed plasma may have time to expand, and, as pointed out in Refs. 14-16, expansion and thermal conduction are potentially important cooling mechanisms in these plasmas. The greater the scale length, the more these mechanisms tend to broaden the x-ray pulse. A tradeoff between yield and pulsewidth thus appears to be indicated.

It is the relatively large preformed plasmas producing the best x-ray yields which are also the most likely to be affected by pulse broadening inherent in the multiple scattering of strong x-ray lines. The purpose of the present work is to quantify the escape time of the He- α line radiation. Section II presents the numerical and analytic models of radiation transport used in the calculation. The numerical calculations are done for aluminum which has been a frequent experimental target

for sub-psec lasers [5,7,10,17], and from which the He- α line has been strongly detected. In Sec. III, the validity of the analytic model is assessed by direct comparison with numerical results. The analytic model is extendable to elements other than aluminum. Results for different plasma conditions are also presented and discussed.

II. RADIATION TRANSPORT

A. Numerical model

The time-dependent transport of radiation of frequency ν along a ray in the positive x direction is described by the equation of transfer

$$\frac{\partial I_\nu}{\partial x} = j_\nu - k_\nu I_\nu - \frac{1}{c} \frac{\partial I_\nu}{\partial t}. \quad (1)$$

In eq. (1), I_ν is the specific intensity, j_ν and k_ν are the emission and absorption coefficients, and c is the velocity of light. For a derivation of this equation see, e.g., Ref. 18. Consider the spacetime point (x_0, t_0) . Looking in the negative x direction, the quantities determining $I_\nu(x_0, t_0)$ are j_ν and k_ν encountered at retarded times $t_r(x_0, t_0, x) = t_0 - \frac{(x_0 - x)}{c}$. The effective optical depth between x_0 and x at time t_0 is

$$\tau_\nu(x_0, t_0, x) = \int_x^{x_0} k_\nu(t_r) dx \quad (2)$$

and the solution to eq. (1) is

$$I_\nu(x_0, t_0) = \int_{x_b}^{x_0} j_\nu[x, t_r(x)] \cdot \exp[-\tau_\nu(x_0, t_0, x)] dx. \quad (3)$$

In eq. (3), x_b is the coordinate of the plasma boundary. In all cases to be considered, it is assumed that no external x-rays are incident on the plasma. Given the emission and absorption coefficients from previous time steps, eq. (3) is numerically solved on a grid of 31 frequency points within the line profile and a spatial mesh of 26-31 points per ray. Linear interpolation in both space and time is employed for j_ν and k_ν . The maximum time step employed is 10 fsec. To compute photoexcitation and escape rates, the angle-averaged intensity J_ν and net radiative flux F_ν are needed. This requires an assumption for the shape and dimensionality of the medium. The present work will be confined to one-dimensional plane-parallel geometry. The numerical burden of including full time dependence in the radiative transfer is kept at an acceptable level with this

simple choice of geometry. Also, the optical depth presented to an escaping line photon can be unambiguously characterized and associated with a calculated escape time or probability. This will facilitate analysis of future multidimensional work more representative of actual laboratory plasmas.

The distribution of the rays follows Gaussian quadrature as described by Chandrasekhar in Ref. 19. Each ray is characterized by the cosine of its angle ($\mu = \cos\theta$) to the planar normal. In the present work both four rays and two rays have been employed for comparison. Their specific μ 's are given in Table III of Ref. 19. In planar, one-dimensional geometry the quantities J_ν and F_ν are given by

$$J_\nu = \frac{1}{2} \int_{-1}^{+1} I_\nu(\mu) d\mu \quad (4)$$

and

$$F_\nu = 2\pi \int_{-1}^{+1} I_\nu(\mu) \mu d\mu. \quad (5)$$

The line photon escape rate is the frequency integral of F_ν at the plasma boundary. The photoexcitation rate for a spectral line of absorption oscillator strength f_{lu} from lower level l to upper level u is given by

$$W_{lu}(\text{sec}^{-1}) = \frac{\pi e^2}{mc} f_{lu} \int \frac{4\pi J_\nu}{h\nu} \phi_\nu d\nu \quad (6)$$

where the integral is taken over the line profile ϕ_ν whose normalization is $\int \phi_\nu d\nu = 1$. Given the photoexcitation rates as well as the appropriate set of collisional rates, populations of the various levels and ionic stages are obtained as a function of time by numerical integration of the atomic rate equations (see, e.g., eq. (1) of Ref. 20). The method of Young and Boris [21] is employed as it is especially well suited to the time integration of numerically stiff differential equations.

B. Analytic model

The two-level-atom approximation has been treated extensively in the astrophysical literature (see, e.g., Ref. 22 and references therein). It is therefore a natural starting point for an analytic description of the radiative transfer within the He- α line. Even though the heliumlike ion is obviously not a two-level system, the same processes of scattering and collisional quenching are

operative in determining the fate of the emitted line photons. Upon absorption, the photon will either be re-emitted or various other processes will transfer the $1s2p^1P_1$ electron elsewhere. For the idealized two-level-atom case, "elsewhere" is only the ground state. For the real heliumlike ion, the electron can in principle end up almost anywhere within the same ion or the adjoining hydrogenic or lithiumlike species. One cannot obtain a probability of collisional quenching (designated ϵ) by merely adding the rates to all other possible levels from $1s2p^1P_1$, since in some cases the electron is collisionally shunted right back to the original upper level of the transition. It is necessary to subtract (for each transition) the probability that the electron returns to the $1s2p^1P_1$ level.

If the electron is transferred to level i from the $1s2p^1P_1$ state the probability of return to the $1s2p^1P_1$ level P_{ri} is defined as the rate from level i back to $1s2p^1P_1$ divided by the sum of all of the rates out of level i . The net quenching probability ϵ is then given by

$$\epsilon = \frac{\sum C_i(1 - P_{ri})}{A_{ul} + \sum C_i(1 - P_{ri})} \quad (7)$$

In eq. (7), C_i is the rate from $1s2p^1P_1$ to the i th level, A_{ul} is the spontaneous decay rate of the resonance transition, and the sum is taken over all levels connected to $1s2p^1P_1$.

The quenching probability ϵ has been computed for Al using the atomic data described in Ref. 20. From the $1s2s^1S_0$ level the chance of return to the $1s2p^1P_1$ level is appreciable (0.92 at an electron density of 10^{21} cm^{-3} near temperatures of 200 eV). At these same conditions, the net probability of collisional quenching of the Al He- α line per absorption (ϵ) is 0.029.

Line photons may also be eliminated from the plasma by escape. The probability P_e that the photon escapes a medium of a given optical depth is obtained from a weighted average of the exponential escape probability at each frequency within the line profile. The weighting factor is the strength of the profile itself at each frequency. Detailed treatment of escape probability calculations may be found in Refs. 23-27. For stationary media, useful analytic forms have been obtained for Doppler [23,24], Voigt [25], and Stark [26,27] line profiles. The Doppler shift due to bulk motion can influence P_e in some instances. For media where this is important, the original work of Sobolev [28] has recently been extended by Shestakov and Edser [29] to include cylindrical geometry.

The quantities ϵ and P_e discussed above, along with the spontaneous decay rate of the upper level A_{ul} , suffice for an approximate analytic description of line photon escape and transport. The

probability that a photon escapes after an excitation is $(1 - \epsilon)P_e$, whereas the probability that it remains within the plasma is $S \equiv (1 - \epsilon)(1 - \epsilon_e)$. The probability that the photon has escaped by the N^{th} scattering is the sum of the probabilities of escape after initial excitation and each of the subsequent scatterings, viz.

$$P_N = (1 - \epsilon)P_e \left[1 + \sum_{n=1}^N S^n \right] = (1 - \epsilon)P_e \left[\frac{1 - S^{N+1}}{1 - S} \right] \quad (8)$$

The ultimate escape probability is obtained by taking the limit of eq. (8) as $N \rightarrow \infty$, $P_u = P_e \left(\frac{1 - \epsilon}{1 - S} \right)$. The time required for N scatterings, i.e., the time associated with line photon probability of escape P_N , including the initial excitation but ignoring the photon travel time between absorptions, is simply the level lifetime A_{ul}^{-1} multiplied by $N+1$. Thus, P_N given by eq. (8) is equivalently $P(t)$, where $t = \frac{N+1}{A_{ul}}$. This analytic form for the fraction of line photons which have escaped as a function of time is compared in the next section with numerical results. It is straightforward to obtain an explicit expression for the time for fractional escape f_e (of the photons which ultimately escape). The condition is $f_e = 1 - S^N$, which leads to

$$t(f_e) = A_{ul}^{-1} \left[\frac{\ln(1 - f_e)}{\ln S} + 1 \right] \quad (9)$$

and in the limit $P_e, \epsilon \ll 1$,

$$t(f_e) = A_{ul}^{-1} \left[\frac{\ln(1 - f_e)}{-(P_e + \epsilon)} + 1 \right]. \quad (10)$$

It is possible to construct an analytic model using three or more levels. However, as pointed out in Ref. 30, the algebra quickly becomes unmanageable. Moreover, as seen below, the equivalent two level approach yields respectable accuracy as well as considerable physical insight. Note also that a single P_e is employed despite the fact that in principle it varies between subsequent scatterings when the photon is emitted from a different position in the plasma. However, as has been shown previously [31,32], the line photon usually remains imprisoned within the line core and stays close to its location of previous emission, escaping in one long flight when emitted in the line wing. Although somewhat oversimplified, this picture explains the success of this approximation in both the present and previous work. As evident in the next section, some spatial diffusion of the excitation does occur.

III. RESULTS

A. Equivalent two-level-atom

The calculations presented in this section have two principal objectives. First, to assess whether under the chosen conditions transport of the principal resonance line of the heliumlike ion can be understood and parameterized as if the ion consisted merely of a ground and one excited state. Second, to establish the numerical parameters needed to insure accuracy in the computation.

As stated above in Sec. II B, at an electron density of 10^{21} cm^{-3} , and temperatures around 200 eV the net probability of collisional quenching per absorption for the Al He- α line is 0.029. A two-level-atom test case is chosen to correspond to this value. At this density, the line is well described by a Voigt profile whose broadening parameter $a=0.05$. A planar Al plasma of width 100 μm would have about 90% of its ions in the heliumlike stage under these conditions. The line center optical depth τ_0 of the He- α line, measured normally from the midplane to plasma boundary, is 90. These are the conditions for which the present calculations were run; obviously, no extensive atomic data file is required for this simplified case. The plasma is assumed stationary (i.e., bulk Doppler motion is neglected in the radiative transfer). To examine the diffusion and escape of line photons the following initial excitation conditions are assumed: the ions are entirely in the ground state except for the spatially innermost 12% where 1% of the ions are in the excited state, see Fig. 1. The clock starts at $t=0$ and the line photons begin escaping and migrating toward the plasma boundary. The collisional excitation rate is set to zero as if the plasma cools instantaneously. In this fashion, the spatial diffusion and escape times obtained reflect only the effects of radiative transfer.

The upper level fraction as a function of space and time is illustrated in Figs. 1 and 2 for 5 time points varying from 0 to 7 psec, for both 4-ray and 2-ray Gaussian quadrature. Note first the excellent agreement between the $n=2$ and $n=4$ cases, strongly suggesting that 2 rays are adequate. Spatial diffusion of the upper level population due to line photon absorption and re-emission is clearly evident. Of considerable interest is the rate of decay of the upper level population in the central zone. If the plasma were optically thin, this population would decrease with an e-folding time of $A_{ul}^{-1}=36 \text{ fsec}$. The actual lifetime is much greater in the optically thick medium because of re-excitation of the level by line photons, as is evident in Figs. 1 and 2. For the first 0.5 psec, the effective lifetime of the upper level is 0.7 psec, increasing to 1.1 psec for the final 3 psec covered

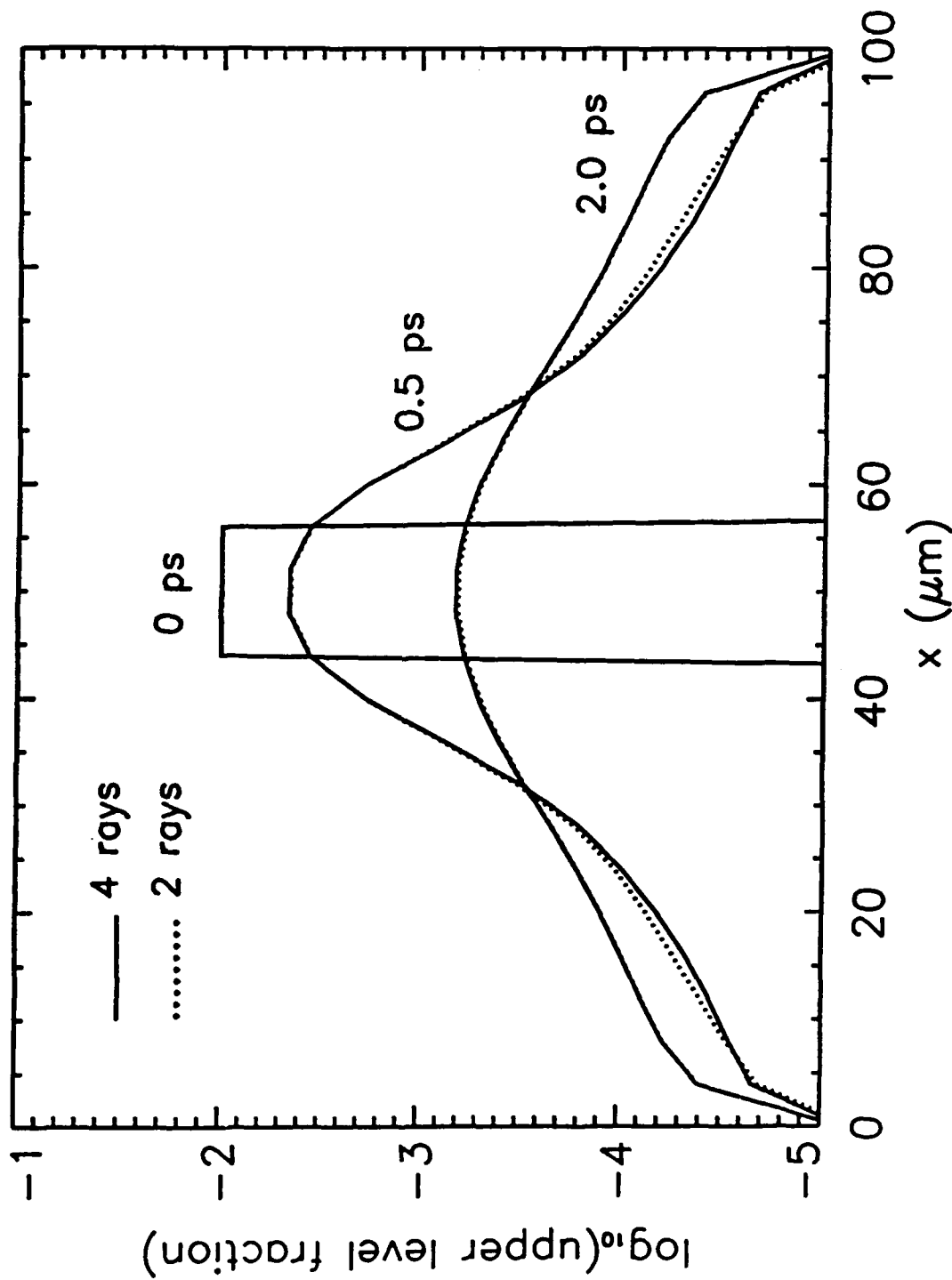


FIG. 1. Al XII $1s2p^1P_1$ population fraction is shown as a function of space and time in the two-level-atom approximation at 0, 0.5, and 2.0 psec following initial excitation. The plasma is planar, $100 \mu\text{m}$ thick, with an assumed temperature of 200 eV and electron density 10^{21} cm^{-3} . Differing assumptions of the various calculations are as indicated in the figure and discussed in the text.

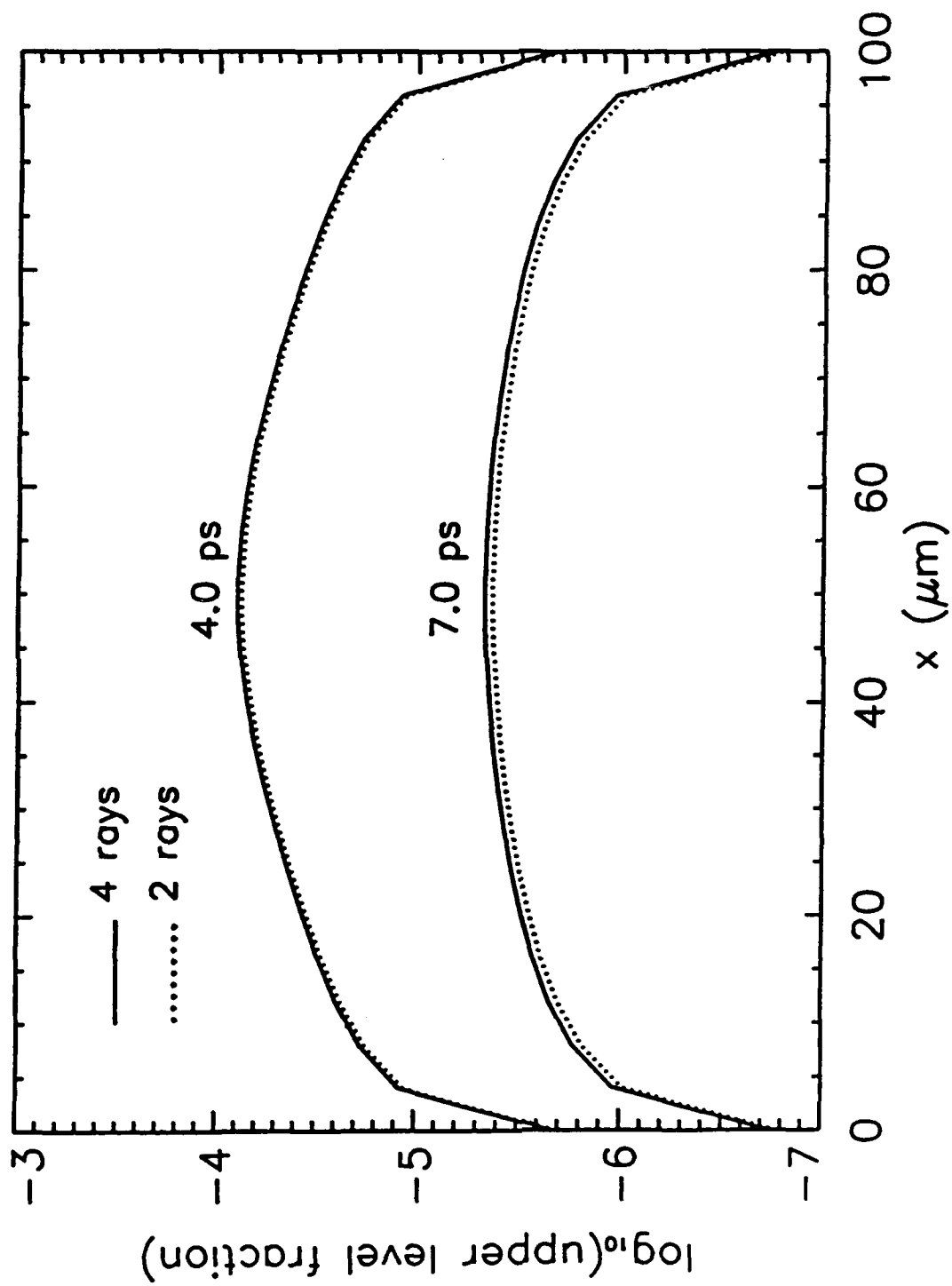


FIG. 2. As in Fig. 1, except that times of 4.0 and 7.0 psec after initial excitation are illustrated.

by Figs. 1 and 2. A frequently used approximation for line transfer is to multiply the spontaneous decay rate by the escape probability, to obtain an effective decay rate which compensates for re-absorption. The results of Ref. 25 may be used to obtain a planar average escape probability P_e of 8.9×10^{-3} for this case. Including the effects of collisional depletion of the upper level, the total effective decay rate is $\sim A_{ul}(P_e + \epsilon) = 1.05 \times 10^{12} \text{ sec}^{-1}$, implying a lifetime of 0.95 psec. This value is very close to the average e-fold time observed in Figs. 1 and 2. Transient delays in re-excitation result in an initially more rapid population falloff, but this phenomenon damps out over 7 ps, resulting in good correspondence between the analytically estimated and numerically computed upper level decay times.

The time profile of escape of the He- α line photons is illustrated in Fig. 3 where numerical results are plotted along with the analytic solution of eqs. (8) and (9). As indicated in that figure, one of the numerical calculations ignored the time-dependent term in eq. (1), therefore implicitly neglecting the photon travel time. The analytic solution also neglects this effect. The numerical solutions which do include full time dependence were obtained for both 2 and 4 Gaussian rays, and, as evident in Fig. 3, the agreement is excellent. All results presented in succeeding sections were therefore obtained using the more economical 2 ray approximation.

The asymptotic or ultimate escape probability $P_u = P_e(\frac{1-\epsilon}{1-\epsilon})$ is 0.23 for the escape and quenching probabilities quoted above. Most of the emitted He- α photons do not escape, since the quenching probability ($\epsilon = 0.029$) exceeds that of escape ($P_e = 8.9 \times 10^{-3}$) by a factor of 3. The fully time dependent numerical solutions depart from the analytic result in several details. First, the photons do not emerge immediately since 170 fsec is required to traverse the 50 μm from the center to the outer boundary of the plasma. Also, about 28% of the initially created line photons escape rather than the 23% given by the analytic solution. This is not particularly surprising since the fixed escape probability is computed from the plasma midplane but the photons diffuse spatially toward the boundary and therefore should not strictly obey a single escape probability. According to the fully time dependent numerical calculation, 1.3 psec is required for 50% of the photons to escape. Achieving a subpicosecond x-ray pulse in Al He- α may be difficult for a plasma like the present one where the line scatters many times prior to escape. Note that recombination of the heliumlike species occurs on a timescale of $\geq 10 \text{ psec}$ [5], even for electron densities of $\sim 10^{22} \text{ cm}^{-3}$. Therefore it will not eliminate the source of the multiple scattering during the x-ray

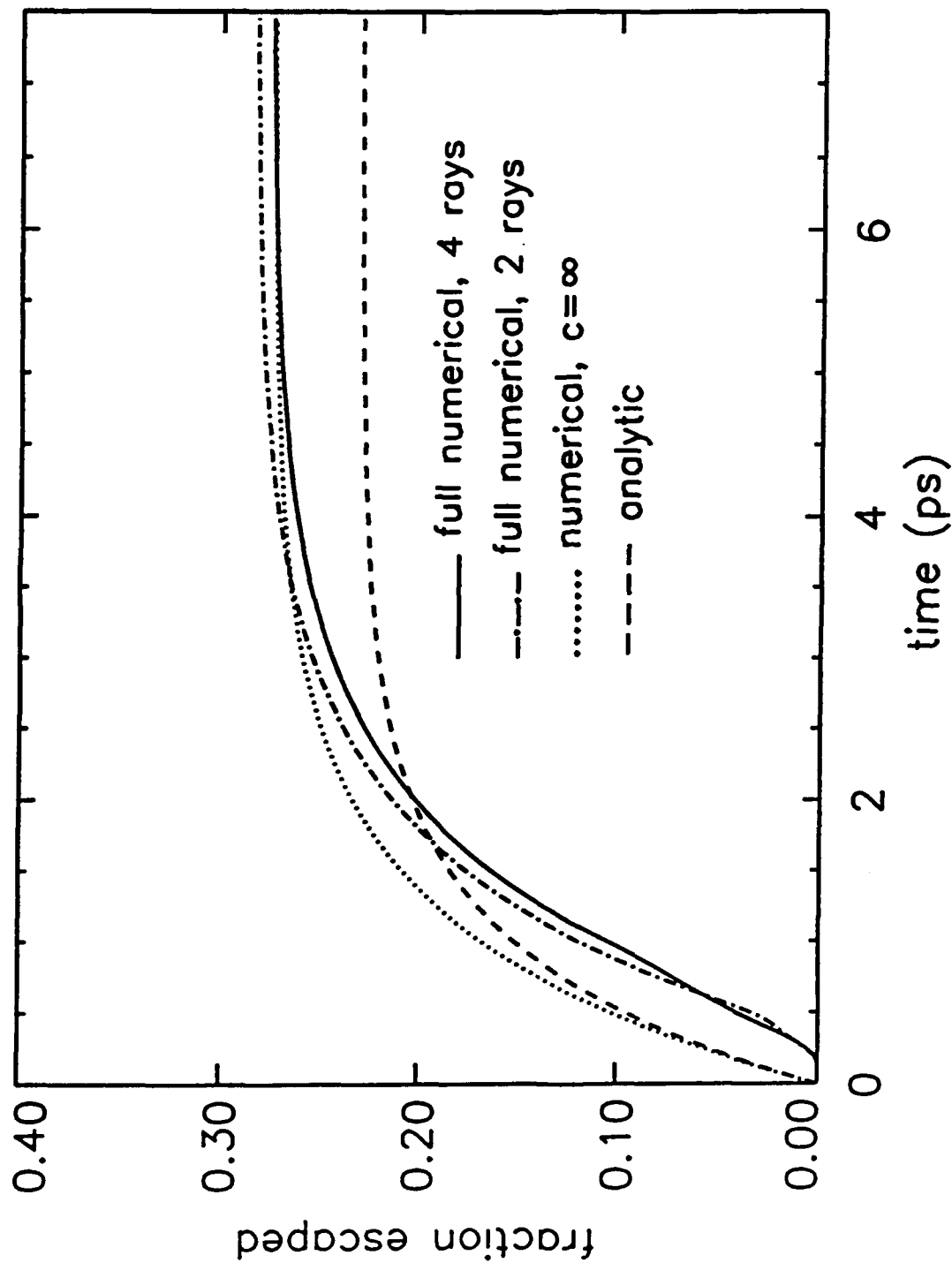


FIG. 3. Escaped photon fraction for the Al He- α line is illustrated for the conditions of Figs. 1 and 2 as a function of time. Numerical calculations using 4 Gaussian rays assuming both the correct and infinite light velocity are shown, as well as 2 ray and analytic approximations discussed in the text.

pulse. For near solid density plasmas, three-body recombination is fast enough to short-circuit this mechanism. More general conditions and assumptions are now examined, and more favorable plasma properties conducive to shorter pulses are considered.

B. Multilevel aluminum plasma

In this subsection, the simplifying approximation of a parameterized two-level-atom is dropped and the escape and diffusion of the He- α line is examined with a multistage, multilevel atomic model for aluminum ions. Due to the expense of such fully time-dependent calculations, it was not feasible to do a truly comprehensive set of runs closely covering all of the expected conditions where such effects might be important. Nevertheless, with the aid of the analytic model discussed above and the atomic number scaling considerations presented below, essential conclusions can be drawn for much of the important physics as applied to frequently achieved conditions in laboratory experiments.

The aluminum atomic model emphasizes the heliumlike stage where excited levels are carried ranging through $n=7$. Triplet and singlet sublevels are modeled for $n=2$ and $n=3$, but $n=4$ through $n=7$ are treated as Rydberg levels in which the triplets and singlets are assumed to be populated statistically. A total of 33 ground and excited states are included in the neutral through bare nuclear stages. The heliumlike rates affecting the $n=2$ sublevels are of the most importance for the present study and are in good agreement with those of Zhang and Sampson [33]. For the methods used for the atomic rate calculations the reader may consult Ref. 20 and references therein.

The profile of the Al He- α line is assumed to be described by the Voigt function with the broadening parameter obtained by summing the rates out of the upper and lower levels. This line is one of the last transitions in the heliumlike manifold to be affected by Stark broadening as density increases. Detailed calculations of the Stark profile of He- α have been presented in Ref. 34, for neon and argon, for typical temperatures at which these ions exist. For neon ($Z=10$), the Stark profile is less than 10% of the Doppler width for electron densities $\leq 10^{22} \text{ cm}^{-3}$. In the case of argon ($Z=18$), electron density of at least 2×10^{23} is needed for the Stark width to exceed 10% of the Doppler width. According to Ref. 35, the Stark width in eV scales as $N_e^{2/3} Z^{-1}$. The temperature at which the heliumlike stage exists is approximately proportional to Z^3 [33], the ionic mass scales as Z , and line energy as Z^2 , leading to a line Doppler width scaling of Z^3 . Therefore,

the electron density at which the line Stark-to-Doppler width ratio is a constant 0.1 would scale as Z^6 . The detailed calculations quoted above are in reasonable accord with this approximation at $Z^{5.1}$. It is concluded that for aluminum, the Stark width of the He- α line would not exceed 10% of the Doppler width except for electron densities $\geq 4 \times 10^{22} \text{ cm}^{-3}$. At such densities, the collisional quenching parameter exceeds 0.5, and the line photons can no longer undergo multiple scattering. Therefore, for present purposes, the Voigt profile approximation is reasonable.

Results of the detailed configuration multilevel calculations for aluminum are shown in Figs. 4-7. In Figs. 4-6, the total ion density is assumed to be 3.0×10^{19} , 9.1×10^{19} , and $9.1 \times 10^{20} \text{ cm}^{-3}$, respectively. A calculation at solid density ($6 \times 10^{22} \text{ cm}^{-3}$) was also done and is discussed below. The plasma thickness is $100 \mu\text{m}$ in Figs. 4 and 5, but $10 \mu\text{m}$ in Fig. 6. In each case the plasma temperature is 200 eV, but there is no reason to expect qualitative differences for any temperature at which the heliumlike stage dominates (i.e., 150-400 eV for Al). As is evident from the "t=0" curves in these figures, the initial conditions are essentially the same as for the two-level-atom case. Initially, the innermost 10% of the planar plasma has the $1s2p^1P_1$ level excited to a fractional population of 0.01. The spread of excitation due to the diffusion of the He- α line photons is apparent. Modification of the escape probability due to the Doppler shift of plasma bulk motion was not taken into account; such effects are discussed in the next subsection.

As the electron density increases in Figs. 4-6, the collisional quenching probability per scattering ϵ increases from 0.01 (Fig. 4) to 0.029 (Fig. 5) to 0.23 (Fig. 6). The single flight photon escape probabilities P_e for these three cases are 1.6×10^{-2} , 8.9×10^{-3} , and 1.5×10^{-2} , respectively. Even though the column density of plasma represented in Figs. 5 and 6 is the same, the escape probability increases at the higher density due to the enhancement of the optically thin line wings in the assumed Voigt profile. However, the ultimate escape probability P_u that a photon leaves the plasma after one or multiple scatterings, drops monotonically with increasing density because of the dominant influence of collisional quenching. The expression given in Sec. II B yields $P_u = 0.61$, 0.23, and 0.05 for the conditions of Figs. 4-6, respectively. The differing collisional destruction of the He- α photons is clearly evident in Figs. 4-6. The spatial spread of excitation with time is much more pronounced in the lower density cases of Figs. 4 and 5, whereas at the ion density of $9.1 \times 10^{20} \text{ cm}^{-3}$ represented by Fig. 6, it is very difficult for a typical He- α photon to run the gauntlet of collisional destruction and reach the plasma boundary. The

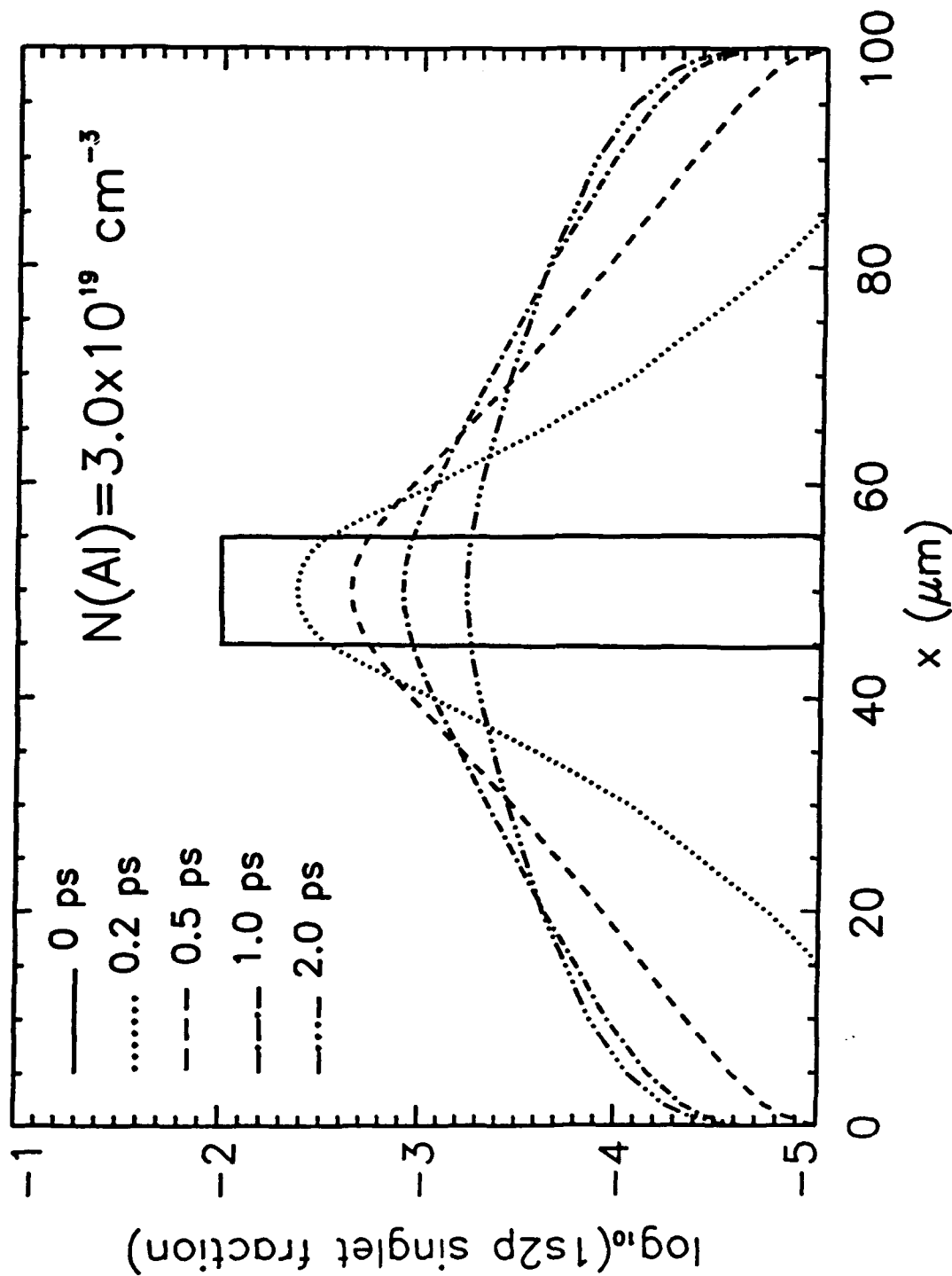


FIG. 4. Al XII $1s2p^1P_1$ population fraction is shown as a function of space and time as obtained from a multilevel fully time-dependent coupled rate and radiative transfer calculation as described in the text. The planar, $100 \mu\text{m}$ thick plasma has an assumed temperature of 200 eV and total ion density of $3.0 \times 10^{19} \text{ cm}^{-3}$.

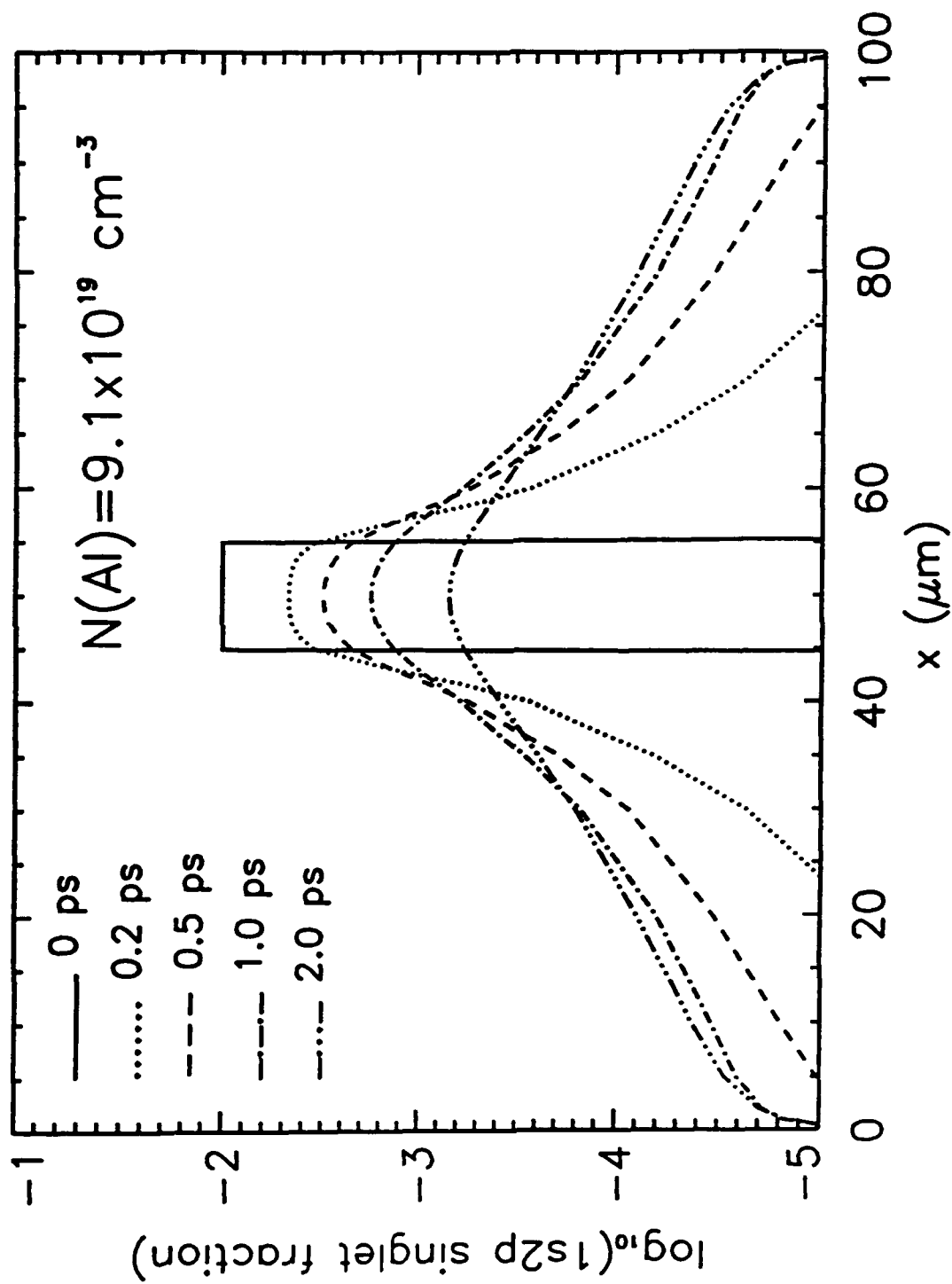


FIG. 5. As in Fig. 4, except that the total ion density is $9.1 \times 10^{19} \text{ cm}^{-3}$, yielding an electron density of 10^{21} cm^{-3} .

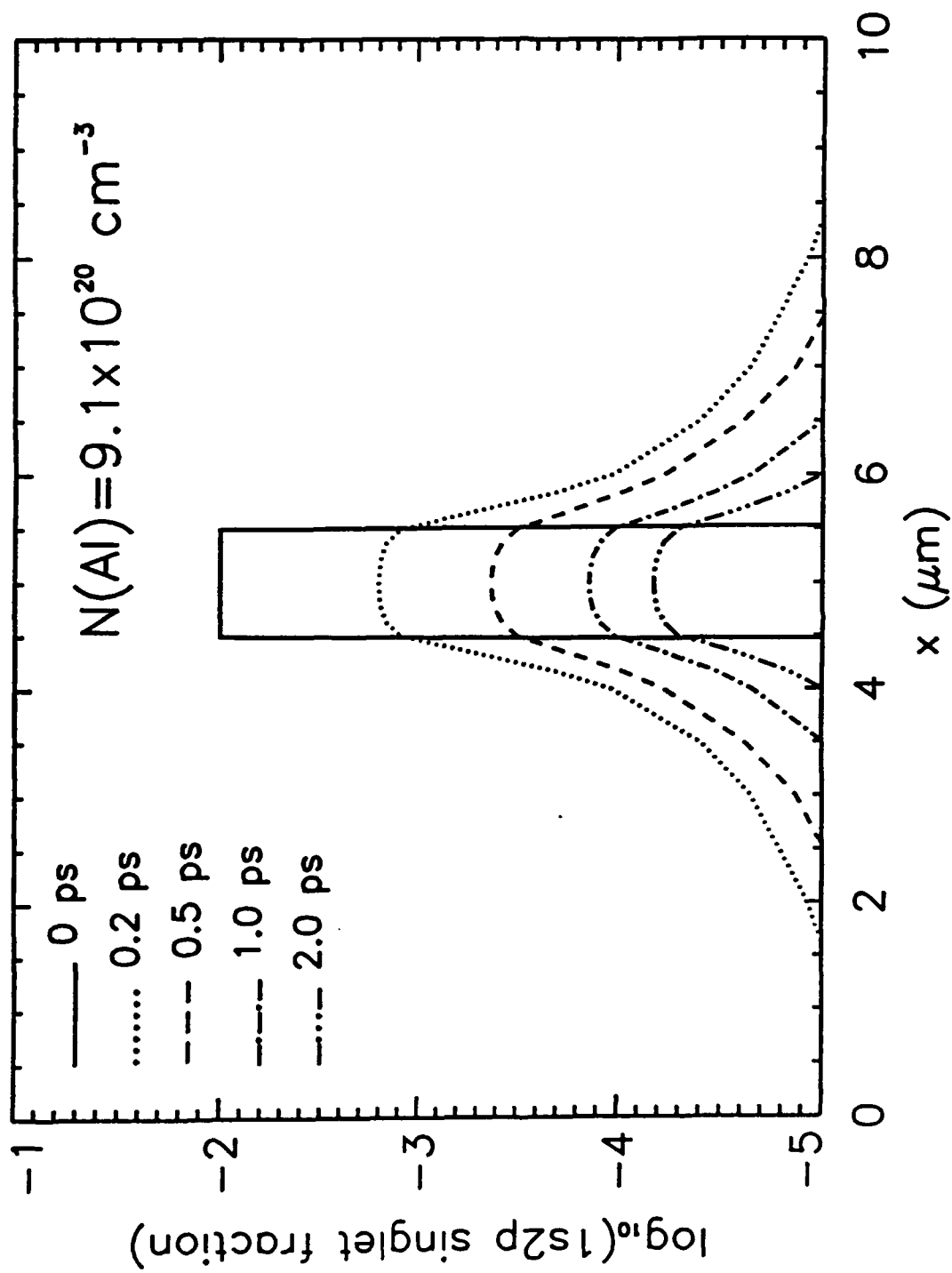


FIG. 6. As in Figs. 4 and 5, except that the total ion density is $9.1 \times 10^{20} \text{ cm}^{-3}$, and the plasma thickness is $10 \mu\text{m}$.

conditions of Fig. 5 are nearly identical to those for which the parameterized two-level-atom case (Figs. 1-3) was studied in the preceding section. The excitation profiles as a function of time for the multilevel and two-level-atom cases may be compared in Figs. 1 and 5 at 0.5 and 2.0 ps. They show very good qualitative agreement; exact correspondence is not expected since quenching of the line is affected by multilevel kinetics.

Fig. 7 quantifies the time dependence of the escape of the He- α line radiation for these three cases as calculated with the detailed multilevel model. At $t=5$ ps, nearly all the photons have escaped and the values of each of the curves of Fig. 7 may be taken as a good estimate of P_u . They indicate that the analytic model predictions quoted above are quite respectable estimates: 0.61, 0.23, and 0.05 vs. the computed values of 0.64, 0.27, and 0.07. Of course, the exact escape time is partly a matter of definition, but half the photons which ultimately will escape have escaped within ~ 0.3 ps for the highest density case, ~ 1.6 ps for the medium density of $9.1 \times 10^{19} \text{ cm}^{-3}$, and within ~ 1.8 ps at the lowest density considered. At high density, the photons are quenched if they do not escape the plasma on first flight or after a few scatterings, hence the short pulsewidth. At the solid ion density of $6.0 \times 10^{22} \text{ cm}^{-3}$, the quenching probability for Al is 0.95, and a detailed calculation confirmed the obvious expectation that the photon either escapes after initial collisional excitation of the $1s2p^1P_1$ level, or is destroyed. No spatial diffusion occurs in this situation and no lower limit on the pulsewidth is set by these effects. The higher level resonance lines of the heliumlike ion are of little significance for the present considerations. They are nearly always much weaker spectroscopically than the principal $n=2$ resonance line. Also, the higher lines are much more susceptible to collisional quenching because the radiative decay rates are lower and the collisional rates from the upper levels are much higher than those of He- α .

C. Generalized plasma conditions

1. Effect of bulk motion

It is well known that the frequency Doppler shift of the line profile due to expansion or compression of a medium can significantly enhance the escape probability. For planar geometry (to which the present work is confined), P_e may be calculated according to the method of Sobolev [28] when the velocity gradient is constant. Ref. 29 extends Sobolev's work to cylindrical media.

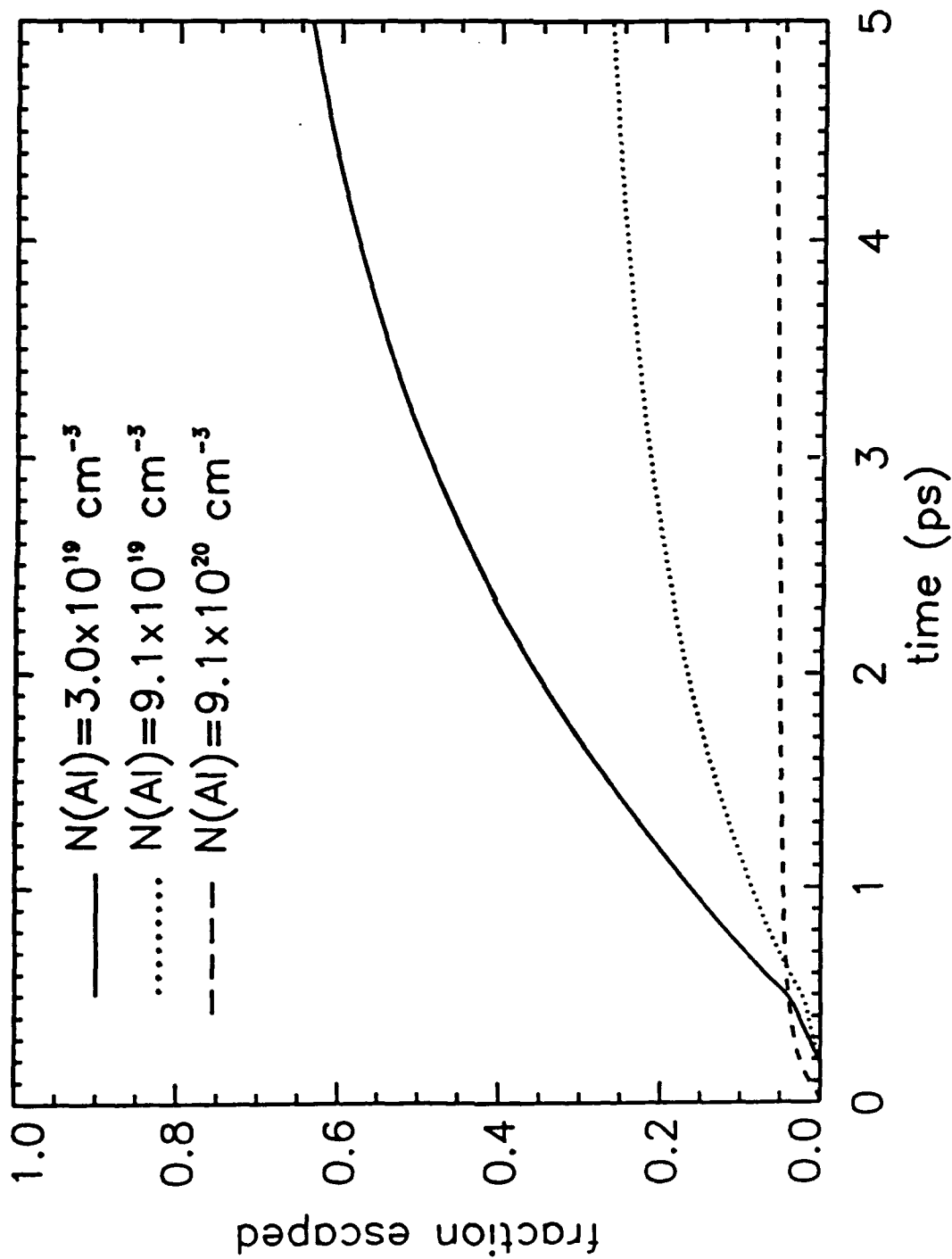


FIG. 7. Escaped photon fraction is plotted as a function of time for the Al He- α line. Total Al ion densities and other plasma conditions are as assumed in Figs. 4-6.

The frequent occurrence of regions of nearly constant velocity gradient in numerical and analytic solutions of plasma hydrodynamic behavior has fostered widespread use of these methods to obtain line escape probabilities. A full numerical treatment would require solution of the radiative transfer equation in the comoving frame. However, the analytic model embodied in eqs (5) and (6) needs no modification, only the substitution of the Sobolev escape probability for the static one. The effect of motional Doppler shifts may already have been detected in the observed broadening of heliumlike Al lines [36].

The magnitude of the effect may be estimated using the analytic solution for isothermal plasma expansion discussed in Ref. 37. The ion acoustic velocity for Al is $\sim 10^7$ cm sec $^{-1}$ at 200 eV. A 1 nsec prepulse would allow plasma expansion to ~ 100 μ m, implying a velocity gradient of 10^9 sec $^{-1}$. Two examples of 100 μ m planar Al plasmas were discussed above in the static limit. For the low density case of 3.0×10^{19} ions cm $^{-3}$, the motionally induced escape probability, calculated from eq. (40) of Ref. 28, is 8.0×10^{-3} , compared to 1.6×10^{-2} for the static limit. At the higher density of 9.1×10^{19} cm $^{-3}$, the Sobolev escape probability is 2.6×10^{-3} , as opposed to the static value of 8.9×10^{-3} . At this assumed velocity gradient, therefore, the escape probability is at most only slightly enhanced by motion and little effect is anticipated.

However, higher velocity gradients than 10^9 sec $^{-1}$ are anticipated in some instances, especially for kilovolt temperature plasmas, as seen in the simulations of Ref. 36 where values of 2×10^{10} sec $^{-1}$ are calculated within 1 psec of the main pulse. Applying this much higher velocity gradient to the two plasmas discussed above increases P_e to 0.16 and 0.053, at densities of 3.0 and 9.1×10^{19} cm $^{-3}$, respectively. According to eq. (10), the time for half of the He- α photons to escape would be reduced by factors of 5 and 2 for the two cases, respectively. It is therefore possible that motional broadening effects may significantly shorten the pulsewidth of a strong x-ray line, depending on the details of the particular plasma's hydrodynamics.

2. Atomic number scaling

The potential for broadening of the pulsewidth of a line is greatest when both the escape and quenching probabilities are small, allowing many scatterings within the plasma. In this limit, according to eq. (10), the escape time scales as

$$t_e \sim [A_{ul}(P_e + \epsilon)]^{-1} \quad (11)$$

Given current experimental capabilities, the atomic number region $8 \leq Z \leq 20$ is of most interest for production of significant K shell emission. The spontaneous decay rate for He- α has been calculated and tabulated as a function of Z in Ref. 1; the relevant collisional rate coefficients for the $n=2$ levels may be found in Ref. 33. The Einstein coefficient A_{ul} scales approximately as $Z^{4.2}$; the collisional rate coefficients as $Z^{-3.2}$, leading to a very sharp dependence: $\epsilon \sim Z^{-7.4}$. The collisional quenching probability for Si He- α , for instance, is only about half that for an identical Al plasma, with a difference of only one atomic number. The scaling of escape probability P_e is considerably weaker. According to eq. (11), the faster decay rate for higher atomic number elements partially compensates the much lower collisional quenching, but (neglecting the weak scaling of P_e), the escape time can increase with atomic number as fast as $Z^{3.2}$. Stated another way, plasma density must be increased along with atomic number to maintain the ratio of collisional to radiative processes and thereby prevent additional broadening of the line photon emission pulse.

IV. CONCLUDING REMARKS

In plasmas containing mostly K shell ionization stages, the strongest resonance line (He- α) is usually a significant if not dominant component of the x-ray emission. This is true of plasmas lasting several nsec, such as the dense Z pinch, as well as of plasmas produced by ultrashort pulse lasers which may persist for psec timescales or shorter. Photons emitted in this line as well as other strong resonance lines can be subject to many absorptions and re-emissions in optically thick plasmas. In general this time-broadens the line component of the x-rays.

This paper has presented detailed numerical calculations supplemented and interpreted by an analytic model which demonstrate that for laboratory plasmas of moderate density and mm or smaller size, the escape time is a few psec or less. These models could also be employed in analyzing astrophysical scale plasmas where much longer characteristic times are expected. One current goal of experiments employing high power subpicosecond lasers is to produce the shortest possible x-ray pulse. If the entire laser-produced plasma is of solid density, collisional quenching of the line photons assures that the scattering mechanism plays no role in widening the x-ray pulse. However, to date the most efficient x-ray generation has occurred when a preformed plasma created by a laser prepulse is subsequently irradiated by the main high intensity pulse. The persistence of the heliumlike ground state raises the possibility that a photon-scattering surrounding plasma,

even though much cooler than the principal x-ray generating region, may place a lower limit on the width of the x-ray pulse. Perhaps the use of mostly continuum emission or lines of other ionization stages which may be more subject to collisional quenching would ameliorate this effect. The enhancement of the line escape probability due to the motional Doppler shift may further reduce its importance in some instances. The time-dependent transfer of radiation in strong resonance lines is one of several physical processes which determine the shape and intensity of the x-ray emission from the new class of ultrashort lived laser-produced plasmas.

REFERENCES

1. C. D. Lin, W. R. Johnson, and A. Dalgarno, *Phys. Rev. A* **15**, 154 (1977).
2. M. M. Murnane, H. C. Kapteyn, M. D. Rosen, and R. W. Falcone, *Science* **251**, 531 (1991).
3. C. H. Nam, W. Tighe, S. Suckewer, J. F. Seely, U. Feldman, and L. A. Woltz, *Phys. Rev. Lett.* **59**, 2427 (1987).
4. M. M. Murnane, H. C. Kapteyn, and R. W. Falcone, *Phys. Rev. Lett.* **62**, 155 (1989).
5. J. A. Cobble et al., *Phys. Rev. A* **39**, 454 (1989).
6. J. C. Kieffer et al., *Phys. Rev. Lett.* **62**, 760 (1989).
7. J. A. Cobble, G. T. Schappert, L. A. Jones, A. J. Taylor, G. A. Kyrala, and R. D. Fulton, *J. Appl. Phys.* **69**, 3369 (1991).
8. A. Zigler et al., *Appl. Phys. Lett.* **59**, 534 (1991).
9. A. Zigler et al., *Opt. Lett.* **16**, 1261 (1991).
10. U. Teubner, G. Kuhnle, and F. P. Schafer, *Appl. Phys. Lett.* **59**, 2672 (1991).
11. W. M. Wood, C. W. Siders, and M. C. Downer, *Phys. Rev. Lett.* **67**, 3523 (1991).
12. M. M. Murnane, H. C. Kapteyn, and R. W. Falcone, *Phys. Fluids B* **3**, 2409 (1991).
13. S. E. Harris and J. E. Kmetec, *Phys. Rev. Lett.* **61**, 62 (1988).
14. M. D. Rosen, *Scaling Laws for Femtosecond Laser Plasma Interactions*, in *SPIE Conf. Proc.* **1229**, E. M. Campbell, ed., p. 160 (1990).
15. V. V. Kolchin and S. A. Shlenov, *Sov. J. Quantum Electron.* **21**, 247 (1991).
16. H. M. Milchberg, I. Lyubomirsky, and C. G. Durfee, III, *Phys. Rev. Lett.* **67**, 2654 (1991).
17. G. A. Kyrala, R. D. Fulton, E. K. Wahlin, L. A. Jones, G. T. Schappert, J. A. Cobble, and A. J.

Taylor, Appl. Phys. Lett. 60, 2195 (1992).

18. J. Cooper and P. Zoller, Astrophys. J. 277, 813 (1984).

19. S. Chandrasekhar, Radiative Transfer, (Dover, New York, 1960), pp. 61-62.

20. D. Duston and J. Davis, Phys. Rev. A 23, 2602 (1981).

21. T. R. Young and J. P. Boris, J. Phys. Chem. 81, 2424 (1977).

22. P. B. Kunasz and D. G. Hummer, Mon. Not. R. Astron. Soc. 166, 19 (1974).

23. T. Holstein, Phys. Rev. 72, 1212 (1947).

24. J. P. Apruzese, J. Davis, D. Duston, and K. G. Whitney, J. Quant. Spectrosc. Radiat. Transfer 23, 479 (1980).

25. J. P. Apruzese, J. Quant. Spectrosc. Radiat. Transfer 34, 447 (1985).

26. J. C. Weisheit, J. Quant. Spectrosc. Radiat. Transfer 22, 585 (1979).

27. R. C. Mancini, R. F. Joyce, and C. F. Hooper, Jr., J. Phys. B 20, 2975 (1987).

28. V. V. Sobolev, Sov. Astron. 1, 678 (1957).

29. A. I. Shestakov and D. C. Eder, J. Quant. Spectrosc. Radiat. Transfer 42, 483 (1989).

30. D. Mihalas, Stellar Atmospheres, 2nd ed. (Freeman, San Francisco, 1978) , p. 378.

31. D. E. Osterbrock, Astrophys. J. 135, 195 (1962).

32. G. B. Rybicki and D. G. Hummer, Mon. Not. R. Astron. Soc. 144, 313 (1965).

33. H. Zhang and D. H. Sampson, Astrophys. J. Suppl. Ser. 63, 487 (1987).

34. P. C. Kepple and J. E. Rogerson, Naval Research Laboratory Memorandum Report No. 4216 ,1980 (unpublished).

35. H. R. Griem, M. Blaha, and P. C. Kepple, Phys. Rev. A 19, 2421 (1979).

36. G. T. Schappert et al., "Atomic Processes in Plasmas Under Ultra-Intense Laser Irradiation", in **AIP Conference Proceedings 206: Atomic Processes in Plasmas**, edited by Y. K. Kim and R. C. Elton (American Institute of Physics, New York, 1990), p. 217.
37. X. Liu and D. Umstadter, *Phys. Rev. Lett.* **69**, 1935 (1992).

**The Influence of Non-Maxwellian Distributions on the Gain
of 3s-3p Transitions in Neon-like Selenium**

K. G. Whitney, P. E. Pulsifer, and A. DasGupta

Radiation Hydrodynamics Branch

Plasma Physics Division

Abstract

If, through stimulated Brillouin scattering or through parametric laser absorption near the critical surface, a significant amount of ion-acoustic microturbulence is generated in laser-produced plasmas, then a 10- to 100-fold reduction in the intensity threshold for generating non-Maxwellian distributions of the kind described by Langdon (A. B. Langdon, Phys. Rev. Lett. 44, 575 (1980)) could occur. Because these distributions have depleted tails, they would alter the ionization dynamics of these plasmas and significantly affect the interpretation of x-ray laser experiments, in particular. In this paper, we will discuss the potential effects of laser-produced non-Maxwellians on the gain dynamics of selenium neon-like x-ray lasers. We utilize an atomic model with a full set of $n=3$ neon-like multiplet states, and compare non-Maxwellian $J=0-1$ and $J=2-1$ gain calculations to corresponding Maxwellian calculations. It is found that the generation of a strong ion-acoustic turbulence at laser intensities in excess of 10^{15} W/cm² could, in principle, help to promote increases in the gain of the $3s-3p$ transitions in neon-like selenium and to promote significant improvements in the performance of these lasers.

I Introduction

In laser-produced plasmas, there are many problems associated with the absorption of laser light in the plasma. In this case, the absorption of electromagnetic energy by inverse Bremsstrahlung can be strongly perturbed by the competing processes of stimulated Raman or stimulated Brillouin scattering. These scatterings can generate a strong microturbulence through the nonlinear generation of plasma waves and ion-acoustic waves.¹ When laser absorption occurs at the critical surface, moreover, parametric decay instabilities are excited that generate a strong Langmuir turbulence that decays into ion-acoustic turbulence. Strong temperature gradients generated by the absorption of laser light in sub-critical x-ray laser plasmas can initiate electrical currents of sufficient strength to generate ion-acoustic turbulence. Unfortunately, it is difficult to calculate the absorption coefficient of laser light in microturbulent plasmas unless the dynamical growth and saturation of the microturbulence energy spectrum can be calculated throughout the plasma.

Microturbulence also affects the heat transport and viscosity properties of a collisional plasma as well as the shape of the isotropic electron distribution function.^{2,3} These microturbulence properties will manifest themselves in a variety of ways in laser-produced plasmas, and the full combination of their effects should be used to diagnose the presence of microturbulence. Moreover, microturbulence may need to be factored into any analysis of laser-produced plasma dynamics before other effects such as nonlocal heat transport can be invoked⁴ to fully explain, for example, the inhibited heat flow known to be present in these plasmas.⁵

In this paper, we assume that a fully developed microturbulence has been generated in a laser-produced selenium plasma. Depending on the charge states of the plasma, the microturbulence will change the plasma's laser absorption as well as its transport properties. In this paper, we will calculate selenium's charge state in Collisional-Radiative Equilibrium (CRE) utilizing the atomic model described in Ref. (6) in order to illustrate the effect that the non-Maxwellian electron distributions generated by the laser absorption process can have on the neon-like gain coefficients. When ion-acoustic turbulence is generated as a result of the laser-plasma interaction, this microturbulences makes it easier to generate these non-Maxwellian distributions.

We begin by initially investigating the coupling of ion-acoustic turbulence to the electron kinetic equation. We then seek to determine the plasma conditions and ion-acoustic fluctuation

levels needed to significantly enhance a weakly turbulent selenium plasma's laser absorptivity given a CRE charge state of the plasma as a function of electron temperature and ion density. Microturbulence promotes the production of self-similar non-Maxwellian electron velocity distributions of the kind described by Dum² and Langdon,⁷ i.e., Langdon's criterion for non-Maxwellian production is modified by the presence of a fully developed microturbulence. The laser intensities that are needed to drive selenium into non-Maxwellian states are then determined from this criteria. These results may have special significance to x-ray laser research. Neon-like selenium is a well studied x-ray laser medium,⁸ and a number of discrepancies regarding its observed, versus its calculated, ionization behavior remain to be explained.⁹ Some of this discrepancy might be explained by the presence of microturbulence and its promotion of non-Maxwellian ionization behavior.

This paper is structured as follows. Section II contains a new derivation, more general than one presented by Dum,³ of the way ion-acoustic turbulence can be included in the kinetic theory of a collisional plasma. Separate contributions of this microturbulence to the different terms of the expansion of the distribution function in spherical harmonics are derived. These contributions are, to good approximation, identical in form to the ones made by electron-ion collisions. Thus, Langdon's criterion can easily be rederived for the laser intensity needed to drive the electrons into a non-Maxwellian state due to rapid heating in a microturbulent plasma.⁷ Using a phenomenological model for the fluctuation level scaling achievable in weakly turbulent plasmas,¹⁰ we then calculate the selenium plasma conditions under which microturbulence would be expected to produce non-Maxwellian electron distributions as a function of selenium plasma conditions. In section III, the effects of these non-Maxwellians on gain calculations in neon-like selenium is presented and discussed. Finally, some implications of this work for experimentally diagnosing plasma microturbulence and for improving the performance of neon-like selenium lasers are discussed in section IV.

II Microturbulence Analysis

We begin our analysis by writing the electron distribution function, f_e , as the sum of an average (in space and time), $\langle f \rangle$, and of a rapidly fluctuating distribution, δf : $f_e = \langle f \rangle + \delta f$.¹¹ We work in the coordinate system of the fluid flow, Fourier transforming the spatial coordinates from

\mathbf{x} to \mathbf{k} , and utilizing standard quasilinear theory to solve for δf by ignoring particle accelerations and plasma fluid flow:¹¹

$$\delta f(\mathbf{k}, \mathbf{v}) = \frac{ie}{m} \frac{\delta \mathbf{E}(\mathbf{k})}{\omega(\mathbf{k}) - \mathbf{k} \cdot \mathbf{v} + i\gamma(\mathbf{k})} \cdot \nabla_{\mathbf{v}} \langle f \rangle, \quad (1)$$

where e is the electronic charge, a positive number, and m is the electron mass. The time dependence of the electromagnetic fluctuations is given by $\exp[i(\omega(\mathbf{k}) + i\gamma(\mathbf{k}))t]$. This expression for δf must be substituted into the equation for $\langle f \rangle$, which contains a collision term, $C(\langle f \rangle)$, that is the sum of electron-electron, electron-ion, and electron-microturbulence interactions:

$$C = C^{ee} + C^{ei} + C^{AN}, \quad (2)$$

where

$$C^{AN} \equiv (\partial_t \langle f \rangle)_{AN} = \frac{e}{m} \langle \delta \mathbf{E}(\mathbf{r}, t) \cdot \nabla_{\mathbf{v}} \delta f(\mathbf{r}, \mathbf{v}, t) \rangle. \quad (3)$$

Note, because we have specialized to ion-acoustic microturbulence, the more general notation C^{AN} will be replaced by C^{ia} . When Eq. (1) is substituted into Eq. (3), a result that can be written in terms of a microturbulence diffusion tensor, \mathcal{D}_{ij} , is obtained:

$$C^{ia} = \frac{\partial}{\partial v_i} \left(\mathcal{D}_{ij} \frac{\partial \langle f \rangle}{\partial v_j} \right), \quad (4)$$

where

$$\mathcal{D}_{ij} = \frac{8\pi e^2}{m^2} \int d^3k \mathcal{W}(\mathbf{k}) \hat{k}_i \hat{k}_j \frac{\gamma(\mathbf{k})}{(\omega(\mathbf{k}) - \mathbf{k} \cdot \mathbf{v})^2 + \gamma(\mathbf{k})^2} \quad (5)$$

$$= \mathcal{D}_0(v^2) \delta_{ij} + \mathcal{D}_1(v^2) \frac{v_i v_j}{v^2}. \quad (6)$$

$\mathcal{W}(\mathbf{k})$ is the energy spectrum of the ion-acoustic fluctuations, i.e., $\langle |\delta \mathbf{E}(\mathbf{r}, t)|^2 / 8\pi \rangle = \int d^3k \mathcal{W}(\mathbf{k})$, and $\hat{k}_i \equiv k_i/k$. We are interested in evaluating \mathcal{D}_{ij} for those physical situations in which the turbulence is fully developed and the plasma is marginally stable.¹² In these situations, the limit $\gamma \rightarrow 0$ can be taken so that $\gamma/((\omega - \mathbf{k} \cdot \mathbf{v})^2 + \gamma^2) \rightarrow \pi \delta(\omega - \mathbf{k} \cdot \mathbf{v})$. We further simplify the problem by assuming that the microturbulence is isotropic. (The more complete theory of non-isotropic microturbulence is reviewed by Bychenkov, Silin, and Uryupin.¹³)

The dispersion relation for ion-acoustic waves is $\omega(\mathbf{k}) = \pm \sqrt{k^2 c_s^2 / (1 + k^2 \lambda_D^2)} \cong \pm k c_s$, where $c_s \cong \sqrt{Z k_B T_e / m_i}$ is the ion sound speed, and $\lambda_D = v_{th} / (\sqrt{2} \omega_e)$ is the electron Debye

length. $v_{th} \equiv \sqrt{2k_B T_e/m}$ is the average electron thermal velocity, $\omega_e \equiv \sqrt{4\pi n_e e^2/m}$ is the electron plasma frequency, \bar{Z} is the average charge state of an ion, and m_i is the ion mass. The diffusion tensor can now be evaluated by letting the spherical coordinate unit vectors, \hat{u}_θ , \hat{u}_ϕ , and \hat{u}_v , in velocity space define the directions, \hat{k}_x , \hat{k}_y , and \hat{k}_z , in k-space respectively. The k-space integration in Eq. (5) can be carried out in the spherical k-space coordinates, (k, θ', ϕ') , where $\mathbf{k} \cdot \mathbf{v} = kv \cos \theta' \equiv kv\mu$. Using the reality condition, $\omega(-k) = -\omega(k)$, we rewrite Eq. (5) as

$$\mathcal{D}_{ij} = \frac{8\pi^2 e^2}{m^2} \int_0^\infty k^2 dk \mathcal{W}(k) \int_0^{2\pi} d\phi' \left\{ \int_{-1}^0 d\mu \hat{k}_i \hat{k}_j \delta(kv\mu + \omega(k)) + \int_0^1 d\mu \hat{k}_i \hat{k}_j \delta(kv\mu - \omega(k)) \right\}, \quad (7)$$

where $\omega(k) = kc_s$ for ion-acoustic waves. The integrations produce the following diagonal diadic form:

$$\mathcal{D} = \mathcal{D}_0(\hat{u}_\theta \hat{u}_\theta + \hat{u}_\phi \hat{u}_\phi) + (\mathcal{D}_0 + \mathcal{D}_1)\hat{u}_v \hat{u}_v. \quad (8)$$

For ion-acoustic turbulence,

$$\mathcal{D}_0 = \frac{4\pi^2 e^2 \Omega_1}{m^2 v} \left\{ 1 - \frac{c_s^2}{v^2} \right\} \eta_+(v - c_s), \quad (9)$$

$$\mathcal{D}_1 = -\frac{4\pi^2 e^2 \Omega_1}{m^2 v} \left\{ 1 - \frac{3c_s^2}{v^2} \right\} \eta_+(v - c_s). \quad (10)$$

In these expressions,

$$\Omega_1 \equiv 4\pi \int_0^\infty dk k^n \mathcal{W}(k), \quad (11)$$

$\eta_+(x)$ is the Heaviside function, which equals one when $x > 0$ and is zero otherwise. The spectrum integration, Ω_1 defines the strength of the ion-acoustic microturbulence. Note that ion-acoustic turbulence affects essentially the entire distribution function, because $c_s \ll v_{th}$, and one can take

$$\mathcal{D}_0 \cong -\mathcal{D}_1 \cong \frac{4\pi^2 e^2 \Omega_1}{m^2 v} \quad (12)$$

to good approximation in order to describe these interactions.

We next make the usual approximate expansion of $\langle f \rangle$ in spherical harmonics¹⁴ in the coordinate system moving with the fluid velocity, \mathbf{v}_f :

$$\langle f \rangle \cong f_0 + \mathbf{f}_1 \cdot \frac{\mathbf{v}}{v}. \quad (13)$$

The collision terms are similarly expanded: $C \cong C_0 + C_1 \cdot \mathbf{v}/v$. The equations of motion for f_0 and \mathbf{f}_1 are then (see Ref. (15), pages 114,115)

$$(\partial_t + \mathbf{v}_f \cdot \nabla) f_0 - (\nabla \cdot \mathbf{v}_f) \frac{v}{3} \frac{\partial f_0}{\partial v} + \frac{v}{3} \nabla \cdot \mathbf{f}_1 + \frac{1}{3v^2} \frac{\partial}{\partial v} (v^2 \mathbf{a}' \cdot \mathbf{f}_1) = C_0(f_0) \quad (14)$$

and

$$(\partial_t + \mathbf{v}_f \cdot \nabla) \mathbf{f}_1 - (\nabla \mathbf{v}_f) \cdot \mathbf{f}_1 - (\nabla \mathbf{v}_f + (\nabla \mathbf{v}_f)^T + \mathbf{I}_2 \nabla \cdot \mathbf{v}_f) \cdot \frac{v^2}{5} \frac{\partial}{\partial v} \left(\frac{\mathbf{f}_1}{v} \right) - \omega_c \times \mathbf{f}_1 - C_1(\mathbf{f}_1) = -v \nabla f_0 - \mathbf{a}' \frac{\partial f_0}{\partial v}, \quad (15)$$

where

$$\mathbf{a}' \cong -\frac{e}{m} \left(\mathbf{E} + \frac{\mathbf{v}_f}{c} \times \mathbf{B} \right) \equiv -\frac{e}{m} \mathbf{E}'. \quad (16)$$

\mathbf{E}' is the effective electric field seen in the local frame of the moving fluid, and $\omega_c \equiv e\mathbf{B}/mc$. Both C_0 and C_1 contain contributions from C^{ia} , which we denote C_0^{ia} and C_1^{ia} respectively. From Eqs. (4) and (6), one finds that

$$C_0^{ia} = \frac{1}{v^2} \partial_v (v^2 (\mathcal{D}_0 + \mathcal{D}_1) \partial_v f_0) \quad (17)$$

and

$$C_1^{ia} = \frac{1}{v^2} \partial_v (v^2 (\mathcal{D}_0 + \mathcal{D}_1) \partial_v \mathbf{f}_1) - \frac{2}{v^2} \mathcal{D}_0 \mathbf{f}_1. \quad (18)$$

(Similarly, by going one more term in the spherical harmonic expansion, one obtains $C_2^{ia} = v^{-2} \partial_v [v^2 (\mathcal{D}_0 + \mathcal{D}_1) \partial_v \mathbf{f}_2] - 6v^{-2} \mathcal{D}_0 \mathbf{f}_2$.)

Eq. (12) implies that $C_0^{ia} \cong 0$ and

$$C_1^{ia} \cong -\frac{2}{v^2} \mathcal{D}_0 \mathbf{f}_1 \quad (19)$$

$$\equiv -\nu^{ia} \left(\frac{v_{th}}{v} \right)^3 \mathbf{f}_1, \quad (20)$$

where the effective velocity-independent ion-acoustic collision frequency, ν^{ia} , is

$$\nu^{ia} = \frac{8\pi^2 e^2 \Omega_1}{m^2 v_{th}^3}. \quad (21)$$

Thus, like electron-ion scattering, the interaction of electrons with ion-acoustic waves primarily affects the momentum transfer to or from the electrons.

We next adopt the common procedure of ignoring electron-ion collisions in Eq. (14) ($C_0^{ei} \cong 0$) and electron-electron collisions in Eq. (15) ($C_1^{ee} \cong 0$). The isotropic electron-electron collision term, C_0^{ee} , is given by the Fokker-Planck expression.¹⁵ If the ions are Maxwellian, the electron-ion momentum transfer in the ion rest frame has the same form as the electron/ion-acoustic term:¹⁵

$$C_1^{ei} = -\nu_{ei} \left(\frac{v_{th}}{v} \right)^3 f_1, \quad (22)$$

where the velocity-independent electron-ion collision frequency is defined by

$$\nu_{ei} \equiv \frac{4\pi n_e \bar{Z} e^4 \log \Lambda_e}{m^2 v_{th}^3}, \quad (23)$$

and $\log \Lambda_e$ is the Coulomb logarithm. Thus,

$$C_0 \cong C_0^{ee} \quad (24)$$

and

$$C_1 \cong C_1^{ei} + C_1^{ia} \equiv -\nu_1 \left(\frac{v_{th}}{v} \right)^3 f_1, \quad (25)$$

where

$$\nu_1 = \nu_{ei} + \nu^{ia} \equiv (1 + \beta)\nu_{ei}. \quad (26)$$

A similar expression for C_1 was derived by Dum,³ who carried out a direct angle averaging of Eq. (5).

The effect of current and heat flow on the shape of the isotropic distribution function, f_0 , is determined by the two f_1 terms in Eq. (14). The first term, involving $\nabla \cdot f_1$, determines the effects of current and heat flow on the electron number and energy densities respectively. The second term, involving a' , represents the effect of laser heating on the electrons. To determine f_1 , we look for a solution to Eq. (15). Generally, as a first approximation, the gradient and time derivative terms can be dropped, leaving one with the equation,

$$-\omega_c \times f_1 + (1 + \beta)\nu_{ei} \left(\frac{v_{th}}{v} \right)^3 f_1 = -v \nabla f_0 - a' \frac{\partial f_0}{\partial v}. \quad (27)$$

This equation may be easily solved for f_1 in terms of $f_0(v)$. If a Maxwellian distribution is used for f_0 , simple expressions can then be found for the electric current, j_e , and heat flux, q_e , from

which the thermal conductivity, κ_e , can be obtained. Both conductivities will be reduced from their classical, non-turbulent values by the factor, $1 + \beta$.

To determine the size and the dynamics of these conductivity reductions in detail, one has the difficult task of calculating the turbulence spectrum, \mathcal{W} . However, since only one moment, Ω_1 , of \mathcal{W} is needed to determine the size of β for ion-acoustic turbulence, it is possible to estimate how strongly a given level of electrostatic microturbulence will affect these conductivities by establishing a bound on Ω_1 . We begin with the definition of β . From Eqs. (21) and (26),

$$\beta = \frac{3\pi}{2} \left(\frac{\omega_e}{v_{th}} \right) \left(\frac{\Omega_1}{E_{th}} \right) \frac{\omega_e}{\nu_{ei}}, \quad (28)$$

where E_{th} is the electron thermal energy density:

$$E_{th} = (3/2)n_e k_B T_e. \quad (29)$$

The size of Ω_1 can be estimated by factoring an average ion-acoustic wavelength, $1/\langle k \rangle$, from its integrand; then, $\Omega_1 = f_E E_{th} / \langle k \rangle$, where f_E is the ratio of the electrostatic fluctuation energy to the thermal energy, $(\langle |\delta E(r, t)|^2 / 8\pi \rangle / E_{th})$. Thus,

$$\beta = \frac{3\pi}{2} \left(\frac{\omega_e / \langle k \rangle}{v_{th}} \right) \left(\frac{\omega_e}{\nu_{ei}} \right) f_E. \quad (30)$$

If, by virtue of the ion-acoustic dispersion relation, one assumes that $\langle k \rangle \leq 1/\lambda_D$, then

$$\beta \geq \beta_{min} \equiv \sqrt{2\pi} \omega_e \tau_e f_E. \quad (31)$$

For laser-produced plasmas, the product, $\omega_e \tau_e$, can range in value from > 1 to $> 10^4$; thus, for large values of this ratio, ion-acoustic energy fluctuation levels, f_E , of 1% can easily lead to a turbulence contribution to the thermal conductivity that is 10 times larger than that due to two-particle collisions. This turbulence level corresponds to a heat flux limiter of 0.1, a value often used to describe the dynamics of laser-produced plasmas.⁵

Investigating the non-turbulent laser heating of electrons, Langdon⁷ derived a criterion that predicted the intensity at which inverse Bremsstrahlung heating would dominate over electron-electron collisions. He found that, when this criterion was satisfied, the electron distribution approached a self-similar form whose high energy tail was depleted relative to that of a Maxwellian

distribution. Earlier, Dum² had found that, under strong ion-acoustic turbulence, the electron distribution tends towards the same self-similar form as discussed by Langdon. We rederive this criterion for a microturbulent plasma.

By substituting the general solution to Eq. (27) into Eq. (14) and by ignoring the $v \nabla f_0$ term in Eq. (27) and the gradient terms in Eq. (14), one obtains the equation, $\partial_t f_0 = H(f_0) + C_0(f_0)$, which is the equation that was used by Langdon. The laser heating term has the form,

$$H(f_0) = \frac{4\pi e^2 I}{m^2 c} \frac{1}{3v^2} \frac{\partial}{\partial v} \left(v^2 \frac{\nu_1 (v_{th}/v)^3}{\omega^2 + \nu_1^2 (v_{th}/v)^6} \frac{\partial f_0}{\partial v} \right), \quad (32)$$

where I is the laser intensity and $\omega = c/\lambda$ is the laser frequency. One can define an e-folding time for laser heating, τ_H^{laser} , by:

$$\tau_H^{laser} \equiv \frac{E_{th}}{(\mathbf{j} \cdot \mathbf{E})_{laser}} = \frac{E_{th}}{\kappa_L I}, \quad (33)$$

where $\kappa_L I = 4\pi \int dv v^2 (m/2) v^2 H(f_0)$ and κ_L is the laser absorption coefficient. $H(f_0)$ dominates $C_0(f_0)$ when the laser e-folding time for heating is smaller than the equilibration collision time, τ_{ee} , needed to establish a Maxwellian distribution: $\tau_{ee}/\tau_H^{laser} \geq 1$. Since $\tau_{ee} = \bar{Z}\tau_e$, one can write this criterion as

$$\tau_{ee}/\tau_H^{laser} = \frac{2}{3}(1 + \beta)\bar{Z} \frac{v_0^2}{v_{th}^2} \geq 1, \quad (34)$$

where v_0 is the peak oscillation velocity of the electrons in the high frequency (laser) electric field. Alternatively, this criterion can be rewritten as a condition on the laser intensity:

$$I/I_{crit} = \frac{2}{3}(1 + \beta)\bar{Z} \frac{v_0^2}{v_{th}^2} \geq 1, \quad (35)$$

where, by definition of v_0 and v_{th} ,

$$I_{crit} \equiv \frac{3\pi m c^3 k_B T_e}{2\bar{Z} e^2 (1 + \beta) \lambda^2} \left[\frac{ergs}{sec - cm^2} \right]. \quad (36)$$

The reduction in I_{crit} by the factor, $(1 + \beta)$, corresponds to an increase in the laser absorption coefficient, κ_L , by the same amount.

The magnitudes of the microturbulence corrections to I_{crit} depend on plasma conditions and can be determined once the saturation level, f_E , is known. This level also depends on plasma conditions and on the strength of the energy source driving the turbulence. We investigate this

dependence by arbitrarily fixing the value of f_E for one set of plasma conditions and by scaling f_E as described by Ichimaru.¹⁰ In a weakly turbulent plasma, he argued that the turbulence spectrum scales as $g^{1/2}$, where g is the plasma parameter:

$$g \equiv \frac{1}{n_e \lambda_D^3}, \quad (37)$$

which we take to be the electron plasma parameter. Note that in strongly turbulent plasmas, f_E would scale as g^0 , i.e., it would be independent of g .¹⁰

To illustrate how this scaling affects β_{min} and I_{crit} , we calculate selenium's ionization state, \bar{Z} , using the atomic model described in Reference (6) by assuming that the plasma is in CRE. Although laser-produced selenium plasmas have been well studied recently in x-ray laser experiments,^{8,9} these plasmas are also of interest in z-pinch experiments. The \bar{Z} values for selenium that are needed to calculate the quantities, f_E , β_{min} , and I_{crit} , are displayed in Fig. (1) as a function of temperature and density. For the purpose of this numerical example, we took $f_E = 0.5g^{1/2}$. This formula produced the values for f_E that are shown in Fig. (2) for the same plasma temperatures and densities as Fig. (1). Fig. (2) is an illustration of the fact that, in weakly turbulent plasmas, as in quiescent plasmas, relatively higher levels of electrostatic energy fluctuations can be generated as the plasma temperature is lowered or as the plasma density is increased. These fluctuation levels produce the β_{min} enhancement factors (see Eq. (31)) shown in Fig. (3), which, in turn, produce the contours for I_{crit} that are presented in Figs. (4).

The I_{crit} values in Fig. (4) were calculated for frequency tripled neodymium ($\lambda = 0.35\mu m$) laser radiation. They are close to those used in current experiments; thus, as these experiments are scaled to higher photon energies or higher x-ray laser intensities, the likelihood for generating non-Maxwellian electron distributions under microturbulent plasma conditions may increase. Note that Fig. (2) can be scaled directly to calculate β_{min} in selenium for any f_E since β_{min} is directly proportional to f_E . In the gain calculations that follow, we will focus our attention on the point at $T_e = 1 \text{ keV}$ and $N_i = 10^{20} \text{ ions/cm}^3$ where we will assume that $\beta \cong 10$.

III Gain Calculations

When $I \gg I_{crit}$, the electron distribution approaches the self-similar form, $u^{-3} \exp(-v^5/5u^5)$, with $u^5 \sim t$, discussed by Dum² and Langdon.⁷ The number of electrons in the tail of this distribution is greatly reduced, leading to reductions in the rates at which the plasma

is ionized. Significant departures of f_0 from a Maxwellian distribution also change the calculation of f_1 , which, in turn, modifies the electrical and heat conductivities that are calculated due to plasma microturbulence alone (see Refs. (2) and (3)). For weaker intensities, the distribution function has transitional behavior of the kind calculated by Alaterre Matte, and Lamoureux.¹⁸ These authors found that for laser intensities comparable to I_{crit} , solutions to the Fokker-Planck equation, $\partial_t f_0 = H(f_0) + C_0(f_0)$, can be adequately approximated by the functions:

$$f_0^m(E, T_e) = (C_m/u_m^3) \exp(-(v^m/u_m^m)), \quad (38)$$

where

$$C_m = \frac{m}{4\pi\Gamma(3/m)}, \quad (39)$$

and

$$kT_e = \left(\frac{\Gamma(5/m)}{3\Gamma(3/m)} \right) m u_m^2. \quad (40)$$

When $m = 5$, these functions coincide with the self-similar solutions of Dum and Langdon. When $m = 2$, they coincide with Maxwellian distributions. Thus, for $2 < m < 5$, these functions describe transitional behavior between the Maxwellians, present when $I \ll I_{crit}$, and the self-similar distributions, present when $I \gg I_{crit}$. The differences between the functions, f_0^m , and a Maxwellian distribution are conveniently represented by the departure functions, γ , defined by

$$\gamma(E) \equiv \frac{f_0^m(E, T_e)}{f_0^{max}(E, T_e)} = \frac{f_0^m(E, T_e)}{f_0^{m=2}(E, T_e)}. \quad (41)$$

These functions are displayed in Fig. (5) for various m 's: $2 \leq m \leq 5$.

Alaterre, et. al. were able to fit their Fokker-Planck solutions using the above functions by determining m from the formula,

$$m(\alpha) = 2 + \frac{3}{1 + 1.66/\alpha^{0.724}}, \quad (42)$$

where

$$\alpha \equiv 2Z \frac{v_0^2}{v_{th}^2} = 4 \times 10^{-16} \frac{ZI[W/cm^2]\lambda[\mu m]^2}{T_e[keV]} (1 + \beta). \quad (43)$$

The factor $1 + \beta$ does not appear in their work. It is added here and represents the natural extension of their calculations to a microturbulent plasma. The transition of m between 2 and 5 as a function of laser intensity, when $\beta = 10$, is shown in Fig. (6).

In the discussion that follows, the selenium atomic model described in Ref. (17) is used. The model consists of hydrogenic structure in each ionization stage of selenium except the neon-like stage, which contains a complete set of the 26 $n=3$ multiplet states as shown in Fig. (7). The rate coefficients for the L-shell of this model are calculated by averaging atomic cross-sections over any specified electron distribution function. For the calculations in Ref. (17), Maxwellian distributions were used. In the gain and ionization abundance calculations that are presented in this section, we used rates that were calculated by integrating over $m = 5$ distributions. Fig. (8) illustrates the relative sensitivity of 3 pairs of rate coefficients to the underlying distribution functions, f_0^m , that are used to obtain them. Using Fig. (6), we have plotted the deviations from detailed balance of these rates as a function of $I \equiv I_{\text{laser}}$ rather than m . As the curves in Fig. (5) indicate, the depletion of the tail of the f_0^m distributions reduces the ionization rate between the neon- to fluorine-like ground states. Under these same plasma conditions, however, the increases in the bulk of the distributions act to enhance the collisional excitation rates to the $J = 0$ 3p excited state (denoted CE($J = 0$)). The $J = 0$ state whose rates are being compared in this figure is the uppermost of the $2p^5 3p$ multiplet states that are drawn to scale together with the $2p^5 3s$ states in Fig. (9). This figure also displays the four $J=0-1$ and $J=2-1$ x-ray laser transitions that have been the focus of research on neon-like lasers.

Figs. (10)-(12) show, respectively, the effects that the $m = 5$ non-Maxwellian distribution have on the gain coefficients of the $J=0-1$ and $J=2-1$ transitions (C and D respectively in Fig. (9)) and on the ionization abundances of the neon- and fluorine-like ground states. The calculations were carried out for purposes of illustration using CRE solutions to the atomic rate equations. Note that at $T_e = 1$ keV, the gains of the C and D transitions peak at $N_i \sim 2 \times 10^{20}$ ions/cm³. Both gains are enhanced significantly by the non-Maxwellian distribution; however, the enhancement is larger for the $J=0-1$ transition at 168.7 Å than it is for the $J=2-1$ transition at 206.4 Å. The reason is found in Fig. (12). The reduction in the ground-to-ground ionization rate, suggested by Fig. (8), leads to a significant increase in the population of the neon-like ground state. The excitation of this state is the dominant mechanism for pumping the $J=0$, 3p state and for creating the 3s-3p, $J=0-1$ population inversion. The $J=2$, 3p state, on the other hand, is pumped predominantly from the 3d states and is not so strongly affected by the shift in the ionization abundances. Fig. (8) shows that the excitation rate to the $J=0$ state has also been increased. Thus, there are more states to pump and

the pumping rate has been increased when the electrons are distributed in an $m = 5$ distribution rather than an $m = 2$ distribution. The net effect is to preferentially populate the $J=0$ state more than the $J=2$ state. Note, however, that since the measured gain coefficients of these lines in x-ray laser experiments is only of the order of 5, one can conclude from Figs. (10) and (11) that there is significant room for improvement in the design and performance of laboratory neon-like x-ray lasers.

IV Summary and Conclusions

The two major problems in plasma microturbulence theory are (1) to determine the dynamics of the electromagnetic energy fluctuations, inclusive of their initial growth rates, their saturation mechanisms, their propagation properties, and the dependence of these properties on inhomogeneous plasma conditions, and (2) to determine the effects of microturbulence on the electron kinetics and on the fluid dynamics of the plasma. While both of these problems are important, only the latter one was analyzed in this paper under the assumption that the microturbulence had been triggered and had grown to a saturated level that was some (small) fraction of the electron thermal energy. Under this assumption, we showed how microturbulence couples to the different terms in the spherical harmonic expansion of the electron kinetic equation for the case of ion-acoustic turbulence. We then found, in agreement with Ref. (3), that the essential effect of electron/ion-acoustic coupling is to increase the electron-ion collision frequency. In so doing, it alters three basic properties of the plasma (by essentially the same correction factor): electrical resistivity is increased, heat flow is reduced, and the critical laser intensities needed to generate non-Maxwellian distributions are reduced. The latter reduction occurs as a result of the increase in the laser absorption coefficient. This absorption change could lead to the use of probe laser beams to determine the fluctuation levels of microturbulent plasmas experimentally.

Since microturbulence reduces the threshold for generating non-Maxwellian electron distributions, its presence would also manifest itself indirectly through this distribution's influence on the x-ray emissions generated in the plasma.¹⁶ These emissions could, therefore, provide diagnostics of the microturbulence. Because the laser intensity threshold needed to produce non-Maxwellian distributions is significantly reduced by (ion-acoustic) microturbulence, our calculations suggest that these emission effects might be seen in laser-produced plasma, x-ray

laser experiments. More importantly, if non-Maxwellian distributions are generated in x-ray laser experiments conducted with high atomic number plasmas, then they could produce shifts in the ionization balance and increases in pumping rates for generating population inversions. These increases could, in turn, significantly affect the design of these experiments and significantly improve the performance of laboratory neon-like lasers.

Acknowledgement

This work was sponsored by the Strategic Defense Initiative Office of Innovative Science and Technology. The authors would like to thank J. P. Apruzese for his valuable assistance in the making of the contour plots.

References

1. W. L. Kruer, *The Physics of Laser Plasma Interactions*, Addison-Wesley Publishing Co., Redwood City, Calif. (1988).
2. C. T. Dum, *Phys. Fluids* **21**, 945 (1978).
3. C. T. Dum, *Phys. Fluids* **21**, 956 (1978).
4. J. R. Albritton, E. A. Williams, and I. B. Bernstein, *Phys. Rev. Lett.* **57**, 1887 (1986); E. M. Epperlein and R. W. Short, *Phys. Fluids B* **3**, 3092 (1991).
5. J. Delettrez, *Can. J. Phys.* **64**, 932 (1986); P. A. Holstein, J. Delettrez, S. Skupsky, and J. P. Matte, *J. Appl. Phys.* **60**, 2296 (1986).
6. K. G. Whitney and M. C. Coulter, *IEEE Trans. Plasma Sci.* **16**, 552 (1988).
7. A.B. Langdon, *Phys. Rev. Lett.* **44**, 575 (1980).
8. C. J. Keane, N. M. Ceglio, B. J. MacGowan, D. L. Matthews, D. G. Nilson, J. E. Trebes, and D. A. Whelan, *J. Phys. B* **22**, 3343 (1989); R. A. London, M. D. Rosen, M. S. Maxon, D. C. Eder, and P. L. Hagelstein, *J. Phys. B* **22**, 3363 (1989).
9. M. Rosen, S. Maxon, B. LaFontaine, H. Baldis, J. Dunn, D. Villeneuve, G. Enright, and H. Pepin, *Bull. Amer. Phys. Soc.* **36**, 2431 (1991).
10. S. Ichimaru, *Basic Principles of Plasma Physics*, W. A. Benjamin, Inc., Reading, Mass. (1973), sections 7.3, 11.3, and 11.4.
11. R. C. Davidson and N. A. Krall, *Nucl. Fusion* **17**, 1313 (1977).
12. W. M. Manheimer, *J. de Physique* **40**, C7-269 (1979).
13. V. Yu. Bychenkov, V. P. Silin, and S. A. Uryupin, *Phys. Reports* **164**, 119 (1988).
14. T. W. Johnston, *Phys. Rev.* **120**, 1103 (1960).
15. I.P. Shkarofsky, T.W. Johnston and M.P. Bachynski *The Particle Kinetics of Plasmas*, Addison-Wesley, Reading, Mass. (1966).
16. P. Alaterre, J. P. Matte, and M. Lamoureux, *Phys. Rev. A* **34**, 1578 (1986).

17. A. Dasgupta, K. G. Whitney, M. Blaha, and M. Buie, Phys. Rev. A, 46, 5973, Nov. (1992).
18. R. Bartiromo, F. Bombarda, and R. Giannella, Phys. Rev. A **32**, 531 (1985).

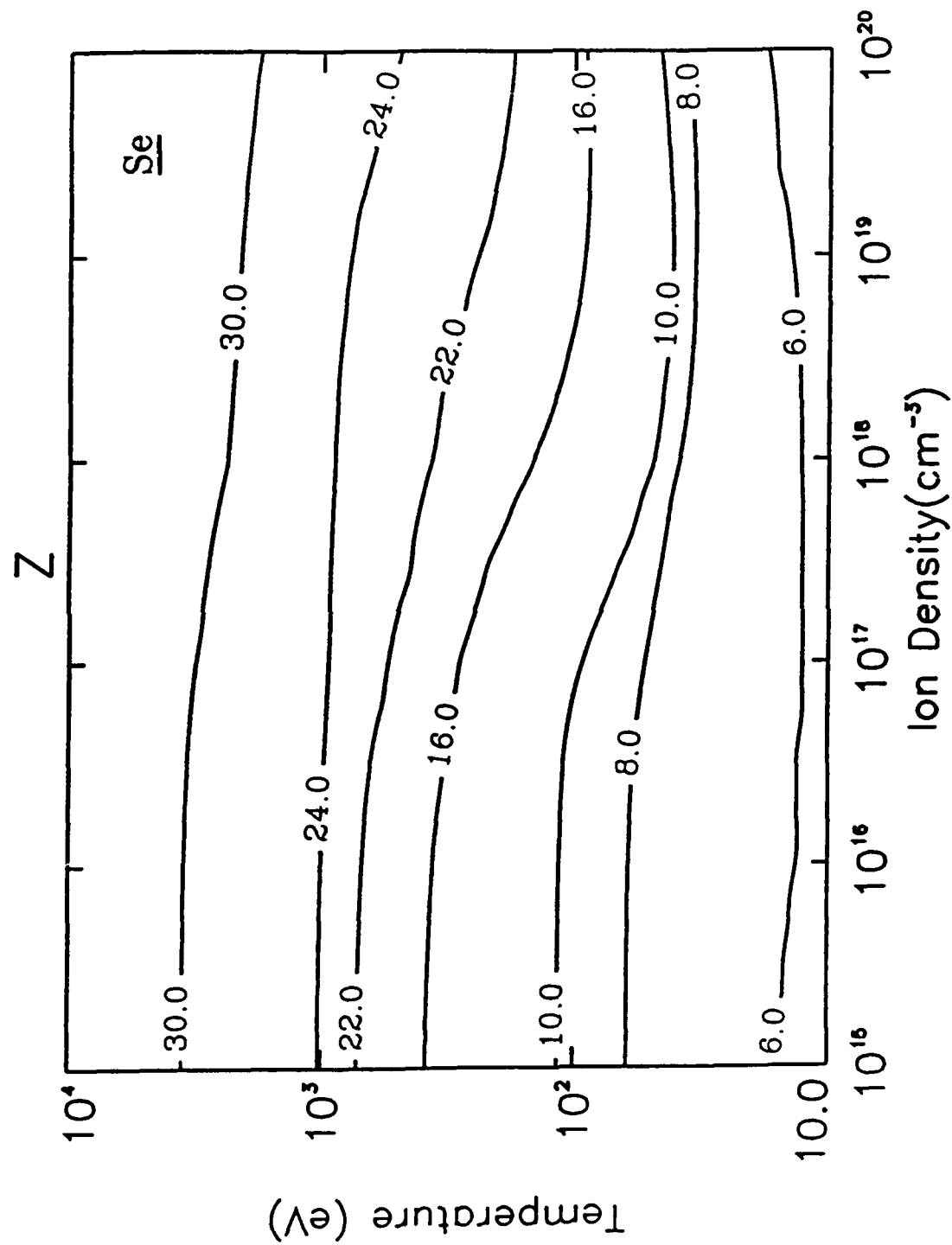


Figure 1. Contours of the average charge state, Z , of selenium in CRE are given as a function of electron temperature and ion density.

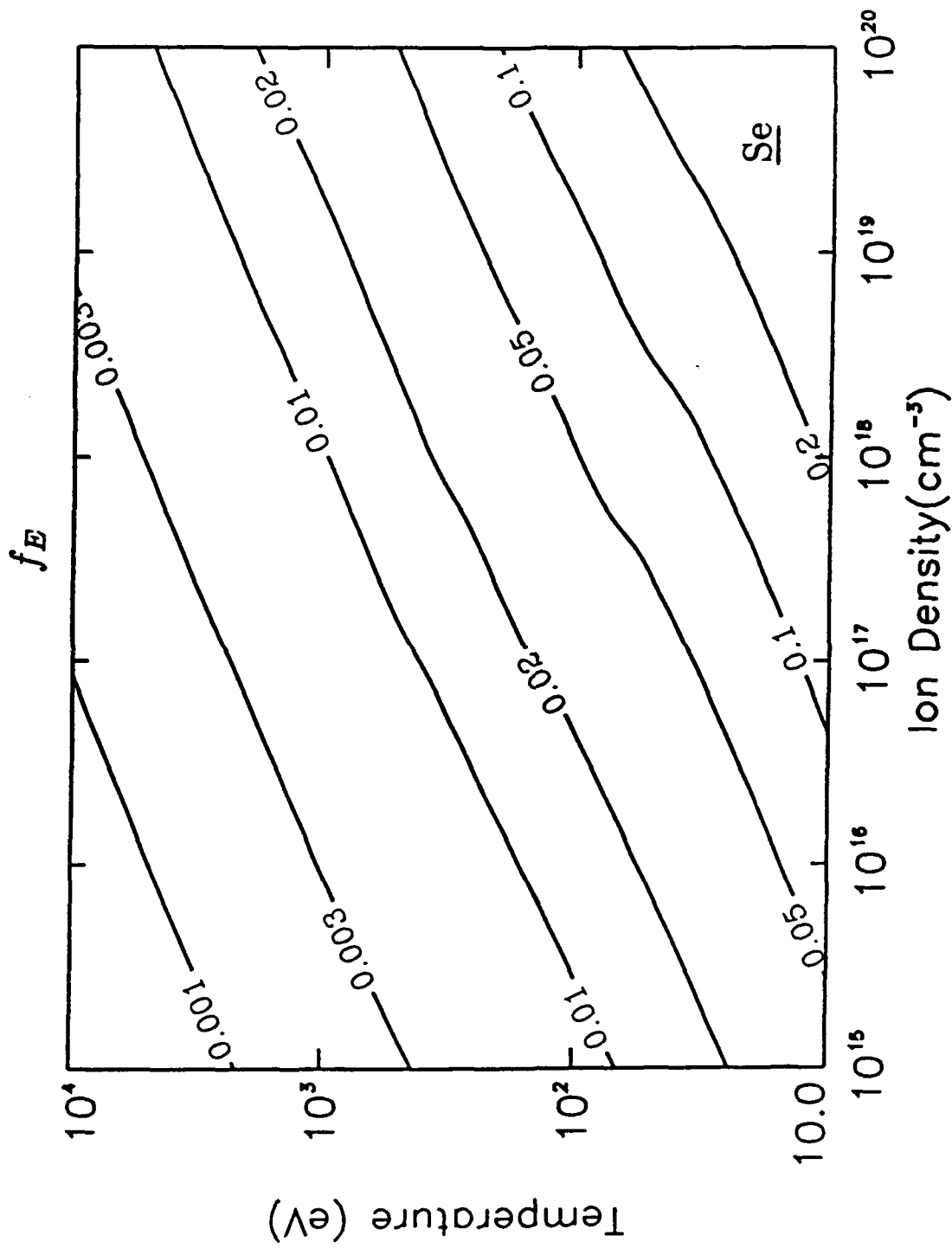


Figure 2. Contours of $f_E = 0.5g^{1/2}$, where g is the electron plasma parameter, are shown as a function of electron temperature and ion density

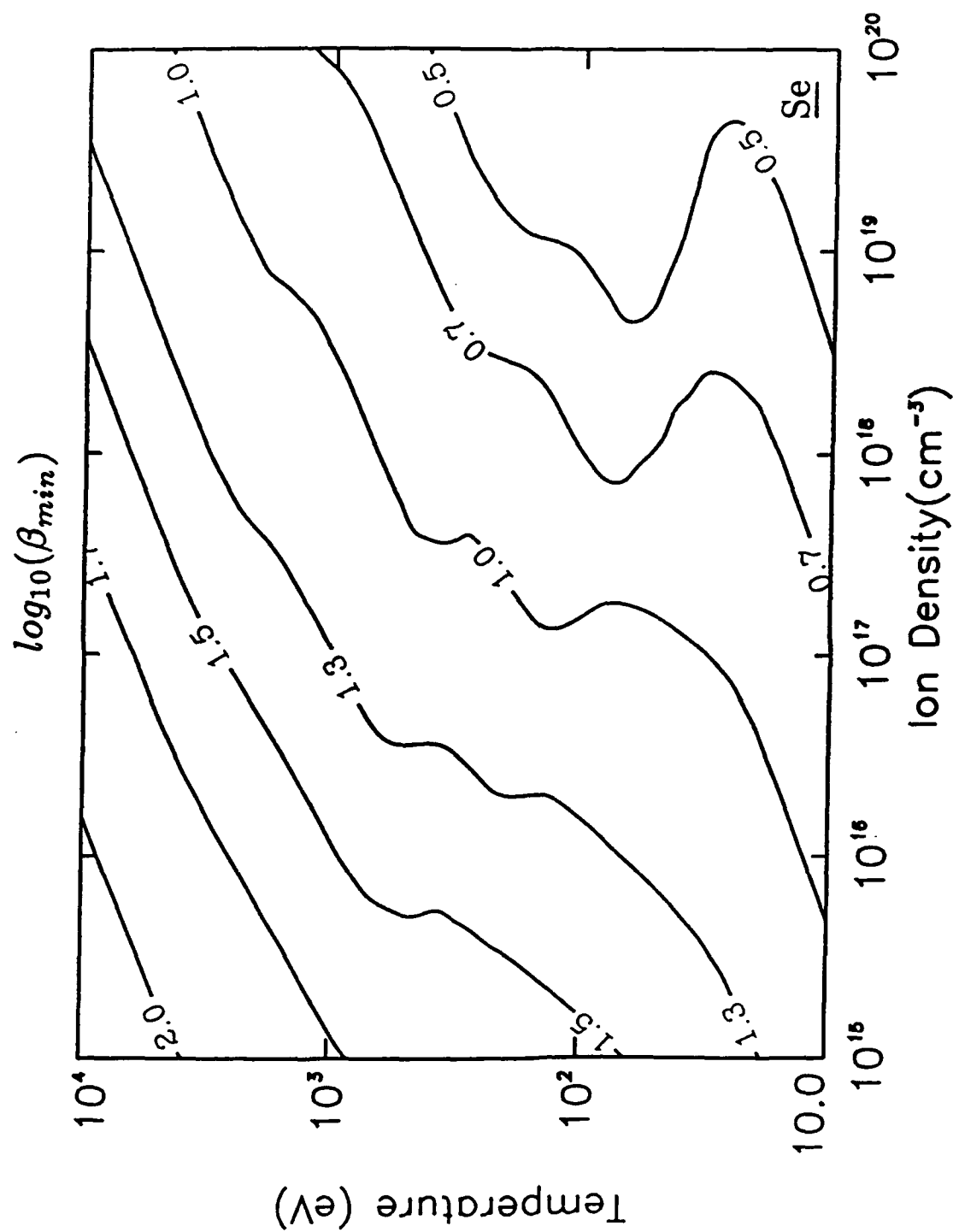


Figure 3. Contours of $\log_{10}(\beta_{min})$ are shown as a function of electron temperature and ion density. They were calculated using the values for Z and f_E shown in Figs. (1) and (2).

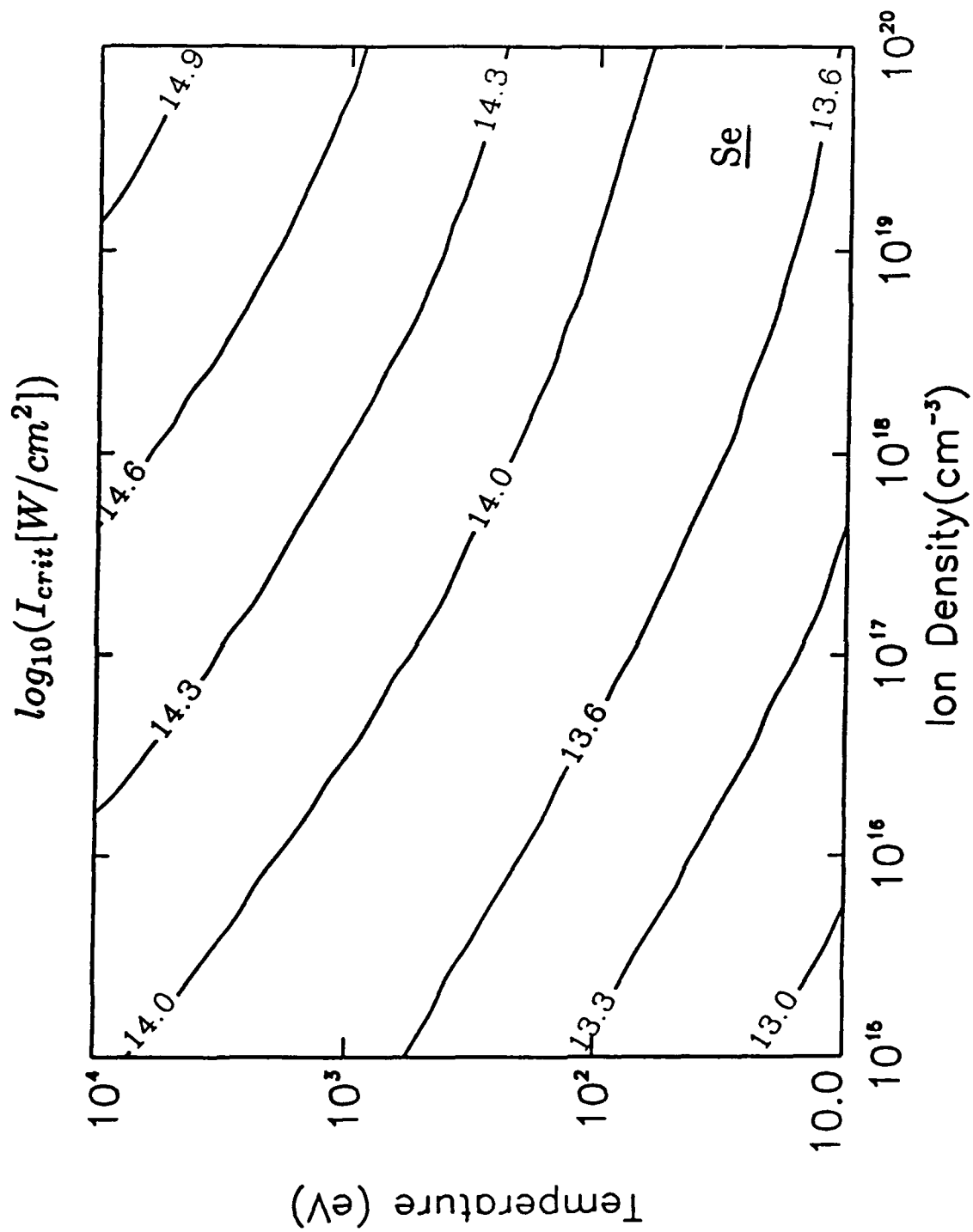


Figure 4. Contours of $\log_{10}(I_{\text{crit}})$ are shown as a function of electron temperature and ion density using the \bar{Z} and β values in Figs. (1) and (3) and a laser wavelength of $0.35\mu\text{m}$.

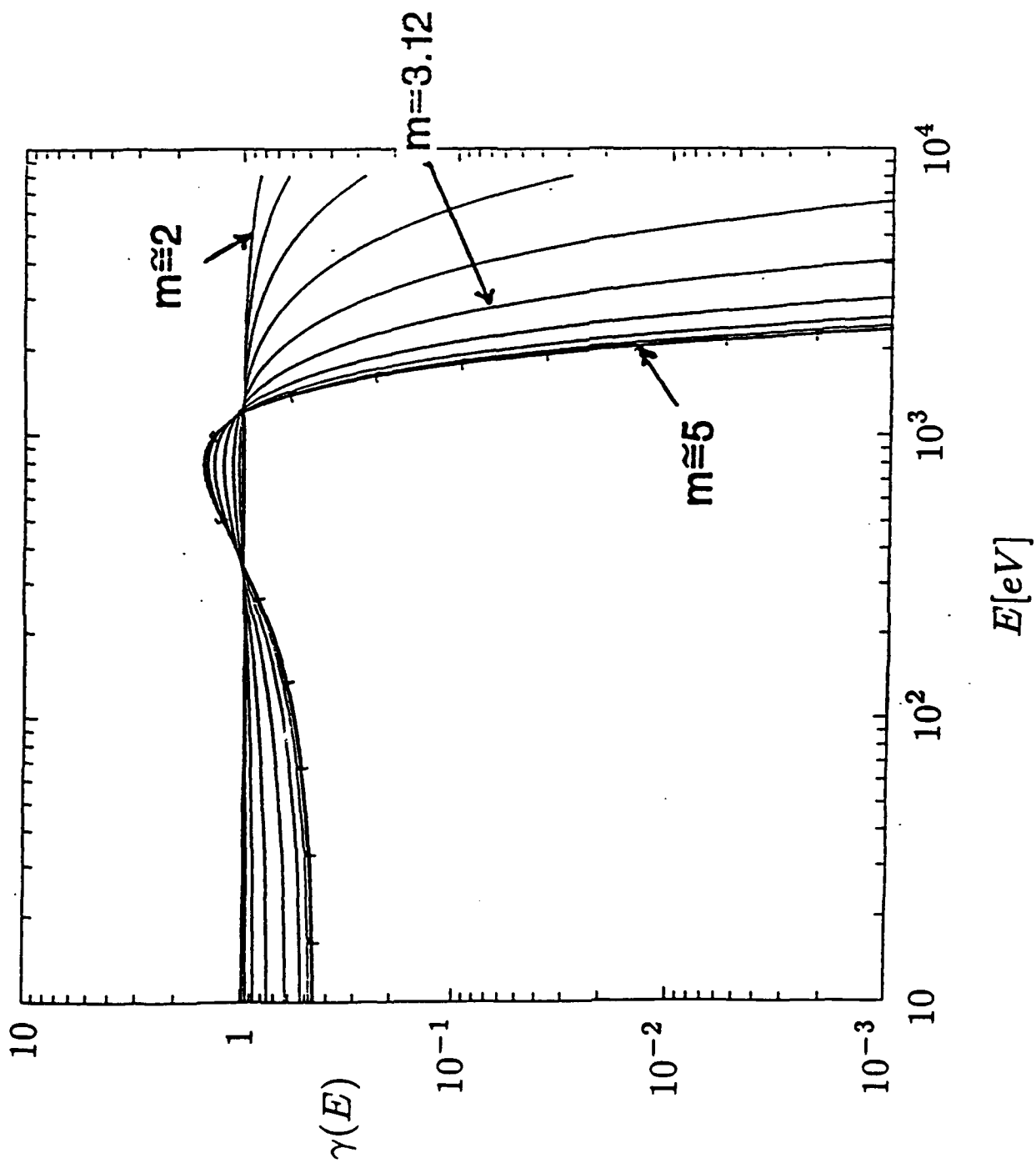


Figure 5. Deviations relative to the Maxwellian distribution, $f_0^{m=2}$, of a progression of f_0^m distributions are shown as a function of electron energy.

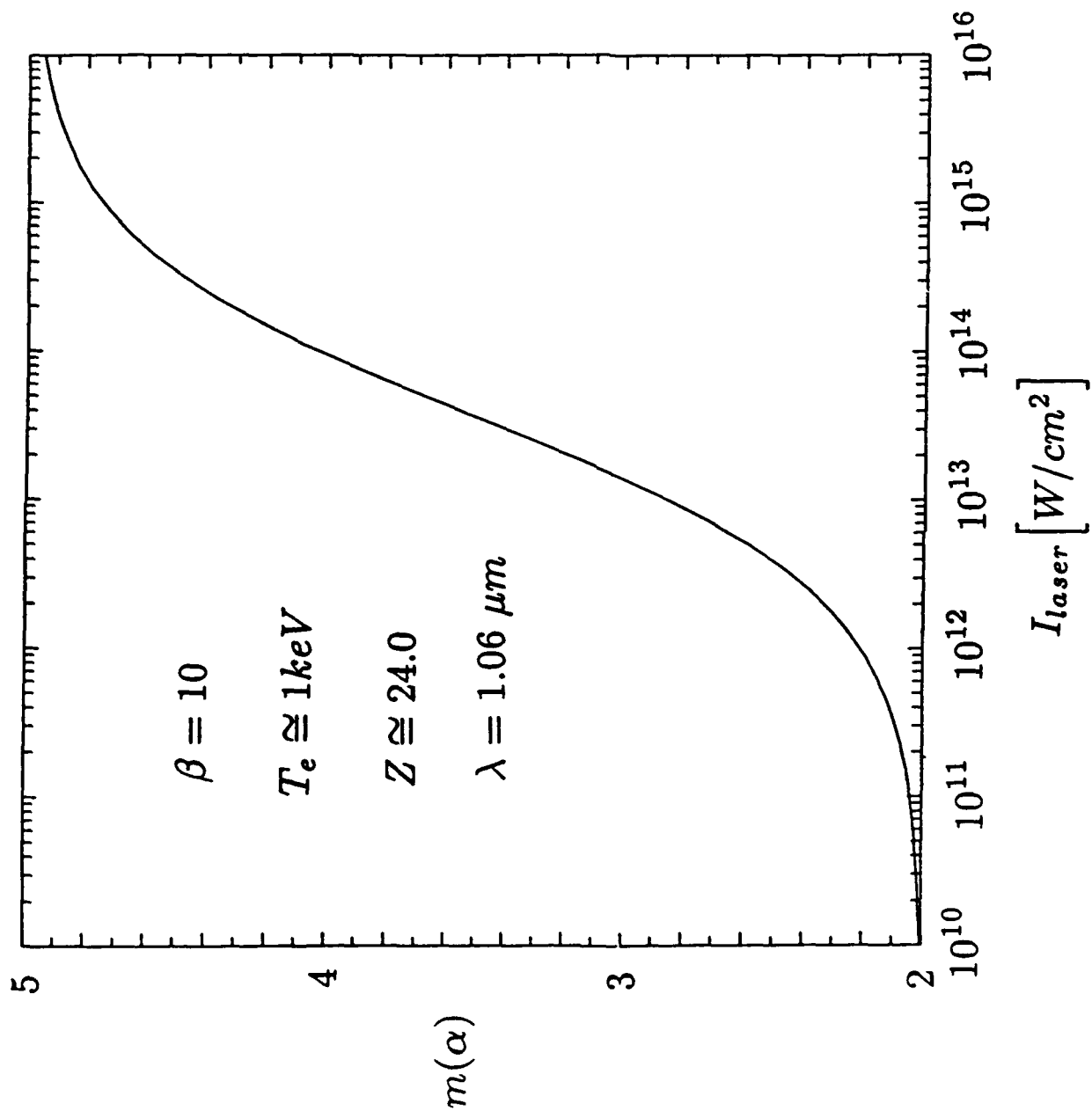


Figure 6. The progression of the electron distribution function in a microturbulent plasma from a Maxwellian to the self-similar $m = 5$ distribution is given as a function of laser intensity.

Neon-like Selenium Model (same lumped state structure throughout the L-shell)

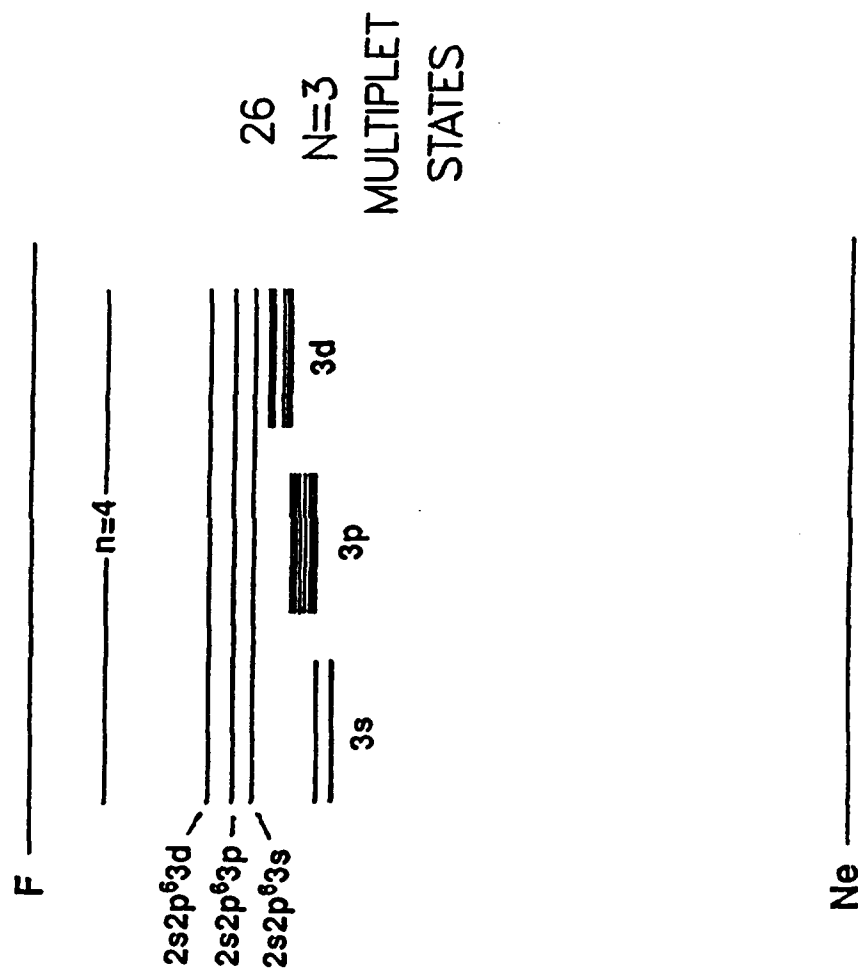


Figure 7. Atomic structure of the neon-like ionization stage. All of the $n = 3$ multiplet states are described in full detail within this atomic model.

DETAILED BALANCE OF RATES

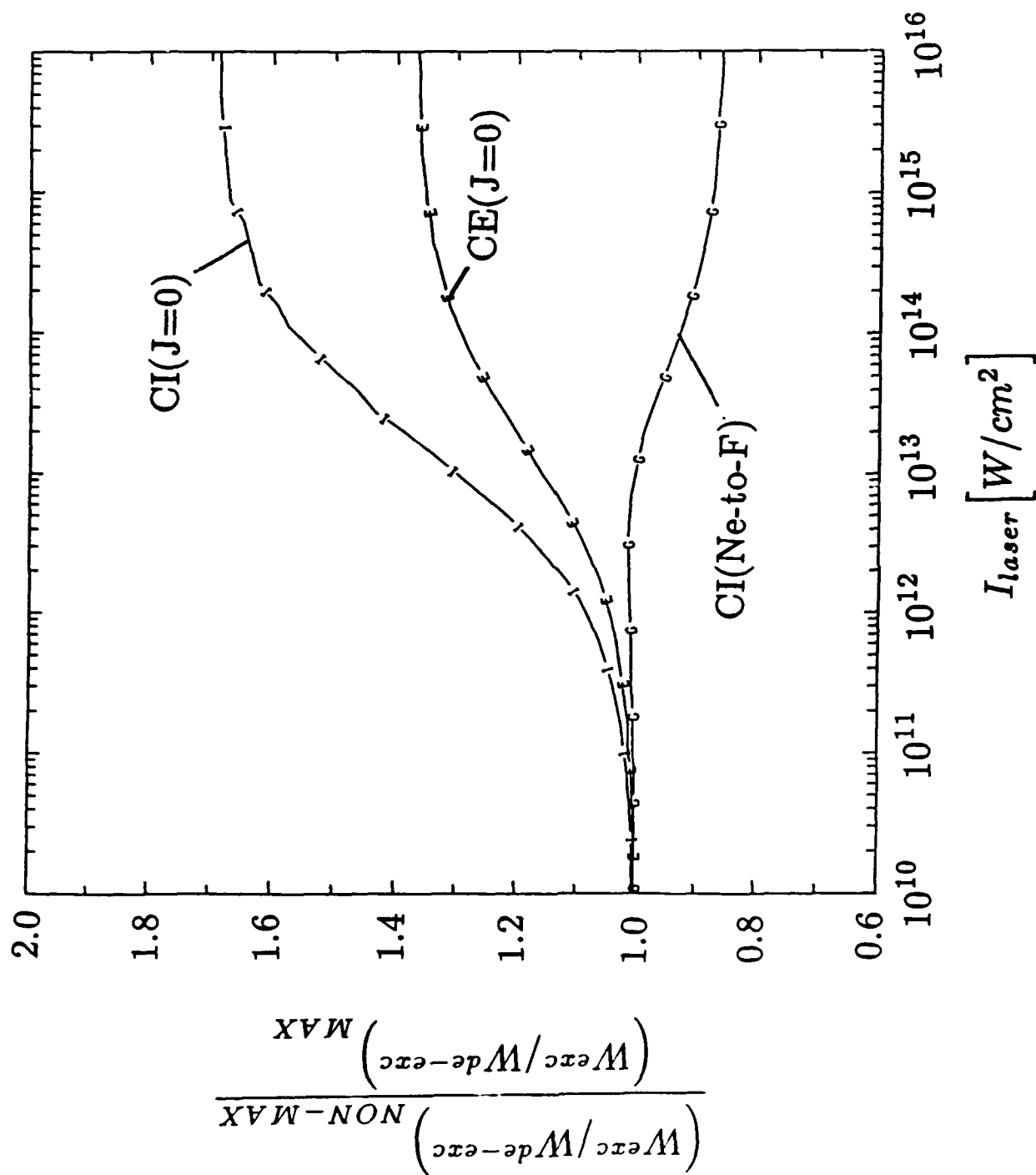


Figure 8. The degree to which rate coefficients fall out of detailed balance as a function of laser intensity (or m , see Fig. (6)) is shown. CI denotes collisional ionization and recombination processes, while CE denotes collisional excitation and deexcitation processes.

$J = 0-1$ AND $J = 2-1$
X-RAY LASER TRANSITIONS IN NE-LIKE SELENIUM

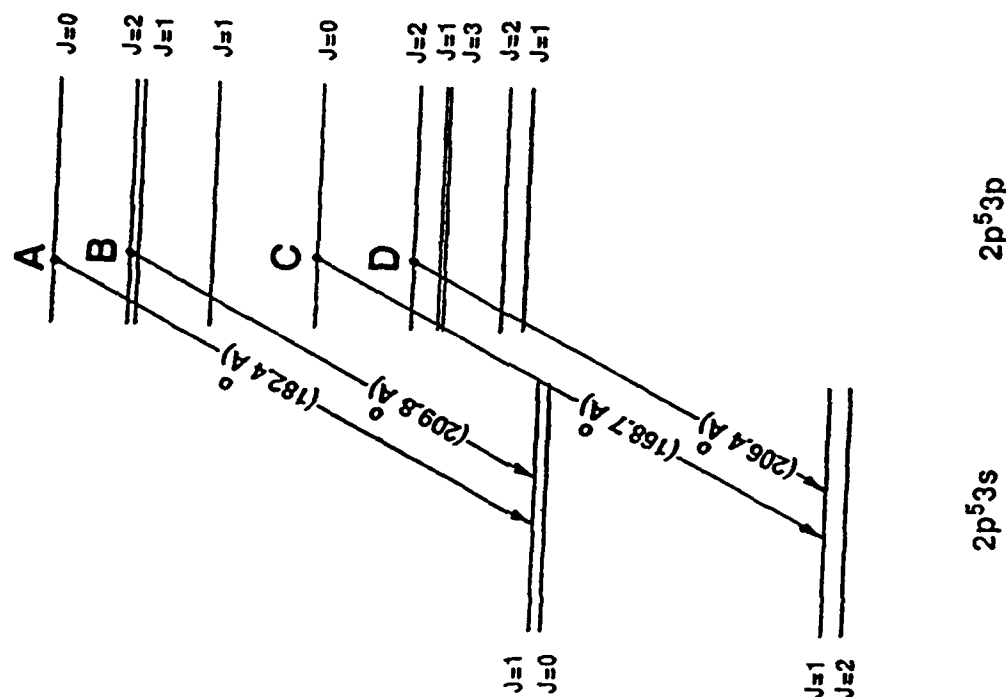


Figure 9. The $4 \ 2p^5 3s$ and $10 \ 2p^5 3p$ multiplet states of the neon-like ionization stage are drawn to scale in an energy diagram. The two $J=0-1$ (denoted A and C) and the two $J=2-1$ (denoted B and D) transitions of importance in neon-like x-ray lasers are identified along with their wavelengths.

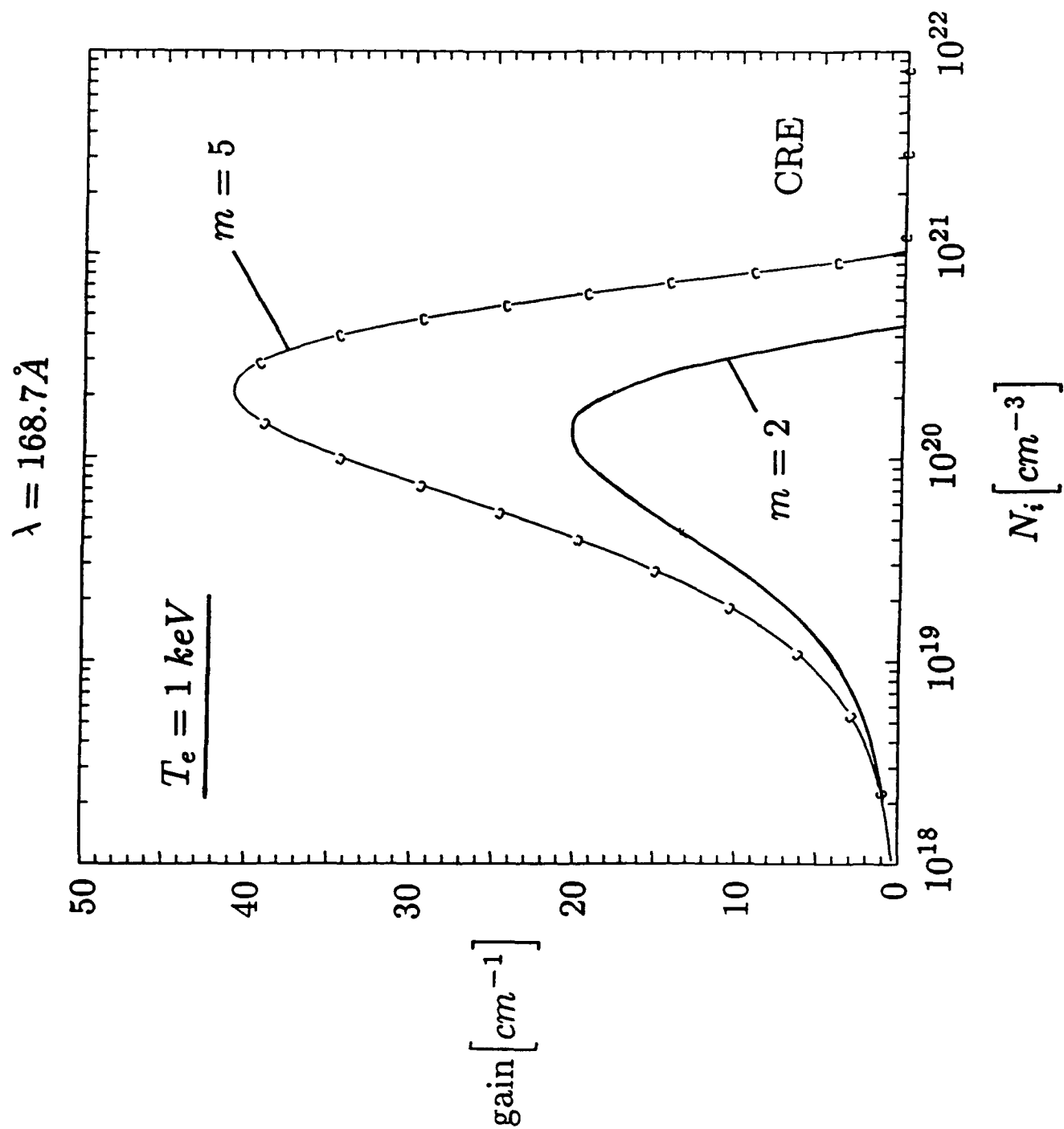


Figure 10. The gain coefficients in CRE that were calculated using f_0^2 and f_0^5 electron distributions are shown as a function of ion density for the $J=0-1$ transition denoted C in Fig. (9).

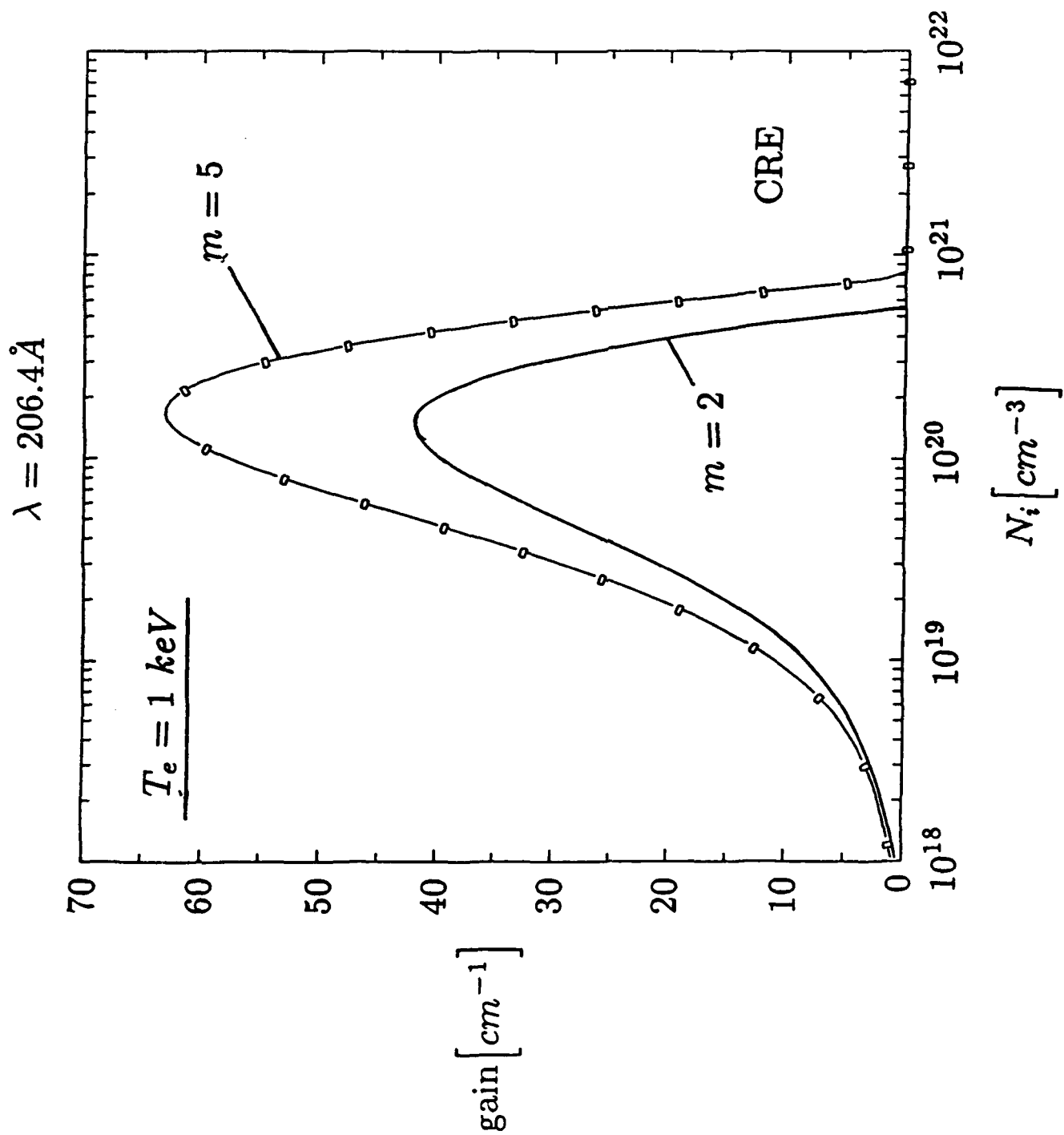


Figure 11. The gain coefficients in CRE that were calculated using f_0^2 and f_0^5 electron distributions are shown as a function of ion density for the J=2-1 transition denoted D in Fig. (9).

FRACTIONAL GROUND STATE POPULATIONS

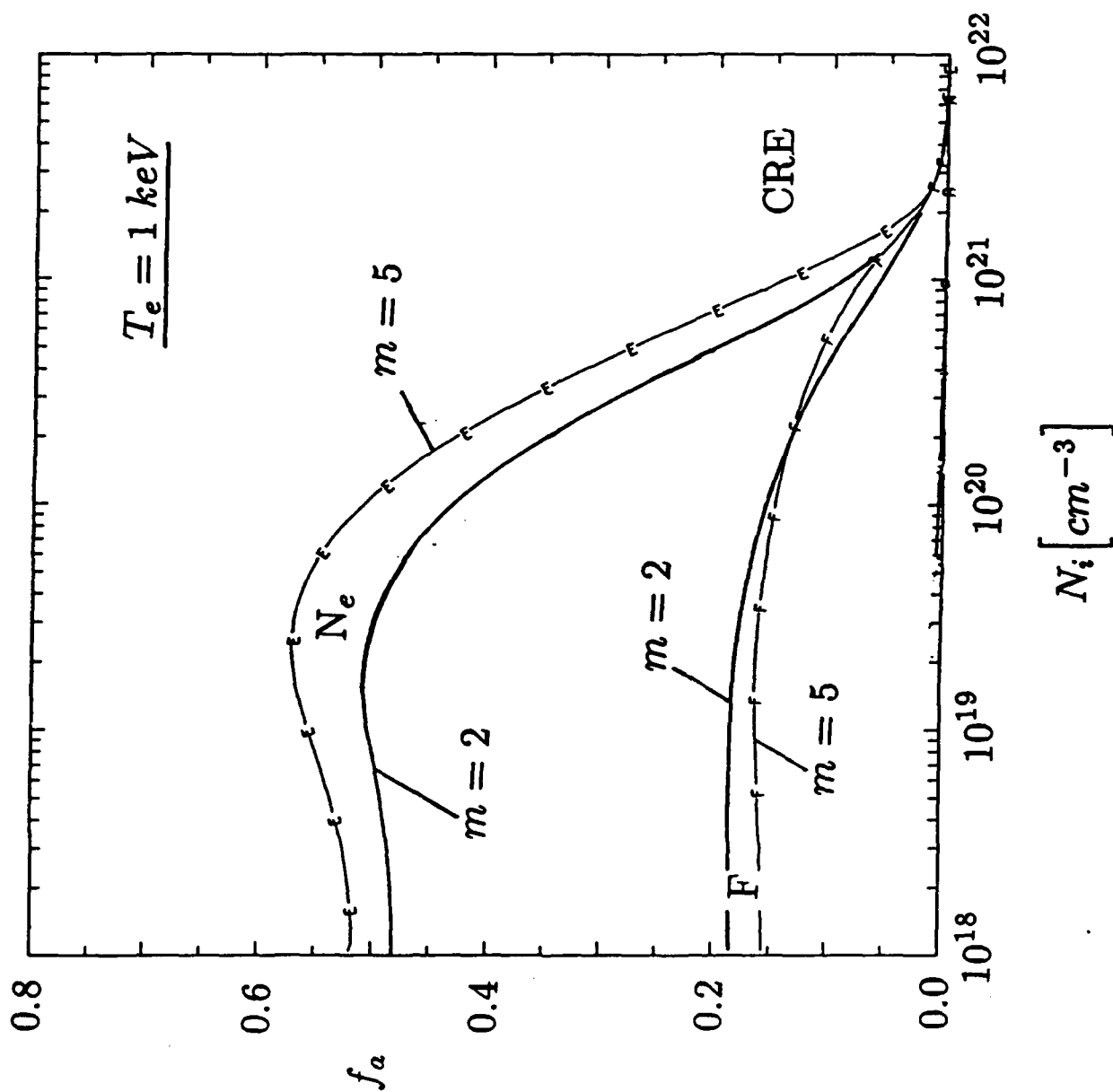


Figure 12. The fractional neon-like and fluorine-like ground state populations (N_{gd}/N_i) in CRE that were calculated using f_0^2 and f_0^5 electron distributions are shown as a function of ion density.